

**THE MAGNETIC CONFINEMENT OF ELECTRON AND PHOTON DOSE
PROFILES AND THE POSSIBLE EFFECT OF THE MAGNETIC FIELD ON
RELATIVE BIOLOGICAL EFFECTIVENESS**

by

Yu Chen

A dissertation submitted in partial fulfillment
of the requirements for the degree of
Doctor of Philosophy
(Physics)
in The University of Michigan
2005

Doctoral Committee:

Professor Frederick D. Becchetti Jr., Chair
Professor Alex F. Bielajew
Professor Leonard M. Sander
Professor Rudolf P. Thun
Research Investigator Dale W. Litzenberg

Abstract

It has been shown experimentally that the focusing provided by a longitudinal non-uniform high magnetic field can significantly improve electron beam dose profiles. This could permit improved targeting of tumors near critical areas and minimize the radiation dose to surrounding healthy tissue. The experimental results together with Monte Carlo simulations suggest that the magnetic confinement of electron radiotherapy beams may provide an alternative to proton or heavy ion radiation therapy in some cases.

In the present work, the external magnetic field capability of the Monte Carlo code PENELOPE was utilized by providing a subroutine that modeled the actual field produced by the solenoid magnet used in the experimental studies. The magnetic field in our simulation covered the region from the vacuum exit window to the phantom including surrounding air. In a longitudinal non-uniform magnetic field, it is observed that the electron dose can be focused in both the transverse and longitudinal directions. The measured dose profiles of the electron beam are generally reproduced in the Monte Carlo simulations to within a few percent in the region of interest provided that the geometry and the energy of the incident electron beam are accurately known. Comparisons for the photon beam dose profiles with and without the magnetic field are also made. The simulations also show that the electron dose profile can be manipulated

by the appropriate control of the beam energy together with the strength and displacement of the longitudinal magnetic field.

The potential application of high magnetic fields in radiation therapy requires investigation of the possible effect of the magnetic field on the relative biological effectiveness (RBE) of the radiation. An experimental study was done in this thesis to investigate the survival rate of a yeast cell line. The magnetic field was produced by NdFeB permanent magnets. *Saccharomyces cerevisiae* cells were irradiated with ^{60}Co source with and without a transverse magnetic field. Our experiments show an indication that the survival rate decreases by a few percent and hence the RBE may be increased slightly in the presence of a 0.78 T magnetic field.

Table of Contents

Acknowledgements.....	ii
List of Figures.....	vii
List of Tables.....	xii
List of Appendices.....	xiii
Abstract.....	xiv
Chapter	
1. Introduction.....	1
1.1 An overview of radiation therapy.....	1
1.2 Magnetically confined radiation therapy.....	2
1.3 Biological effect of the magnetic field.....	3
1.4 Track structure.....	4
1.5 The main goals of this work.....	5
2. Magnetic confinement of electron and photon dose profiles—a Monte Carlo simulation with a non-uniform longitudinal magnetic field.....	8
2.1 Introduction.....	8
2.2 Methods.....	10
2.2.1 Simulated setup.....	10
2.2.2 Magnetic field.....	14

2.2.3 Normalization of the simulations to the measurements.....	17
2.3 Results.....	18
2.3.1 Electron beams.....	18
2.3.2 Photon beams.....	32
2.4 Discussion.....	35
2.4.1 Simulation of multi-beam electron dose profiles.....	35
2.4.2 Possible dependence of relative biological effectiveness (RBE) on magnetic fields.....	40
2.5 Conclusion.....	40
3. The effect of the magnetic field on the relative biological effectiveness (RBE).....	45
3.1 Theory of RBE.....	45
3.1.1 DNA damage and repair.....	45
3.1.2 Models of radiation cell killing.....	48
3.1.3 Relative biological effectiveness(RBE).....	54
3.1.4 Microdosimetric model of RBE.....	59
3.1.5 Calculation of proximity function of energy deposition from simulated tracks.....	61
3.2 The experiment.....	68
3.2.1 Purpose of the experiment.....	68
3.2.2 Considerations about cells, radiation sources and magnetic fields	70
3.2.3 Experimental setup.....	76

3.2.4 Dose calculation.....	79
3.2.5 Preparation, irradiation and growth of the cells.....	93
3.2.6 Statistical properties of the cultured colonies.....	101
3.2.7 Results and test of hypotheses.....	109
3.3 Future work.....	118
4. Conclusion.....	121
Appendices.....	124

List of Tables

Table

3.1 Experiments 1-7 were done in a uniform 2.05 T field for aerated cells.....	69
3.2 Irradiation parameters.....	109
3.3 Results of the experiments.....	116

List of Figures

Figure

- 2.1 Detailed setup used in the simulation. A pencil electron beam starts from the left vacuum exit window..... 13
- 2.2 The film is sandwiched horizontally between the two halves of the phantom (dimensions in cm)..... 13
- 2.3 The solenoid magnetic field along the central axis..... 16
- 2.4 The magnetic field strength distribution (left) and field lines (right)..... 16
- 2.5 Two-dimensional plot of 21.6 MeV electron dose profiles for $B=0$ T..... 20
- 2.6 The difference between the simulation and the measurement (left) together with the statistical uncertainty of the simulation for $E=21.6$ MeV and $B=0$ T (right)..... 20
- 2.7 The relative error (i.e. difference between MC simulation and experiment relative to the maximum dose) is tallied in the region where the dose lies in between the lower threshold 10% and the upper threshold 100% of the maximum dose..... 21
- 2.8 The measured and simulated electron beam depth dose curves at central axis, 0.5 cm, 1.0 cm and 1.5 cm away from the central axis for $E=21.6$ MeV and $B=0$ T..... 22
- 2.9 The measured and simulated electron radial dose profiles at depth 2 cm, 4 cm, 5 cm and 6 cm for $E=21.6$ MeV and $B=0$ T..... 23
- 2.10 Two-dimensional plot of 21.6 MeV electron dose profiles for $B=3.03$ T..... 26

2.11 The difference between the simulation and the measurement (left) and the statistical uncertainty of the simulation for $E=21.6$ MeV and $B=3.03$ T.....	26
2.12 The relative error (i.e. difference between MC simulation and experiment relative to the maximum dose) tallied in the region where the dose lies in between the lower threshold 10% and the upper threshold 100% of the maximum dose.....	27
2.13 The measured and simulated electron depth dose curves along the central axis, 0.5 cm, 1.0 cm, and 1.5 cm away from the central axis for $E=21.6$ MeV and $B=3.03$ T.....	28
2.14 The measured and simulated electron radial dose profiles at depth 2 cm, 4 cm, 5 cm and 6 cm for $E=21.6$ MeV and $B=3.03$ T.....	29
2.15 Three-dimensional plot of the electron tracks near and inside the phantom without the aluminum collimator.....	30
2.16 This graph shows the depth dose profiles when the phantom was placed at different longitudinal positions in the magnetic field, where electron energy is 20 MeV and $B=3$ T.....	31
2.17 10 MV photon beam dose distributions.....	34
2.18 (a) upper left: dose profile for 10 MV photon beams. (b) upper right: dose profile for 35 MeV electron beam in 6 T solenoid magnetic field. (c) lower left: dose profile for 35 MeV electron beam in 9 T solenoid magnetic field. (d) lower right: dose profile for 35 MeV electron beam in 12 T solenoid magnetic field.....	37
2.19 Two-dimensional dose plot of the multi-beam 35 MeV electron dose profile with a 6 T solenoid magnet.....	38

2.20 The dose along a beam axis with electron energy of 35 MeV and peak value of the solenoid magnetic field 6 T.....	39
3.1 An idealized schematic comparing two single strand breaks (top) and one double strand break (bottom).....	47
3.2 Graph showing the LPL-calculated survival response pattern of CHO 10B2 cells irradiated ¹³⁷ Cs gamma-rays.....	53
3.3 Survival curves for various types of clonogenic mammalian cells irradiated with 300-kV x-ray or 15-MeV d ⁺ →T neutrons.....	56
3.4 Variation of RBE with LET for survival of mammalian cells of human origin..	57
3.5 Survival curves for cultured cells of human origin exposed to 250-kVp x-rays, 15-MeV neutrons, and 4-MeV α-particles.....	57
3.6 Dose-response curves for Chinese hamster cells (CHL-F line) grow <i>in vitro</i> and exposed to ⁶⁰ Co γ-ray at various dose rates.....	58
3.7 The schematic picture showing the effect of the magnetic field on α.....	60
3.8 The schematic picture showing the effect of the magnetic field on β.....	60
3.9 Energy deposition proximity function for B=0 T.....	63
3.10 Energy deposition proximity function for B=10 T.....	64
3.11 Energy deposition proximity function for B=100 T.....	65
3.12 Energy deposition proximity function for B=1000 T.....	66
3.13 Energy deposition proximity function for B=10000 T.....	67
3.14 Front view of the electromagnet.....	69
3.15 The rods of the ⁶⁰ Co gamma source.....	72
3.16 The cover and the lid on the well of the gamma source.....	73

3.17 The source at the bottom of the water pool.....	73
3.18 Schematic picture of the superconducting magnet.....	75
3.19 Picture of the permanent magnet.....	75
3.20 Experimental setup.....	77
3.21 Geometry of the membrane and a non-nutrient agar plate.....	77
3.22 Top view of the set up. The circle is the source and the blocks are the magnets.....	78
3.23 Detailed view of the magnets and the nitrocellulose membrane.....	78
3.24 The iso-fluence lines of the primary photons of the ^{60}Co source.....	80
3.25 This plot shows the uniformity of the primary photon fluence at radial position where the samples are irradiated.....	81
3.26 The primary fluence as a function of its radial position.....	81
3.27 Three-dimensional plot of the magnetic field of a pair of permanent magnets of 2 inch diameter.....	82
3.28 The magnetic field in the cross section area of the 2 inch diameter magnets.....	83
3.29 The magnetic field in the cross section area of the 7/8 inch diameter magnets.....	83
3.30 Detailed view of the magnetic field in the cross section area of the 2 inch diameter magnets.....	84
3.31 Detailed view of the magnetic field in the cross section area of the 7/8 inch diameter magnets.....	84

3.32 The magnetic field flux density plotted as a function of its radial position for the 2 inch diameter magnets.....	85
3.33 The magnetic field flux density plotted as a function of its radial position for the 7/8 inch diameter magnets.....	85
3.34 Schematic geometry of Model 1.....	89
3.35 Schematic geometry of Model 2.....	89
3.36 Comparison of the depth dose in the middle of the water phantom with and without a transverse magnetic field.....	90
3.37 Comparison of the radial dose in the middle of the water phantom with and without a transverse magnetic field.....	90
3.38 Comparison of the depth dose of a 1 cm slab of water with and without a transverse magnetic field.....	91
3.39 One layer of non-nutrient agar.....	92
3.40 The non-nutrient agar plate with the membrane removed.....	98
3.41 Cells without irradiation grew into colonies of similar size.....	99
3.42 Irradiated cells grew into colonies of different sizes.....	99
3.43 Mutants are those colonies of irregular shapes.....	100
3.44 Variation in p leads to a broadened binomial distribution.....	106
3.45 A broadened distribution for 210 cells in average.....	108
3.46 A broadened distribution for 750 cells in average.....	108
3.47 The number of survival cells and the standard deviation of the mean are plotted for the experiments where the ratio of the width of the membrane to the diameter of the magnet is 0.2.....	116

List of Appendices

Appendix

A.	The primary fluence of the ^{60}Co source.....	125
B.	Serial Binomial Process.....	127
C.	Colonies counts for all the experiments.....	129
D.	Experimental Setups.....	145
E.	Order Information.....	149
F.	Agar Recipe.....	151

Chapter 1

Introduction

1.1 An overview of radiation therapy

Radiation therapy is widely used in cancer treatment¹. About fifty percent of cancer patients are treated with radiation at some time during their disease. As an example in radiation therapy, external radiation beams are delivered to the tumors. Over time, this radiation damages the cells that are in the path of its beam—normal cells as well as cancer cells. Cancer cells are very busy growing and making new cells, hence spend more time in mitosis (M phase) of the cell cycle. In M phase, the cells are more vulnerable to radiation damage. Because cancer cells also are less well organized than healthy cells, they are less able to repair the damage and recover. Thus cancer cells are more easily destroyed by radiation, while healthy, normal cells repair themselves and survive.

Substantial numbers of patients with common cancers achieve long-term tumor control largely by the use of radiation therapy. DeVita *et al*². and Souhami and Tobias³ suggested that surgery and/or radiotherapy could be expected to be successful in approximately 40% of these cases. In about 15% of all cancers, radiotherapy would be the principal form of treatment.

Photon radiotherapy is the most widely used radiation therapy. People have developed 3-D conformal photon therapy, stereotactic radiosurgery and intensity

modulated radiation therapy (IMRT). Recently, researchers try to include tracking of motions such as breath into the optimization of IMRT.

Proton radiotherapy has a finite range and Bragg peak⁴. There is a significant difference between standard (x-ray) radiation treatment and proton therapy. If given in sufficient doses, x-ray radiation techniques will control many cancers. But, because of the physician's inability to adequately conform the irradiation pattern to the cancer, healthy tissues may receive a similar dose and can be damaged. Consequently, a less-than-desired dose is frequently used to reduce damage to healthy tissues and avoid unwanted side effects. The power of protons is that higher doses of radiation can be used to control and manage cancer while significantly reducing damage to adjacent healthy tissue and vital organs. However, proton beams are difficult to bend and higher energy is need for deep penetration, hence the proton facilities are usually very expensive.

Electron radiotherapy is usually used in treating tumor at shallow depth, especially for breast cancers. Another form of electron therapy, internal bracktherapy, is used in the treatment of prostate cancers. Electrons have a finite range but are easily scattered due to their small mass. Tumors in deeper depth are not suitable for traditional external electron therapy due to the large scattering and hence damage to surrounding healthy tissue.

1.2 Magnetically confined radiation therapy

In order to reduce scattering of the electrons, Bostick⁵ proposed the use of longitudinal magnetic field for the enhancement of electron beam dose distributions. Bielajew⁶ pointed out the erroneous Bragg peak effect for electron beams in uniform

longitudinal magnetic fields and demonstrated that a strong longitudinal magnetic field can significantly reduce the lateral spread of scattered and secondary electrons and hence the penumbra for electron and photon irradiations. The experimental study by Litzenberg⁷ *et al.* clearly demonstrated the application of a high magnetic field, a longitudinal non-uniform field in particular, can provide both transverse and longitudinal confinement of high-energy electron radiation therapy beams inside the phantom. Since the relatively low-cost linacs are readily available, magnetically-confined electron radiotherapy may be a cost-effective alternative to proton and heavy ion radiotherapy.

Monte Carlo simulations of Ramahi⁸ and Naqvi⁹ *et al.* further investigate the possibility and effectiveness of a longitudinal magnetic field to improve the photon dose profiles in regions around tissue-air interface such as upper respiratory cavities. Monte Carlo simulations for the application of a transverse magnetic field to control photon dose profiles also have been studied by Reiffel¹⁰, Li¹¹, and David¹² *et al.*

1.3 Biological effect of the magnetic field

Along the advance of proposed application of magnetic field in radiation therapy, people would like to investigate the biological effect of magnetic fields. Rockwell investigated the influence of a 0.14 T magnetic field on the radiosensitivity and recovery of EMT6 cells irradiated with 120 kV x-rays and reported minimal effect¹³. Later on, Nath *et al.* used a 2 T magnetic field to study the response of mammalian cells irradiated with 30 MeV x-rays¹⁴. They could not detect significant effect due to the statistical uncertainties of their experiment.

Some researchers investigated the biological effects of the magnetic field alone. Raylman *et al.* reported that the prolonged exposure to a 7 T magnetic field appeared to inhibit the growth of three human tumor cell lines *in vitro*¹⁵. Onodera *et al.* studied the effect of a 10 T static magnetic field on human peripheral blood immune cells¹⁶. Their results suggested that the magnetic field had acute effects on immune cells during cell division while the field exposure had minimal effect on immune cells in a non-dividing phase. Nakahara *et al.* concluded no effect on cell growth, cell cycle distribution or micronucleus frequency for the exposure of CHO-K1 cells to a 10 T static magnetic field, but the exposure to the magnetic field might cause an increase in the micronucleus formation induced by 4 Gy x-rays¹⁷. In their experiment, the x-ray dose was delivered before the exposure to the magnetic field. They were not performed at the same time. Nonetheless, the genotoxic potential of magnetic fields is still controversial¹⁸.

1.4 Track structure

The quality of radiation is commonly attributed to linear energy transfer (LET), which is a measure of the average energy deposited along the track of a particle per unit length and depends on the type of particle and its energy. Further more, the LET alone is not sufficient to describe the quality of radiation for biological purposes. The biological effectiveness can vary for different particles with the same LET. Physics calculations have shown that about 30-50% of the absorbed dose from common low-LET radiations such as hard x-ray or γ -rays is deposited by low-energy (0.1-5 keV) secondary electrons¹⁹. Therefore these low energy secondary electrons are a significant cause of double-strand break induction, cell inactivation and other cellular effects²⁰.

Although the LET does not change in the presence of a magnetic field of several Tesla, the trajectories of the low-energy secondary electrons can be changed by a strong magnetic field. This could possibly change the probability of DNA lesion formation and hence the RBE of the radiation. We will discuss the popular biological models in Chapter 3 and propose how the magnetic field effect can be included.

1.5 The main goals of this work

The possible application of magnetic fields in electron and photon radiation therapy requires a suitable tool to calculate the dose. The Monte Carlo (MC) transport code PENELOPE^{21,22} has the magnetic field ability included but lacks verification with real magnetic fields. In addition, RBE in the presence of magnetic fields has to be investigated before any clinical application.

Thus the first part of the dissertation is a comparison of data from the simulation to an existing experiment using the MC code PENELOPE. The second part of the dissertation describes a related experimental study of the effect of the magnetic field on RBE. Early works^{13,14} showed minimal effect of the magnetic field on RBE. However, the uncertainties in the previous work are relatively large. We tried to reduce the uncertainties and better results were obtained, showing a possible small effect.

References to Chapter 1

-
- ¹ G. G. Steel, "Basic clinical radiology", Arnold, 2002, pp 1-2
- ² V. T. DeVita, A. Goldin, V. T. Oliverio *et al.*, "The drug development and clinical trials programs of the Division of Cancer Treatment National Cancer Institute", *Cancer Clin Trials* 2: 195-216 (1979)
- ³ R. Souhami and J. Tobias, "Cancer and its Management", Blackwell, Oxford (1986)
- ⁴ S. Webb, "The physics of three-dimensional radiation therapy", IOP publishing Ltd. 1993 pp172-173
- ⁵ W. H. Bostick, "Possible techniques in direct-electron-beam tumor therapy", *Phy. Rev.* **77**, 564-565 (1950)
- ⁶ A. F. Bielajew, "The effect of Strong Longitudinal magnetic fields on dose deposition from electron and photon beams," *Med. Phys.* **20**, 1171-1179 (1993)
- ⁷ D. W. Litzenberg, B. A. Fraass, D. L. McShan, T. W. O'Donnell, D. A. Roberts, F. D. Becchetti, A. F. Bielajew, J. M. Moran, "An Apparatus for Applying Strong Longitudinal Magnetic Fields to Clinical Photon and Electron Beams", *Phys Med Bio* **V46** no. 5, pp. N105-N115, (2001)
- ⁸ S. J. Wadi-Ramahi, S. A. Naqvi, J. C. H. Chu, "Evaluating the effectiveness of a longitudinal magnetic field in reducing underdosing of the regions around upper respiratory cavities," *Med. Phys.* **28**, 1711-1717 (2001)
- ⁹ S. A. Naqvi, X. A. Li, S. W. Ramahi, J. C. Chu, and S. Ye, "Reducing loss in lateral charged-particle equilibrium due to air cavities present in x-ray irradiated media by using longitudinal magnetic fields," *Med Phys.* **28**, 603-611 (2001)
- ¹⁰ L. Reiffel, A. Li, J. Chu, R. W. Wheatley, S. Naqvi, R. Pillsbury and A. Saxena, "Control of photon beam dose profiles by localized transverse magnetic fields," *Phys. Med. Biol.* **45**, N177-N182 (2000)
- ¹¹ X. A. Li, L. Reiffel, J. Chu, and S. Naqvi, "Conformal photon-beam therapy with transverse magnetic fields: Monte Carlo study," *Med. Phys.* **27**, 1447 (2000)
- ¹² D. Jette, "Magnetic fields with photon beams: Monte Carlo calculations for a model magnetic field," *Med. Phys.* **27**, 2726-2738 (2000)
- ¹³ S. Rockwell, "Influence of a 1400-gauss magnetic field on the radiosensitivity and recovery of EMT6 cells *in vitro*", *Int. J. Radiat. Biol.* **31**, 153-160 (1977)

-
- ¹⁴ R. Nath, R. J. Schults and P. Bongiorni, "Response of mammalian cells irradiated with 30 MV X-rays in the presence of a uniform 20-kilogauss magnetic field", *Int. J. Radiat. Biol.* **38** No. 3, 285-292 (1980)
- ¹⁵ R. R. Rayman, A. C. Clavo and R. L. Wahl, "Exposure to strong static magnetic field slows the growth of human cancer cells *in vitro*", *Bioelectromagnetics* **17**(5): 358-63 (1996)
- ¹⁶ H. Onodera, Z. Jin, S. Chida, Y. Suzuki, H. Tago, Y. Itoyama, "Effect of 10-T static magnetic field on human peripheral blood immune cells", *Radiat. Res.* **159** (6): 775-9 (2003)
- ¹⁷ T. Nakahara, H. Yaguchi, M. Yoshida, J. Miyakoshi, "Effects of exposure of CHO-K1 cells to a 10 T static magnetic field", *Radiology* **224**(3): 817-22 (2002)
- ¹⁸ J. McCann, F. Dietrich, C. Rafferty, "The genotoxic potential of electric and magnetic fields: an update", *Mutat. Res.* **411**(1): 45-86 (1998)
- ¹⁹ H. Nikjoo and D. T. Goodhead, "Track structure analysis illustrating the prominent role of low-energy electrons in radiobiological effects of low-LET radiation", *Phys. Med. Biol.* **36**, 229-238, (1991)
- ²⁰ D. T. Goodhead and H. Nikjoo, "Clustered damage in DNA: Estimates from track-structure simulations", *Radiat. Res.* **148**, 485-486, (1997)
- ²¹ J. Baró, J. M. Fernández_Varea and F. Salvat, "PENELOPE: an Algorithm for Monte Carlo Simulation of the Penetration and Energy Loss of Electrons and Positrons in Matter," *Nuclear Instruments and Methods* **VB100**, 31-46 (1995)
- ²² J. Sempau, E. Acosta, J. Baró, J. M. Fernández_Varea and F. Salvat, "An Algorithm for Monte Carlo simulation of coupled electron-photon transport", *Nuclear Instruments and Methods Research B* **132** 377-390 (1997)

Chapter 2

Magnetic confinement of electron and photon dose profiles—a Monte Carlo simulation with a non-uniform longitudinal magnetic field*

2.1 Introduction

The effect of magnetic fields on dose deposition has been studied for a long time. Bostick¹ proposed the use of longitudinal magnetic field for the enhancement of electron beam dose distributions. Shih's² Monte Carlo simulation followed by different experiments of Whitmire^{3, 4}, Nath⁵, and Paliwal⁶ *et al.* reported the effect of transverse magnetic field enhancing electron-dose profiles in homogenous and inhomogeneous media. Weinhou⁷ *et al.* studied the enhancement of electron beam dose distributions by longitudinal magnetic fields of a single-coil superconducting magnet with Monte Carlo simulations. Bielajew⁸ pointed out the erroneous Bragg peak effect for electron beams in uniform longitudinal magnetic fields and proved that for broad parallel beams, owing to lateral equilibrium, the central axis depth dose curve is independent of the strength of the external uniform longitudinal magnetic field. He demonstrates that a strong longitudinal magnetic field can significantly reduce the lateral spread of scattered and secondary electrons and hence the penumbra for electron and photon irradiations. In other words, a uniform longitudinal magnetic field shows its dose-enhancement effect only in places

* Chapter 2 is the draft of a paper accepted for publication in the journal *Medical Physics*. Co-authors: Alex Bielajew, Dale Litzenberg, Jean Moran and Fred Becchetti

where the lateral charged particle equilibrium cannot be achieved originally. Monte Carlo simulations of Ramahi⁹ and Naqvi¹⁰ *et al.* further investigate the possibility and effectiveness of a longitudinal magnetic field to improve the photon dose profiles in regions around tissue-air interface such as upper respiratory cavities. Monte Carlo simulations for the application of a transverse magnetic field to control photon dose profiles also have been studied by Reiffel¹¹, Li¹², and David¹³ *et al.* The experimental work by Litzenberg¹⁴ *et al.* clearly demonstrated the application of a high magnetic field, a longitudinal non-uniform field in particular, can provide both transverse and longitudinal confinement of high-energy electron radiation therapy beams inside the phantom. This can then permit precise targeting of tumors near critical areas, enhance the dose in the tumor region at greater depths and the dose to surrounding healthy tissue can be suppressed. Relative to the enhanced dose at depths, the dose at the beam entrance region also can be reduced. This results in an internally focused, confined beam leading to a more localized, enhanced dose profile. Although electron linacs are the primary accelerator used to produce most clinical photon radiation therapy beams, the primary electron beam is seldom used for treating internal tumors. However, high-energy electron beams with a suitably focused and confined dose profile could prove useful as a cost-effective alternative to proton- and other ion-therapy beams, or as an additional modality in electron and photon radiation therapy^{15,16}.

The main purpose of the present work was to accurately simulate the results of the existing experiment¹⁴ and to understand the origin of a number of “anomalies” seen in the dose profiles obtained in the experiment. In this study the Monte Carlo code PENELOPE^{17,18} was utilized to realistically simulate the experiment. The realistic

magnetic field produced by the superconducting magnet was modeled in our simulations. It covered the whole region along the beam line from the vacuum exit window to the phantom including the surrounding air.

2.2 Methods

The simulation algorithm of PENELOPE^{17,18} is based on a scattering model that combines numerical databases with analytical cross section models for the different interaction mechanisms and it is applicable to energies (kinetic energies in the case of electrons and positrons) from a few hundred eV to ~ 1 GeV. This code has been extensively tested without magnetic fields^{19,20}. The arbitrary external magnetic field capability of PENELOPE was utilized by providing an efficient subroutine that looks up and interpolates the field map produced by a model of the non-uniform field of the solenoid magnet used in the experimental studies. The accuracy of the model will be described in section II.B.

2.2.1 Simulated setup

The high energy (G50) gantry of a two-gantry 50 MeV racetrack microtron accelerator (MM50 Scanditronix, Uppsala, Sweden) was used in the experiment¹⁴. We simulated the experiments for 20 MeV electron beams and 10 MV photon beams. Due to the high energy loss and scattering of electrons in materials, an accurate layout of all components in the beam path is required to do accurate simulations for electron beams. The gantry head was modeled with the following components: the beryllium vacuum exit window (0.0463 g/cm^2), the ion chamber made of gold and polyamide (0.0088 g/cm^2),

the tungsten scattering foil (0.193 g/cm^2), the mylar gantry exit window (0.0024 g/cm^2) and helium gas (0.0116 g/cm^2).

The electron beam source before the vacuum exit window was modeled with a monoenergetic pencil beam. In the experiment, a helium bag was placed between the gantry and the magnet to reduce beam scattering¹⁴. An aluminum collimator of 5.08 cm thickness and 5.00 cm aperture was placed in the front side of the solenoid magnet bore. The phantom was placed directly behind the aluminum collimator in the solenoid magnet bore. The front surface of the phantom was about 17.16 cm from the center of the solenoid magnet. The experiment was designed so that the magnetic axis and the electron beam axis were coincident. The peak value of the magnetic field was 3.03 T at the center of the magnet.

The overall setup used in the simulation is shown in Figure 2.1. Figure 2.2 shows the detailed setup near the phantom where, again, accurate information is needed for simulations using electron beams, especially when non-uniform magnetic fields with strong gradients are present. The constituents of the plastic phantom (density 0.984 g/cm^3) are polyolefin (50%), polyurethane (46%), inert pigment (2%) and molecular sieves (2%).

The film used to obtain depth-dose measurements in the experiment was Kodak XV Ready Pack. As shown in Figure 2.2, the phantom was a polyurethane cylinder cut into two pieces along its axis with the film placed in between. The film was horizontal and the film plane was 0.5 cm lower than the magnet axis as the diameter of the phantom was somewhat smaller than the diameter of the magnet bore.

A superconducting solenoid magnet²¹ (Intermagetics General Corporation, Guilderland, New York) with 20 cm diameter bore was used to produce a longitudinal field with a maximum strength of about 3.03 T. The center of the magnetic field was approximately 249 cm away from the vacuum exit window¹⁴ (Figure 2.1).

2.2.2 Magnetic field

The internal magnet configuration consists of solenoid coils of known dimensions²². The current density is approximated to be continuous in the finite cross section area of the coil regions hence the field can be numerically calculated with Biot and Savart Law. Since the magnet does not have a steel yoke, there is no hysteresis present, and the magnetic field scales directly in proportion to the current in the solenoid coil. The calibration curve is given in the manual of the magnet. The magnetic field strength at the center of the magnet was 3.03 T in the experiment. The calculated values along the axis are compared with the measured data in Figure 2.3 and they agree to within 3% up to ± 1 m from the center of the solenoid. Comparisons of off-axial longitudinal field strength measurements and calculations at several different axial positions were also made in Ref. 21. The calculated and measured values agree to within 2% inside the cryostat radius and within 5% out of the cryostat radius. The magnetic field strength and field lines are shown in Figure 2.4. The calculated field profile is then stored in a look-up table. An interface subroutine was then written to make these data accessible to PENELOPE.

Different from the approximation used in this paper, the coils were approximated with an infinitely thin cylindrical current sheet to calculate the magnetic field in Ref. 14, which lead to differences near the coil regions compared with Figure 2.4. The bore of the magnet is 20 cm in diameter and aperture of the collimator is 5 cm. Since the coils were blocked by the collimator and the shell of the magnet, the electrons could not reach this area. The closer to the axis, the smaller the difference is between these two models. These two approximations gave almost identical results near the axis if properly normalized.

Dose calculations with the magnetic fields produced by these two approximations showed little difference.

Confinement using a longitudinal field is quite different than that using a transverse magnetic field which also has been suggested^{2-6, 23}. While a transverse beam can provide confinement, it also will deflect, rather than focus, the incident electron beam. In contrast, a longitudinal field generated by a solenoid magnet on the beam axis acts as a simple magnetic lens and provides both focusing (for the primary electrons) and confinement (for the secondary electrons) without deflecting the primary beam.

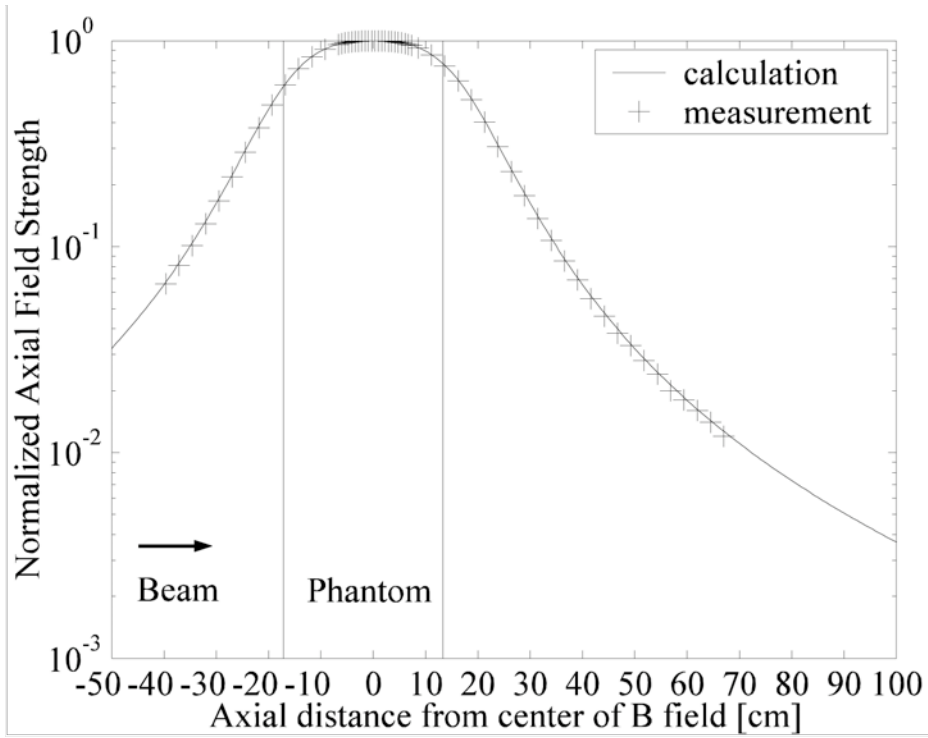


Figure 2.3 The solenoid magnetic field along the central axis

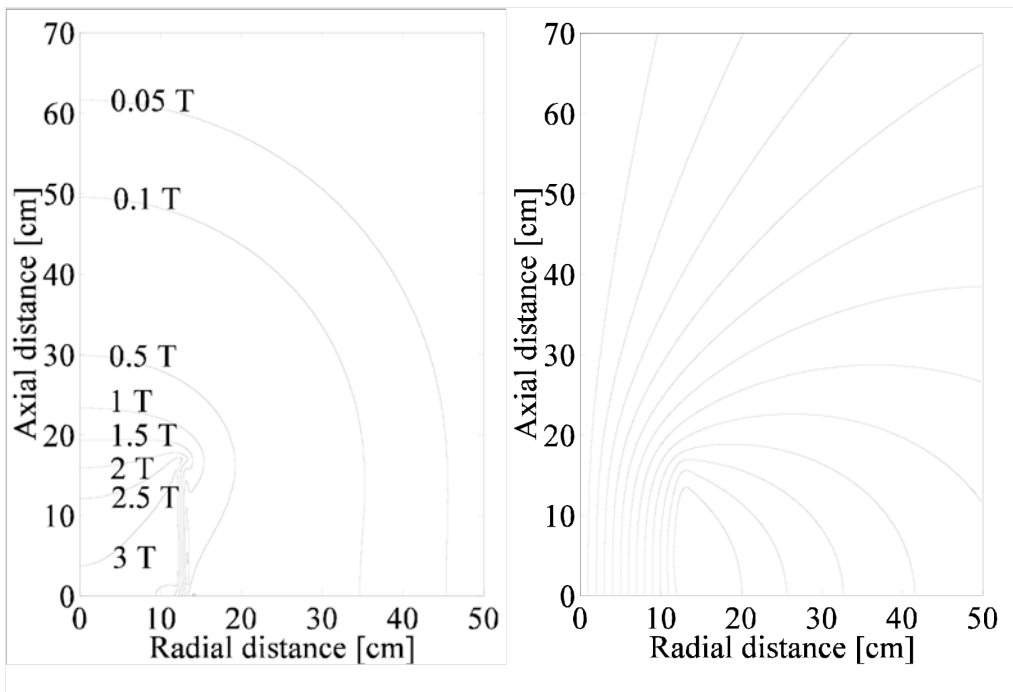


Figure 2.4 The magnetic field strength distribution (left) and field lines (right)

2.2.3 Normalization of the simulations to the measurements

The optical density of the film after irradiation was digitized and calibrated such that the optical density of the film is proportional to the dose¹⁴. Let $f(r, z)$ be the measured dose obtained from the film and $d(r, z)$ the calculated value from the MC simulation.

We expect

$$f(r, z) = kd(r, z), \quad (2.1)$$

where k is a normalization constant. Assume Eq. (1) is valid for any point of interest in the film.

$$\text{Define the error as } Err = \sum_{i,j} [f(r_i, z_j) - kd(r_i, z_j)]. \quad (2.2)$$

In the above expressions, $f(r_i, z_j)$ is the film data interpolated at the same position as for $d(r_i, z_j)$. Find k that minimizes Err , i.e. $\frac{dErr}{dk} = 0$. The summation is done over all the points that are within preset lower and upper limits. The lower limit was set to be 10% of the maximum dose while the upper limit was set to be 100% of the maximum dose. The reason to choose these numbers as the cutoffs is as follows. The XV film does not respond linearly over the whole range of interest, especially at high doses where it starts to saturate. Light leakage may affect the measurement of the very-low-dose region. Some artifacts can be seen in the dose plot for the case without magnetic field, which occurs where the dose is lower than that with the magnetic field. Since the highest dose in

the experiment was still less than the saturation dose of the film, we set the upper limit to be 100%.

2.3 Results

2.3.1 Electron beams

A. Electron beam dose distribution when magnetic field $B=0$ T

The stated energy of the electron beam could not exactly be verified in the experiment and was only known to about $\pm 10\%$ from the accelerator settings. Thus in the MC simulation, the first step was to determine the best-fit electron beam energy. This was done using the data taken without a magnetic field i.e. $B = 0$ T. The actual beam energy was determined to be 21.6 MeV. This energy differs from the nominal energy 20 MeV used in the experiment as determined from the accelerator setting but this also has been found by other investigators²⁴. Similar problems also were found in other medical accelerators²⁵. This energy then was also used for the simulation when the magnetic field was applied.

The MC simulations are compared with measurements in Figure 2.5 and the differences are shown in Fig. 6. One hundred million histories were simulated to make the statistical uncertainty smaller than 3% of the maximum dose everywhere (Figure 2.6). We are primarily interested in the region where the dose ranges from 10% to 100% of the maximum dose and we can see from Figure 2.7 that most of the simulation values agree with the measurement within a few percent in that region. The depth-dose curves at several radial positions are displayed in Figure 2.8. The simulation agrees with the

measurement reasonably well in the region 1 cm away from the phantom surface. The radial dose profiles at different depths are shown in Figure 2.9. Without additional measurements of the dose in the first 1 cm, it is difficult to know the cause of the discrepancies between the model and the measurements in this region. Alignment of the sealed ready-pack film in the phantom is a potential source of error for the measurements.

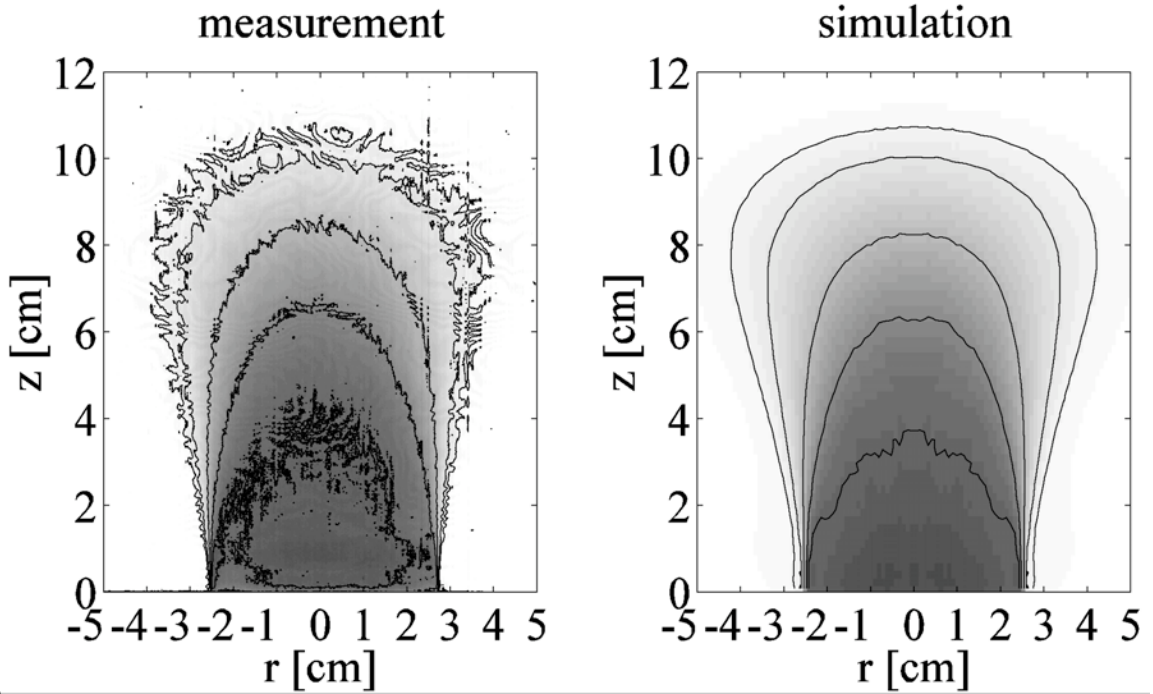


Figure 2.5 Two-dimensional plot of 21.6 MeV electron dose profiles for $B=0$ T. Artifacts can be seen in the very low dose region (left). The 10%, 20%, 50%, 80% and 100% isodose lines are shown. The dose is scaled to 100% at 3 cm on the central axis.

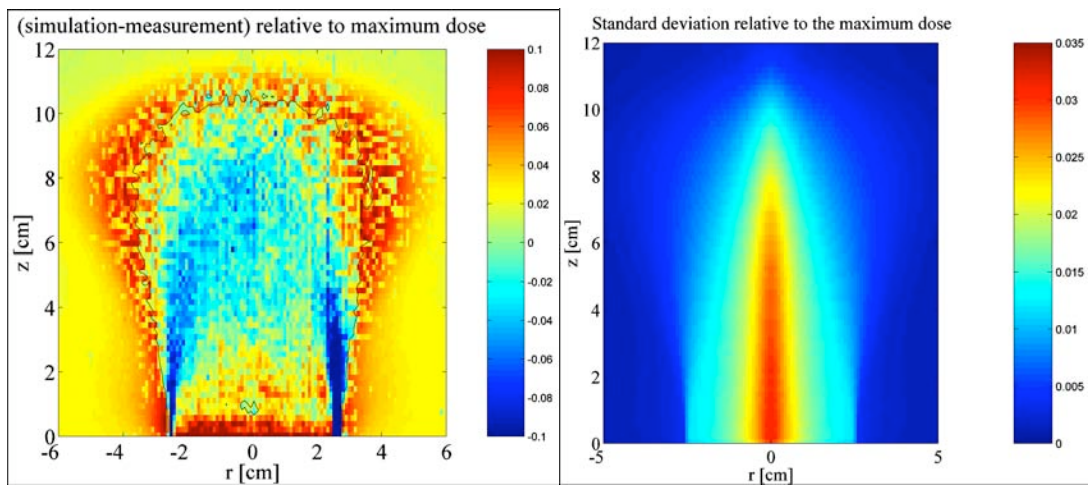


Figure 2.6 The difference between the simulation and the measurement (left) together with the statistical uncertainty of the simulation for $E=21.6$ MeV and $B=0$ T (right).

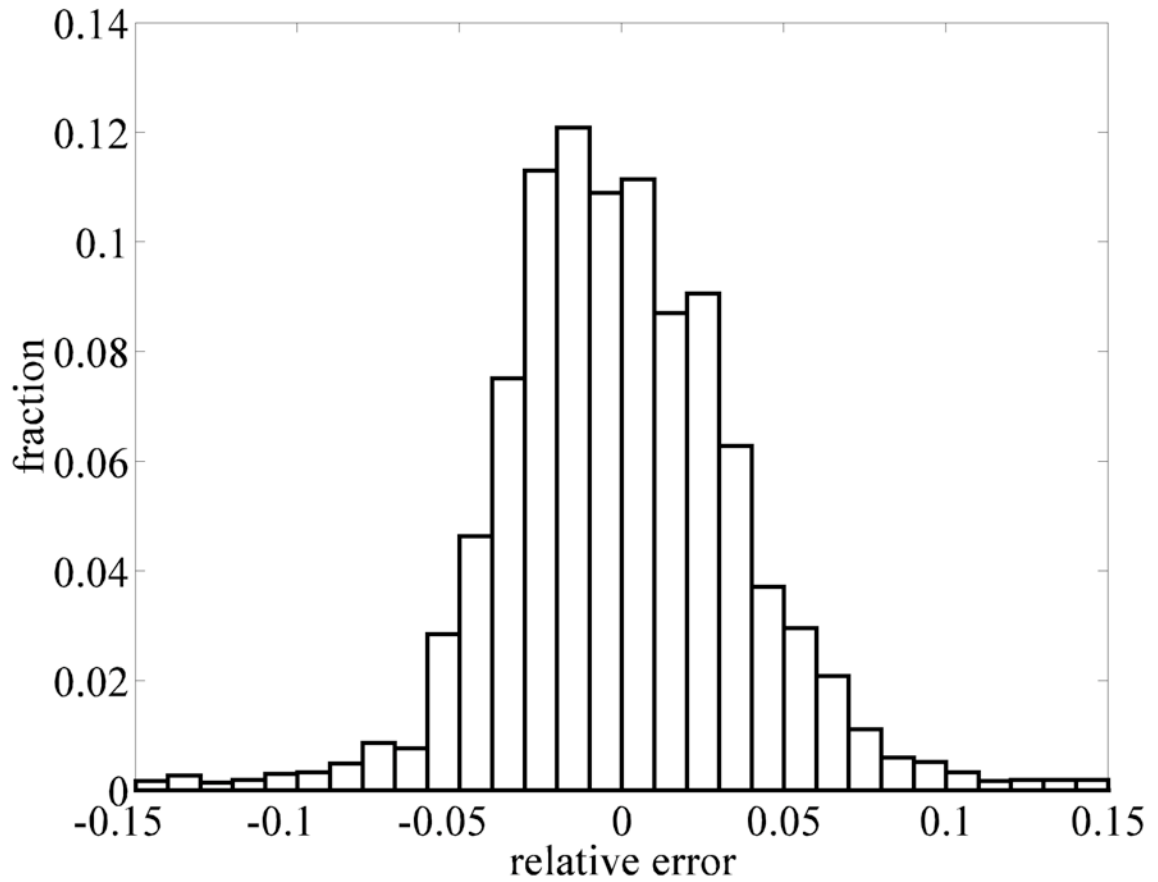


Figure 2.7 The relative error (i.e. difference between MC simulation and experiment relative to the maximum dose) is tallied in the region where the dose lies in between the lower threshold 10% and the upper threshold 100% of the maximum dose. This histogram shows the fraction of the simulated data points with a certain relative error for $E=21.6$ MeV and $B=0$ T.

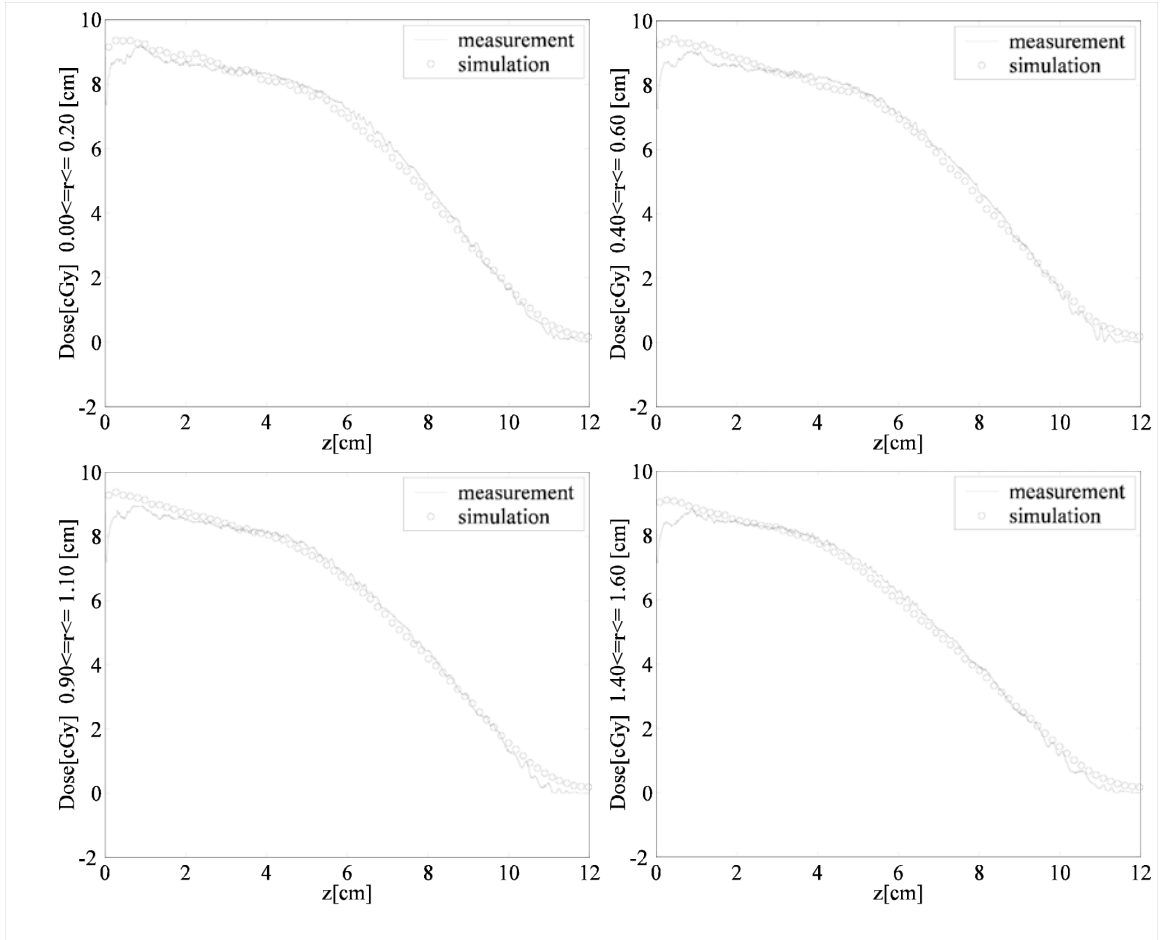


Figure 2.8 The measured and simulated electron beam depth dose curves at central axis, 0.5 cm, 1.0 cm and 1.5 cm away from the central axis for $E=21.6$ MeV and $B=0$ T.

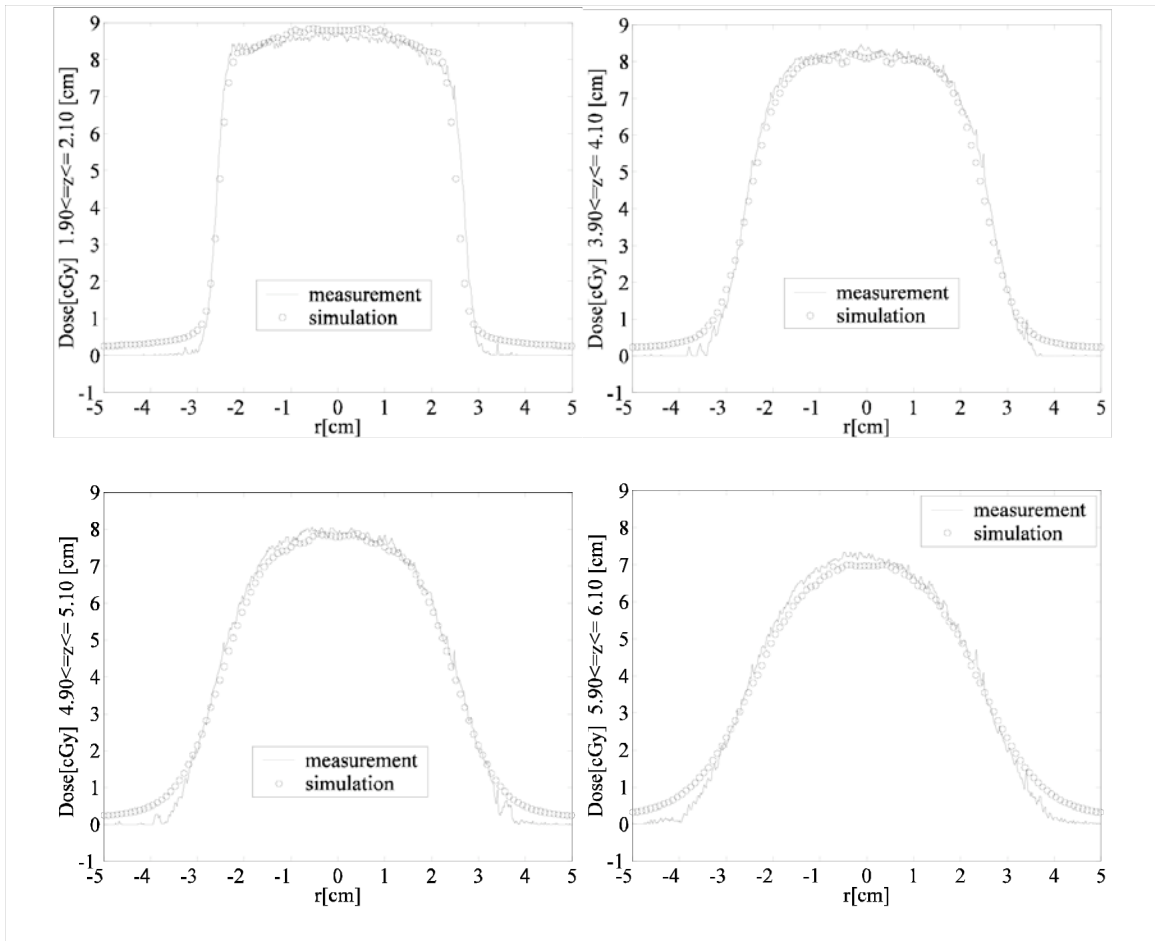


Figure 2.9 The measured and simulated electron radial dose profiles at depth 2 cm, 4 cm, 5 cm and 6 cm for $E=21.6$ MeV and $B=0$ T.

B. Electron beam dose distribution when a longitudinal magnetic field is applied

The strength of the magnetic field at the center of the magnet was 3.03 T. Sixty million histories were simulated resulting in the statistical uncertainties smaller than 1.5% over the region of interest. The focusing effect in the dose profile of the electron beam is satisfactorily reproduced in the MC simulations (Figures 2.10-2.14). As expected, in the longitudinal non-uniform magnetic field, it is observed that the electron dose can be focused in both the transverse and longitudinal directions. In addition, some electrons can be reflected backwards due to the “mirror” effect²⁶ of the magnetic field, enhancing the local dose (Figure 2.15). The net result is that the high-dose region is now significantly confined in a much smaller volume when a strong longitudinal magnetic field is applied. The simulation agrees with the measurement quite well 1 cm from the surface into the phantom. Magnetic field data obtained with the thin sheet approximation were also tried to calculate the dose profiles. Similar results were obtained and the discrepancies in the region from the phantom surface until 1 cm deep could not be attributed to the small change of the magnetic field. Similar to the case without the magnetic field, additional measurements of the surface dose should be made in order to find the cause of the discrepancies.

Different dose profiles can be formed if the axial position of the phantom (or of course the patient) can be changed while the beam energy and the strength of the magnetic field are fixed. Our MC simulations show that the longitudinal “squeezing” effect can be greater if the front surface of the phantom is about 15 cm away from the field center (Figure 2.16). The enhanced dose peak becomes sharper at this position

which implies that minimum spread-out of the dose can be achieved with a good combination of beam energy, field strength and displacement of the phantom/patient (or the field). Likewise, since the solenoid focusing the electron beam acts as a simple lens, displacing the object (incident beam) leads to a known displacement of the image (focused beam). Thus the electron beam can be scanned in the transverse plane as well as intensity modulated for radiation therapy. All of these appear to be clinically viable options in an actual treatment scenario.

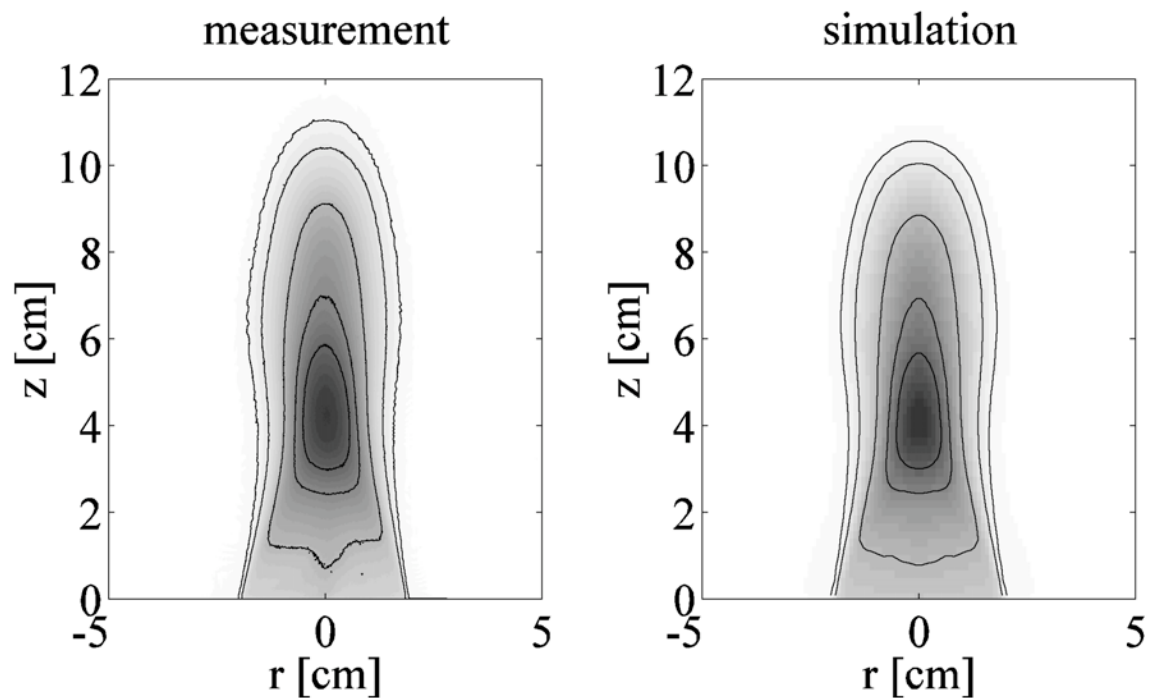


Figure 2.10 Two-dimensional plot of 21.6 MeV electron dose profiles for $B=3.03$ T. The magnetic field is along z axis. The 10%, 20%, 50%, 80% and 100% isodose lines are shown. The dose is scaled to 100% at 3 cm on the central axis.

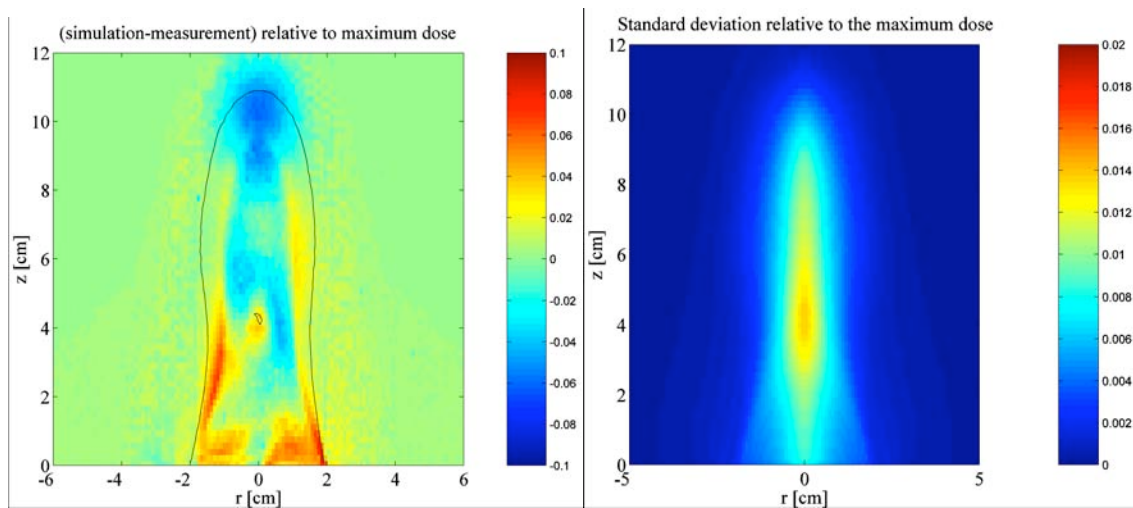


Figure 2.11 The difference between the simulation and the measurement (left) and the statistical uncertainty of the simulation for $E=21.6$ MeV and $B=3.03$ T.

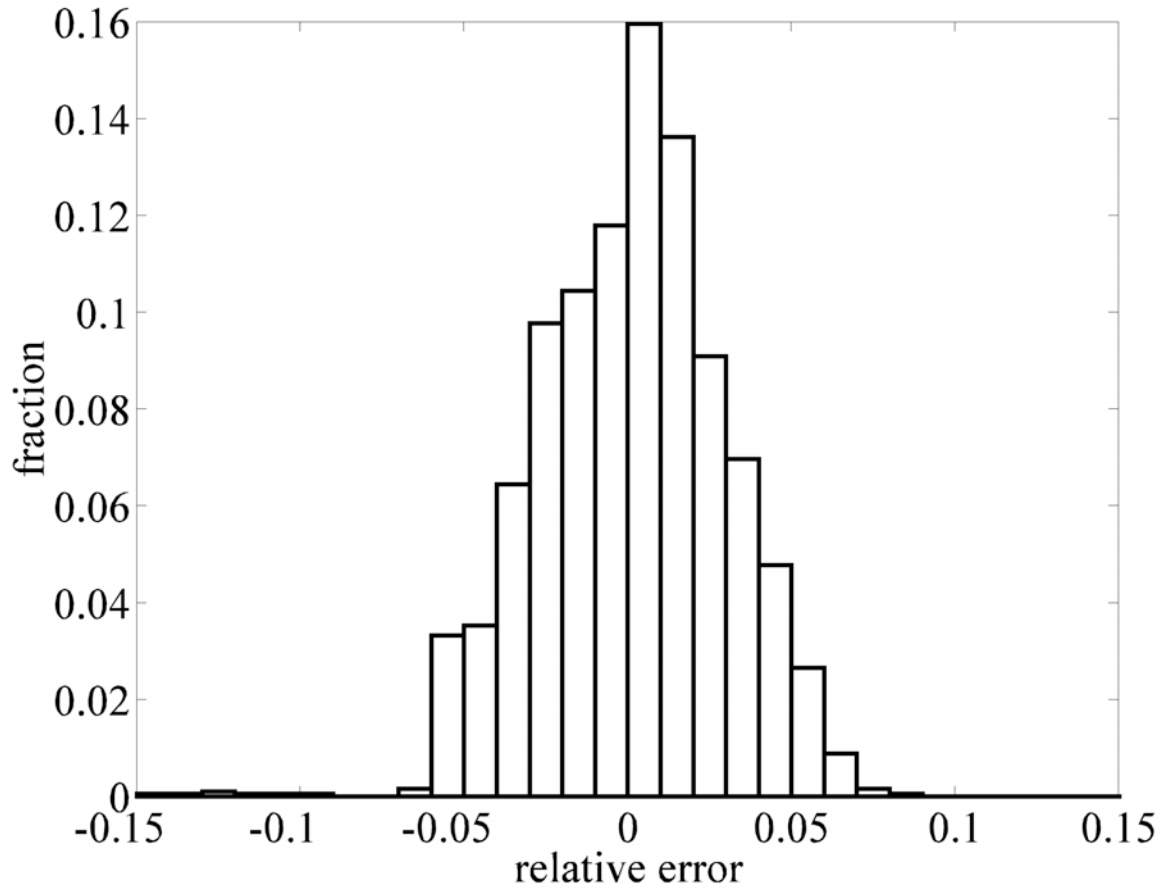


Figure 2.12 The relative error (i.e. difference between MC simulation and experiment relative to the maximum dose) tallied in the region where the dose lies in between the lower threshold 10% and the upper threshold 100% of the maximum dose. This histogram shows the fraction of the simulated data points with a certain relative error for $E=21.6$ MeV and $B=3.03$ T.

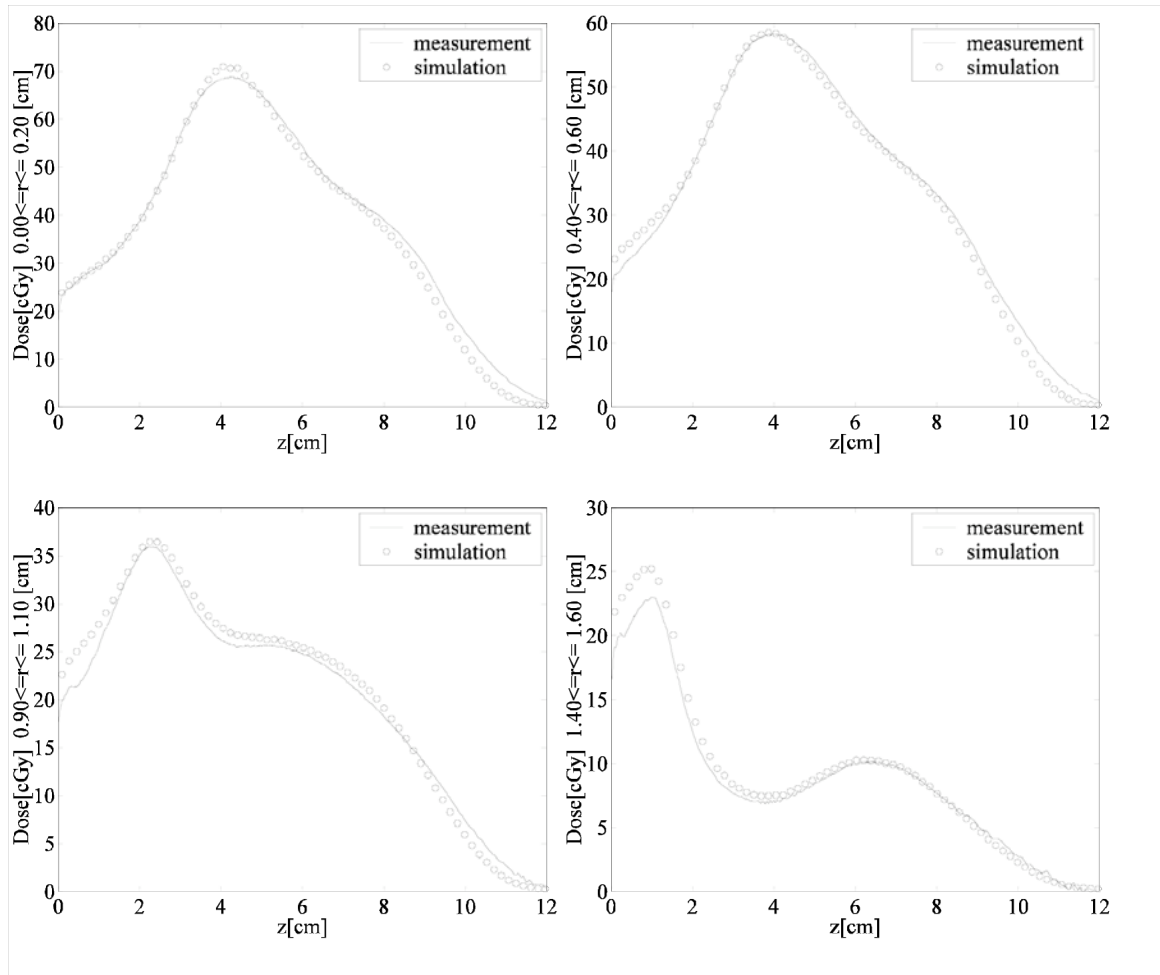


Figure 2.13 The measured and simulated electron depth dose curves along the central axis, 0.5 cm, 1.0 cm, and 1.5 cm away from the central axis for $E=21.6$ MeV and $B=3.03$ T.

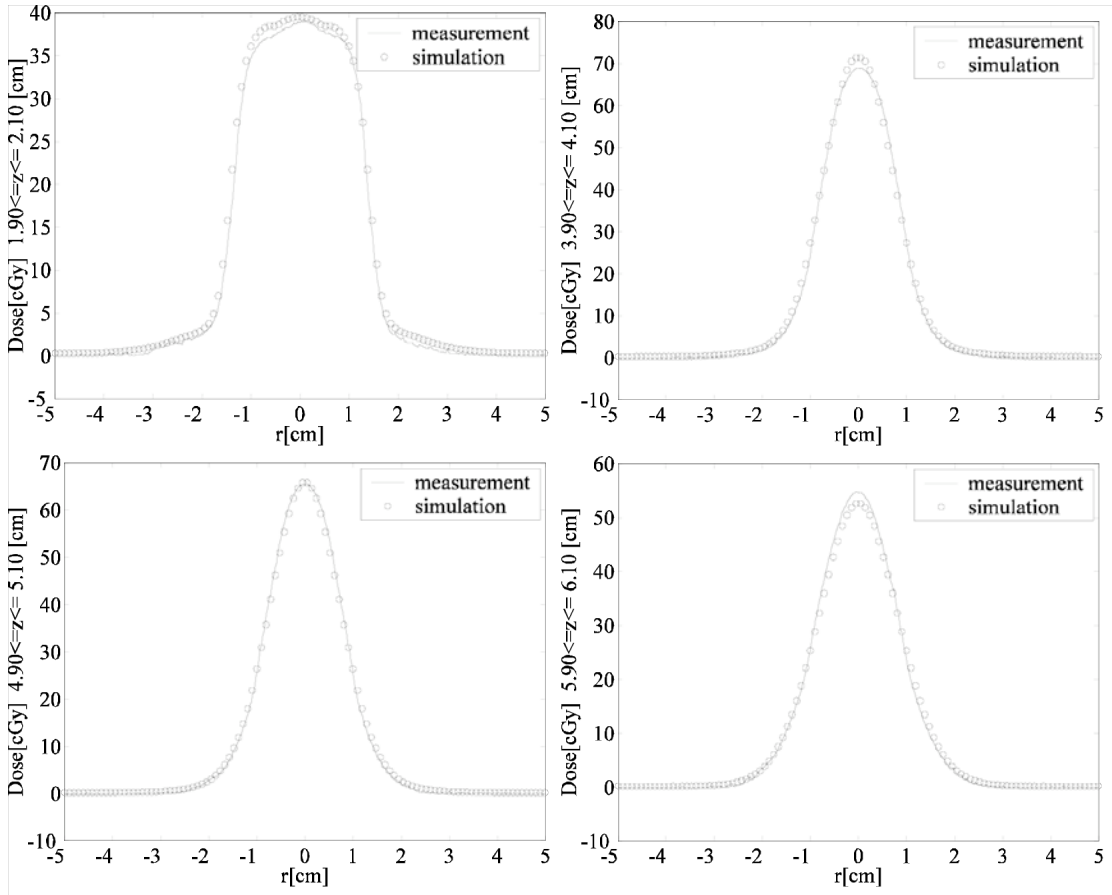


Figure 2.14 The measured and simulated electron radial dose profiles at depth 2 cm, 4 cm, 5 cm and 6 cm for $E=21.6$ MeV and $B=3.03$ T.

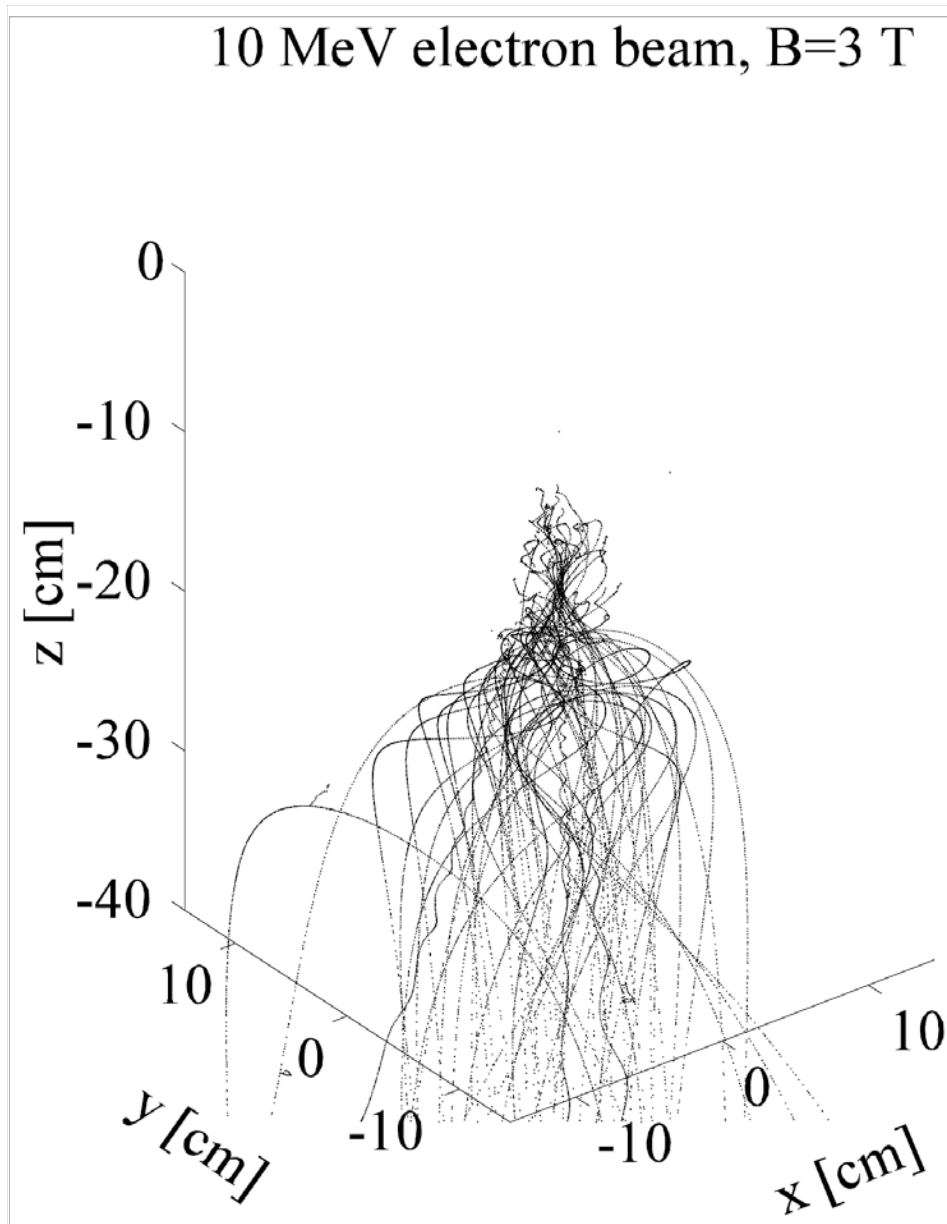


Figure 2.15 Three-dimensional plot of the electron tracks near and inside the phantom without the aluminum collimator. The front surface of the phantom is located at $z=-17.16$ cm. The magnetic field center is at the origin ($B=3$ T). The electron beam ($E=10$ MeV) goes in the positive z direction. Here we use 10 MeV instead of 20 MeV electrons to show the “mirror” effect prominently.

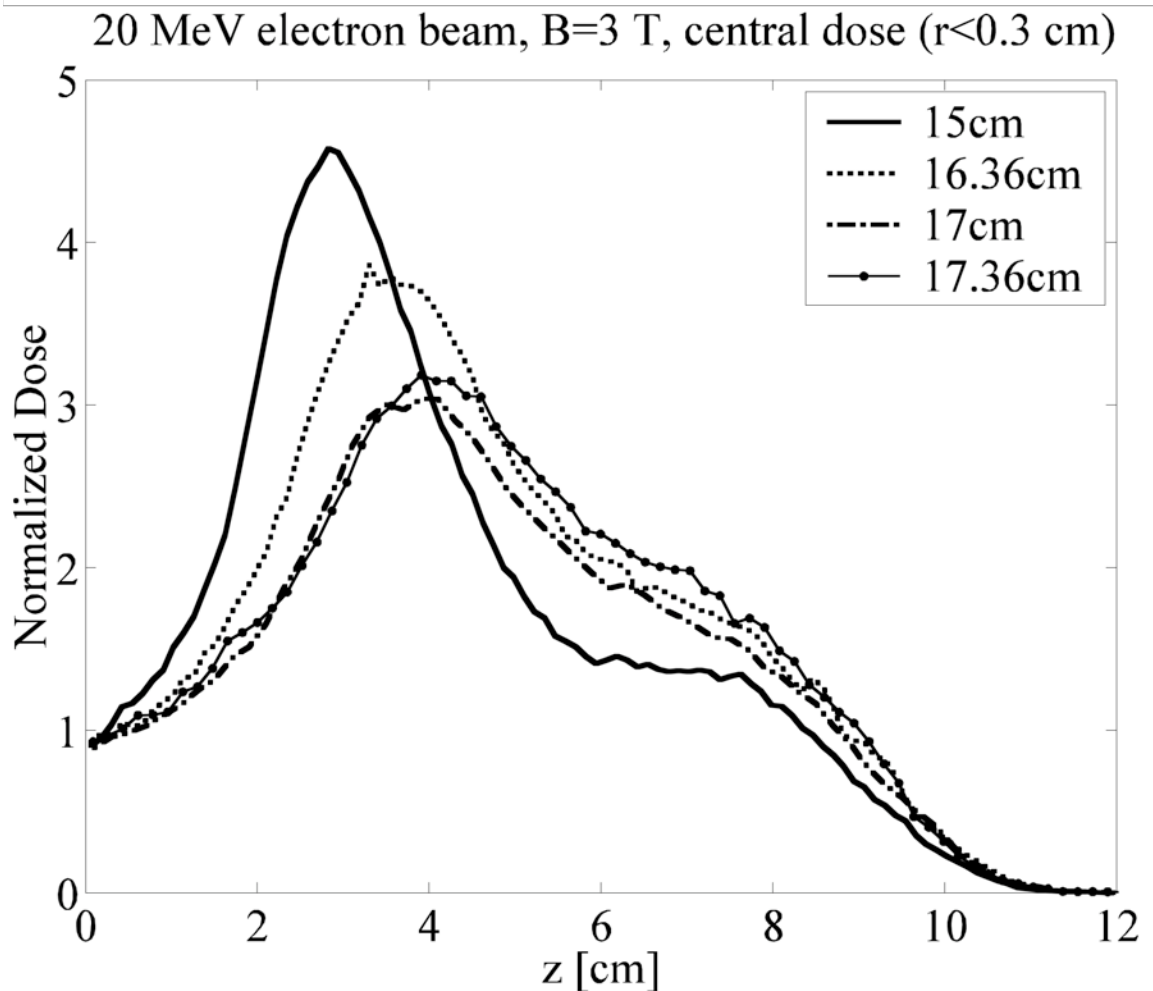


Figure 2.16 This graph shows the depth dose profiles when the phantom was placed at different longitudinal positions in the magnetic field, where electron energy is 20 MeV and B=3 T. A sharp peak in the dose profile can be formed at the optimal position.

2.3.2 Photon beams

In addition to the data for electron beam-dose profiles, the experiment¹⁴ also obtained limited data on magnetic confinement of the dose profile for photon beams. In this case the secondary electrons produced by the photons are confined by the magnetic field and hence so is the resulting dose. This potentially could be useful in photon beam therapy as often these secondary electrons can propagate through low-density regions creating extraneous dose to healthy tissue^{9, 10}. However, the experimental setup was not optimized to demonstrate the reduction of penumbra with magnetic confinement¹⁴. First, the thickness of the aluminum collimator was not enough to block the photon beam. Second, a large amount of scattered electrons produced in the surrounding air was trapped by the magnetic field and formed a high surface dose. Therefore, our simulation here is used only to reproduce and understand the experiment.

Since the exact geometry of the parts in the gantry head that generate photons was not known, the simulation starts from a photon source with a specific energy distribution, which is not verified with experiments. Nonetheless, the present MC simulations again appear to reproduce qualitatively the existing experimental data¹⁴ (Figure 2.17). However, as noted, the data were taken with the uniform-density phantom. It thus does not clearly demonstrate that the longitudinal magnetic field can enhance the dose in low-density regions. Additional data using a non-uniform (*e.g.* a tissue-lung) phantom are needed to provide a more stringent test of the MC simulations.

It was noted that in the experiment the surface dose for the photon beam was intensified when the magnetic field was applied¹⁴. The present calculations show that this

was due to the magnetic field trapping and focusing scattered secondary electrons that were produced in the air by the incident photon beam. Our simulation shows that the surface dose decreases if the volume of surrounding air is reduced.

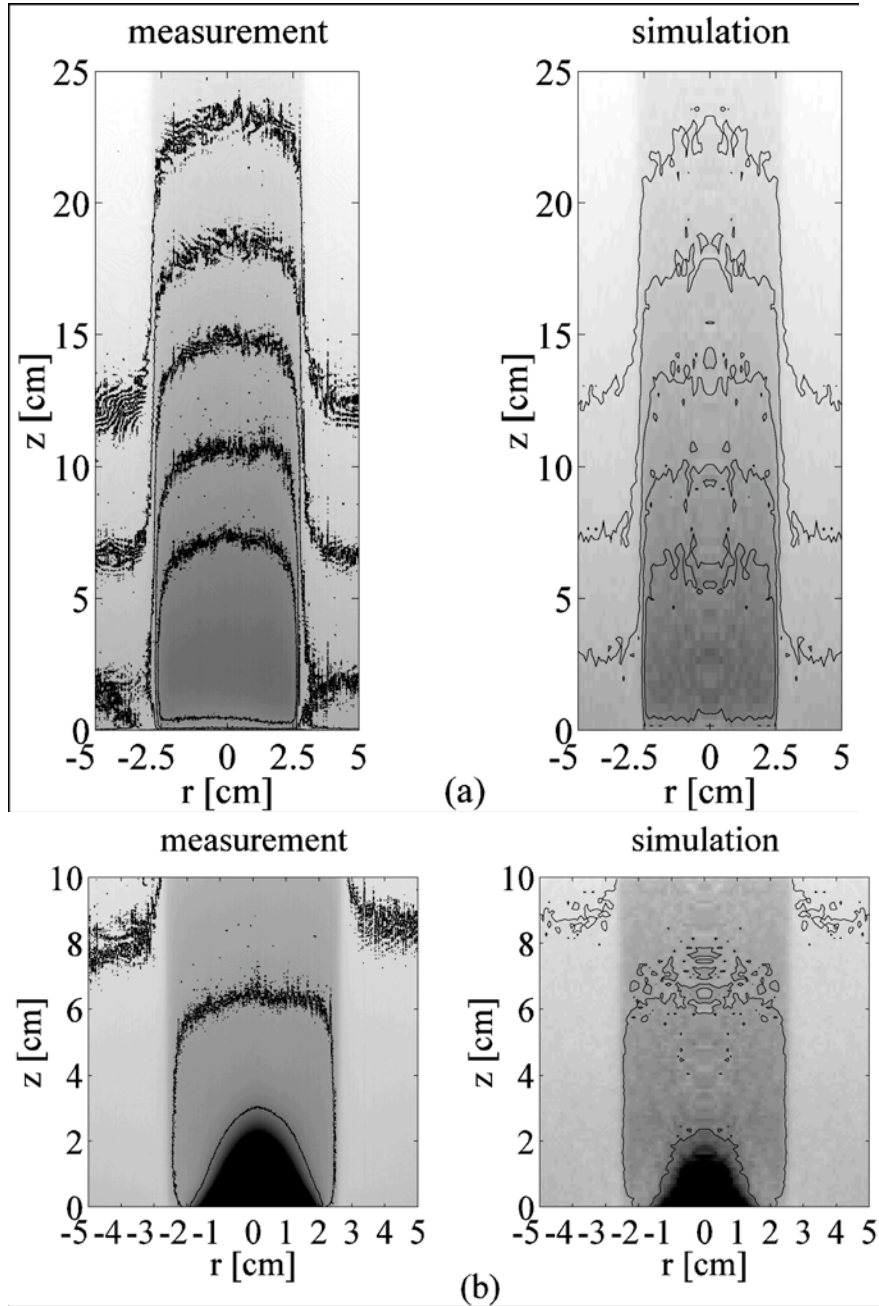


Figure 2.17 10 MV photon beam dose distributions (a) Comparison of the experimental result (left) with the simulation (right) for $B=0$ T. The 50%, 60%, 70%, 80% and 90% isodose lines are shown. The dose is scaled to 100% at 3 cm on the central axis. (b) Comparison of the experimental result (left) with the simulation (right) for $B=3.03$ T. The 50%, 80% and 100% isodose lines are shown. The dose is scaled to 100% at 3 cm on the central axis.

2.4 Discussion

2.4.1 Simulation of multi-beam electron dose profiles

Since relatively compact electron accelerators, with energy of 20 MeV to 100 MeV, together with large-bore, high-field superconducting solenoid magnets are either commercially available now or feasible in the near future¹⁵, we have done simulations in order to further demonstrate the possibilities of magnetically-confined electron-beam radiation therapy. As an example, we have done a simple simulation of a multi-beam stereotactic treatment dose profile with 35 MeV electron beams, which would be typical of a modest-size microtron adapted for clinical use. 20 MeV electron beams are not energetic enough to treat a position as deep as 10 cm. A skull plus tissue phantom was modeled as 0.6 cm thick bone followed by uniform tissue in a 20 cm diameter phantom set edge-wise to a magnetically-confined electron beam. Six electron beams each with energy of 35 MeV were used with a longitudinal solenoid magnetic field of 6 T. The latter was suitably arranged together with aluminum collimator of 2 cm aperture to provide optimal dose at the center of the skull-tissue phantom (Figure 2.18). As can be seen in the simulations, it appears possible to provide a very high dose in a relatively small volume while avoiding critical regions (Figure 2.19). The dose peak was the superposition of the six individual confined doses. Without the magnetic field, the dose would spread out in the region. As seen from a comparison between Figure 2.18 (a) and Figure 2.18 (b), the dose after the hot spot was greatly reduced in the case of electron beams. Even stronger fields lead to better dose confinement [Figure 2.18 (b)-(d)]. As indicated by Figure 2.16, the position of the phantom in the magnetic field can

significantly affect the dose profile. The dose near the entrance in Figure 2.18 (d) was increased due to the increase of the magnetic field strength. The position of the phantom in the magnetic field could be tuned to reduce the dose near the entrance. All these factors should be taken into consideration in a real treatment planning system.

Again, of course, experimental data would provide a more stringent test of this but these simulations suggest that magnetically-confined electron beams using high-field solenoids effectively could be used in multi-beam stereotactic treatments. A common on-site electron accelerator facility could be used to provide both magnetically-confined photon and electron beam radiation therapy treatment. The issue of providing a suitable magnetic-field configuration in a clinical setting has previously been discussed¹⁵. Very-large-bore, high-field superconducting solenoids including split-coil magnets are commercially available with some systems requiring no cryogenics (LN or LHe). The latter are particularly well suited for mounting on a gantry suitable for stereotactic treatment. The patient could be placed between the Helmholtz coil pair during the treatment much like those in open bore MRI scanners. Also, it recently has been shown that an array of permanent magnets can be utilized to provide magnetic collimation for electrons²⁷. As noted earlier, unlike a transverse magnetic field, a longitudinal magnetic field does not deflect the incident primary electron beam, hence the magnet can be an integral part of the electron accelerator gantry.

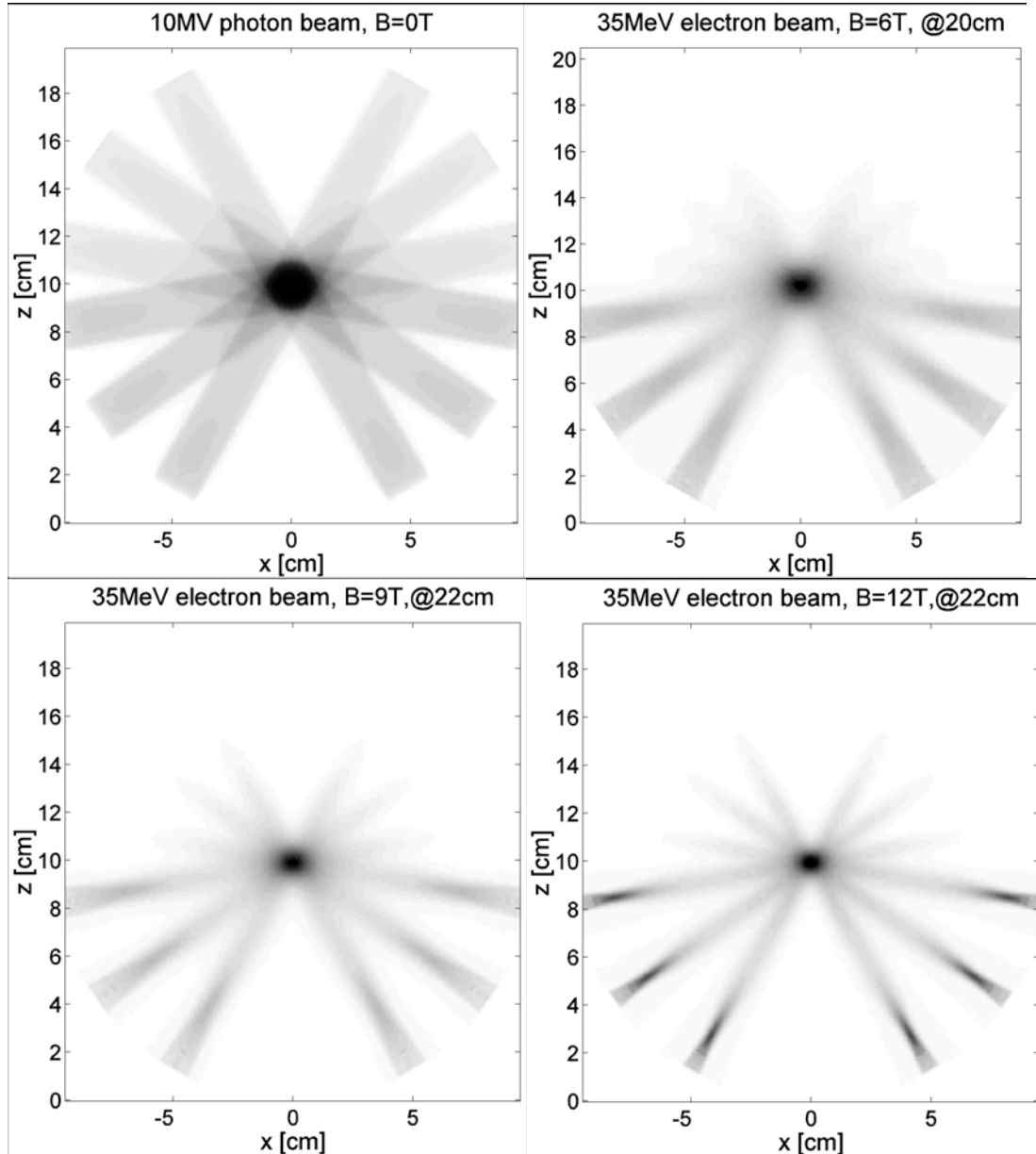


Figure 2.18 (a) upper left: dose profile for 10 MV photon beams. (b) upper right: dose profile for 35 MeV electron beam in 6 T solenoid magnetic field. (c) lower left: dose profile for 35 MeV electron beam in 9 T solenoid magnetic field. (d) lower right: dose profile for 35 MeV electron beam in 12 T solenoid magnetic field. We can see the effect of increasing the strength of the magnetic field from (b) to (d). [(a)-(d) all have the same aperture of the aluminum collimator.]

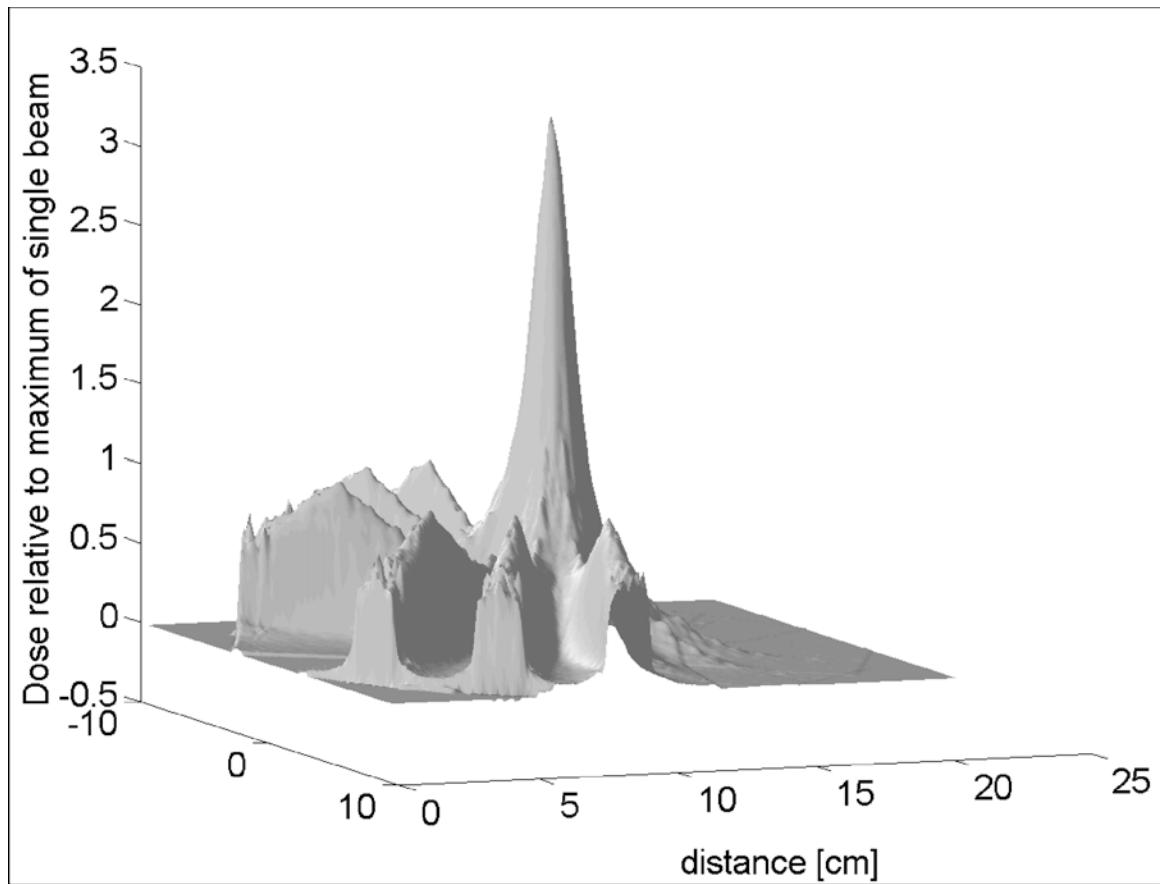


Figure 2.19 Two-dimensional dose plot of the multi-beam 35 MeV electron dose profile with a 6 T solenoid magnet

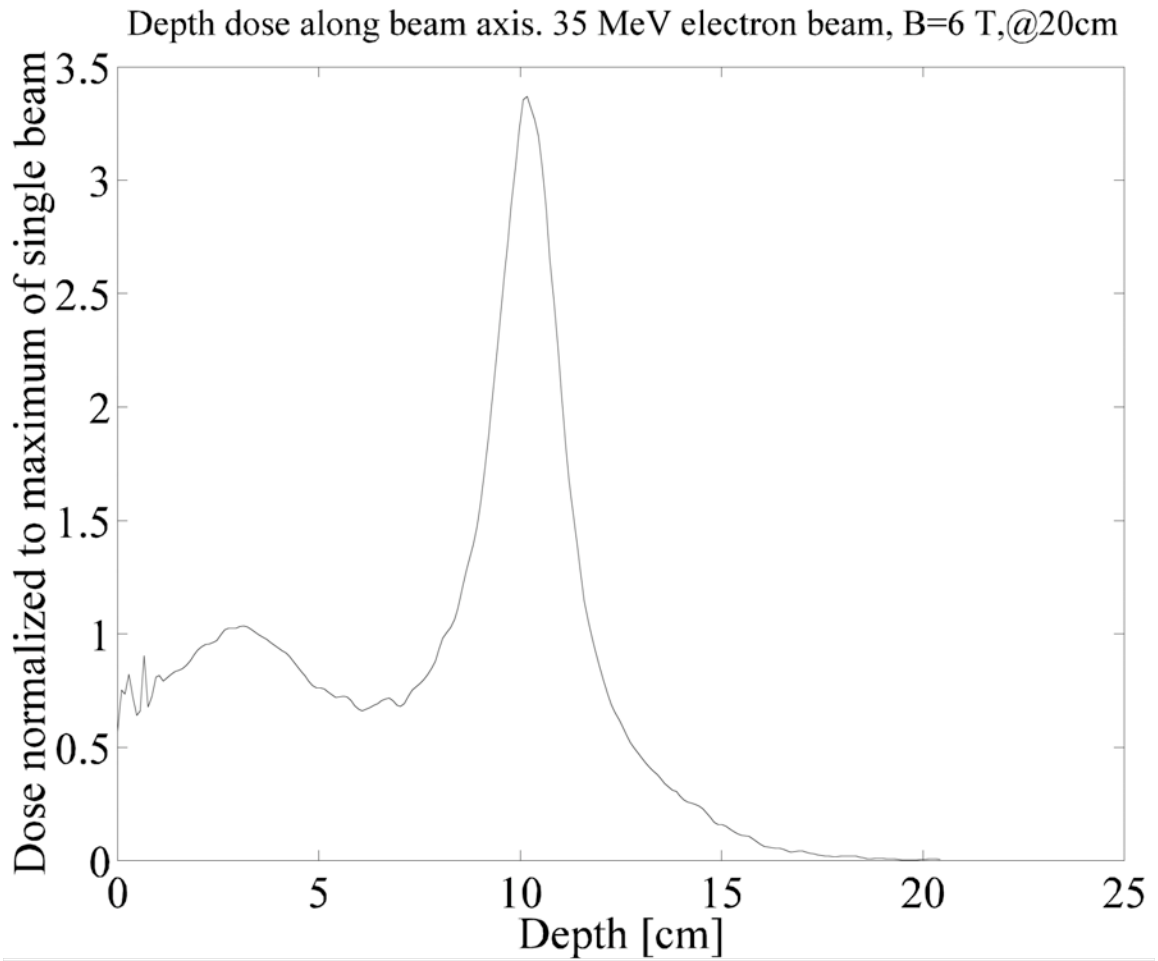


Figure 2.20 The dose along a beam axis with electron energy of 35 MeV and peak value of the solenoid magnetic field 6 T

2.4.2 Possible dependence of relative biological effectiveness (RBE) on magnetic fields

As previously noted by others^{3,6,8}, since the trajectories of the low-energy secondary electrons primarily responsible for radiation damage and hence the RBE are altered in the presence of high magnetic fields, it is possible that RBE may depend on the magnetic field. If this is the case, RBE as a function of the field strength B would need to be determined and modeled for any magnetically-confined radiation therapy beam. While a few measurements of this type have been done^{28,29}, more complete measurements are needed.

2.5 Conclusion

The experimental dose profiles are generally reproduced in the simulation to within a few percent. By comparing the simulations with the experiments, we demonstrate that the non-uniform longitudinal magnetic field generated by a solenoid can provide both transverse and longitudinal confinement of an electron beam dose profile. The “3D” confinement results from focusing effect of the magnetic lens, reduction of lateral scattering of the electrons, and the mirror effect of the magnetic field. Our results show that the MC code PENELOPE has the basic capability of calculating the dose with realistic magnetic fields. However, the primary electron beam energy and the beam-line geometry need to be carefully verified and modeled in order to get an accurate simulation.

From our simulations, we can see that electron dose profiles can be manipulated by the appropriate combination of the beam energy, the strength of the magnetic field, and the position of the target media in the magnetic field. Stereotactic treatment appears possible using magnetically-confined electron beams. The physical collimation and the magnetic confinement have to be suitably adjusted to optimize the dose profile. Since intense primary electron beams are readily available, a high dose rate can be obtained.

Acknowledgements

We would like to thank Indrin Chetty for providing us the geometry of some of the components inside the gantry head. This work is supported by a Munn Foundation Grant from the University of Michigan Comprehensive Cancer Center and NSF Grants PHY-02-44989 and 03-54828.

References to Chapter 2

- ¹ W. H. Bostick, "Possible techniques in direct-electron-beam tumor therapy," *Phy. Rev.* **77**, 564-565 (1950)
- ² C. C. Shih, "High energy electron radiotherapy in a magnetic field," *Med. Phys.* **2**, 9-13 (1975)
- ³ D. P. Whitmire, D. L. Bernard, M. D. Peterson, and J. A. Purdy, "Magnetic enhancement of electron dose distribution in a phantom," *Med. Phys.* **4**, 127-131 (1977)
- ⁴ D. P. Whitmire, D. L. Bernard, and M. D. Peterson, "Magnetic modification of the electron-dose distribution in tissue and lung phantoms," *Med. Phys.* **5**, 409-417 (1978)
- ⁵ R. Nath and R. J. Schulz, "Modification of electron-beam dose distribution by transverse magnetic fields," *Med. Phys.* **5**, 226-230 (1978)
- ⁶ B. R. Paliwal, A. L. Wiley, Jr., B. W. Wessels, and M. C. Choi, "Magnetic field modification of electron-beam dose distributions in inhomogeneous media," *Med. Phys.* **5**, 404-408 (1978)
- ⁷ M. S. Weinhaus, R. Nath, and R. J. Schulz, "Enhancement of electron beam dose distributions by longitudinal magnetic fields: Monte Carlo simulations and magnet system optimization," *Med. Phys.* **12**, 598-603 (1985)
- ⁸ A. F. Bielajew, "The effect of Strong Longitudinal magnetic fields on dose deposition from electron and photon beams," *Med. Phys.* **20**, 1171-1179 (1993)
- ⁹ S. J. Wadi-Ramahi, S. A. Naqvi, J. C. H. Chu, "Evaluating the effectiveness of a longitudinal magnetic field in reducing underdosing of the regions around upper respiratory cavities," *Med. Phys.* **28**, 1711-1717 (2001)
- ¹⁰ S. A. Naqvi, X. A. Li, S. W. Ramahi, J. C. Chu, and S. Ye, "Reducing loss in lateral charged-particle equilibrium due to air cavities present in x-ray irradiated media by using longitudinal magnetic fields," *Med Phys.* **28**, 603-611 (2001)
- ¹¹ L. Reiffel, A. Li, J. Chu, R. W. Wheatley, S. Naqvi, R. Pillsbury and A. Saxena, "Control of photon beam dose profiles by localized transverse magnetic fields," *Phys. Med. Biol.* **45**, N177-N182 (2000)
- ¹² X. A. Li, L. Reiffel, J. Chu, and S. Naqvi, "Conformal photon-beam therapy with transverse magnetic fields: Monte Carlo study," *Med. Phys.* **27**, 1447 (2000)

-
- ¹³ D. Jette, "Magnetic fields with photon beams: Monte Carlo calculations for a model magnetic field," *Med. Phys.* **27**, 2726-2738 (2000)
- ¹⁴ D. W. Litzenberg, B. A. Fraass, D. L. McShan, T. W. O'Donnell, D. A. Roberts, F. D. Becchetti, A. F. Bielajew, J. M. Moran, "An Apparatus for Applying Strong Longitudinal Magnetic Fields to Clinical Photon and Electron Beams", *Phys Med Bio* **V46** no. 5, pp. N105-N115, (2001)
- ¹⁵ F. D. Becchetti, D. W. Litzenberg, J. M. Moran, T. W. O'Donnell, D. A. Roberts, B. A. Fraass, D. L. McShan, and A. F. Bielajew, "Magnetic Confinement of Radiotherapy Beam-Dose Profiles", *Proc. Cyclotrons and Their Applications 2001, Sixteenth International Conference (AIP Press)* pp. 44-46
- ¹⁶ F. D. Becchetti, J. M. Sisterson, W. R. Hendee, "Point/Counterpoint: High Energy Electron Beams Shaped with Applied Magnetic Fields Could Provide a Competitive and Cost-effective Alternative to Proton and Heavy-ion Radiotherapy," *Med. Phys.* **29** , 2435-2437 (2002)
- ¹⁷ J. Baró, J. M. Fernández_Varea and F. Salvat, "PENELOPE: an Algorithm for Monte Carlo Simulation of the Penetration and Energy Loss of Electrons and Positrons in Matter," *Nuclear Instruments and Methods* **VB100**, 31-46 (1995)
- ¹⁸ J. Sempau, E. Acosta, J. Baró, J. M. Fernández_Varea and F. Salvat, "An Algorithm for Monte Carlo simulation of coupled electron-photon transport", *Nuclear Instruments and Methods Research B* **132** 377-390 (1997)
- ¹⁹ J. Sempau, A. Sánchez-Reyes, F. Salvat, H. Oulad ben Tahar, S. B. Jiang and J. M. Fernández-Varea, "Monte Carlo simulation of electron beams from an accelerator head using PENELOPE," *Phys. Med. Biol.* **46** 1163-1186 (2001)
- ²⁰ R. D. Stewart, W. E. Wilson, J. C. McDonald and D. J. Strom, "Microdosimetry properties of ionizing electrons in water: a test of the PENELOPE code system," *Phys. Med. Biol.* **47**, 79-88 (2002)
- ²¹ R. L. Stern, "Design and Utilization of an Air-core Superconducting-Solenoid Nuclear-Reaction-Product Spectrometer", Ph.D dissertation of the Department of Physics, the University of Michigan, pp 26-31 (1987)
- ²² W. Liu, "Production and use of radioactive ion beams for measurements of nuclear reactions," Ph. D dissertation of the Department of Physics, the University of Michigan, pp 17 (1990)

-
- ²³ E. Nardi, G. Barnea and C. Ma, "Electron beam therapy with coil-generated magnetic fields", *Med. Phys.* **31**, 1494-1503 (2004)
- ²⁴ I. J. Chetty, J. M. Moran, T. S. Nurushev, D. L. McShan, B. A. Fraass, S. J. Wilderman and A. F. Bielajew, "Experimental validation of the DPM Monte Carlo code using minimally scattered electron beams in heterogeneous media," *Phys. Med. Biol.* **47**, 1837-1851 (2002)
- ²⁵ D. Sheikh-Bagheri and D. W. O. Rogers, "Sensitivity of megavoltage photon beam Monte Carlo simulations to electron beam and other parameters," *Med. Phys.* **29**, 379-390 (2002)
- ²⁶ J. D. Jackson, "Classical Electrodynamics," third edition, ISBN 0-471-30932-X, pp 594-596
- ²⁷ L. Ma, "Dosimetric properties of magnetically collimated electron beams for radiation therapy," *Med. Phys.* **31**, 2973-2977 (2004)
- ²⁸ R. Nath, R. J. Schulz and P. Bongiorni, "Response of mammalian cells irradiated with 30MV X-rays in the presence of a uniform 20-kilogauss magnetic field," *Int. J. Radiat. Biol.*, Vol. **38**, No. 3, 285-292 (1980)
- ²⁹ S. Rockwell, "Influence of a 1400-gauss magnetic field on the radiosensitivity and recovery of EMT6 cells *in vitro*," *Int. J. Radiat. Biol.*, Vol. **31**, No. 2, 153-160 (1977)

Chapter 3

The effect of the magnetic field on the relative biological effectiveness (RBE)

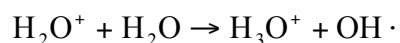
3.1 Theory of RBE

A brief overview of the theories about radiation damage and repair is given in this section. Factors that can affect RBE also are listed. Then the possibility of the effect of the magnetic field on RBE is discussed.

3.1.1 DNA damage and repair

A. Direct and indirect action of radiation

Many studies^{1,2,3} shows that the biological effects of radiation result principally from damage to DNA which is the critical target. When atoms of the target are ionized or excited, the chain events that lead to a biological change are initiated. When the energy is absorbed in biological material, there is a possibility that it will directly interact with the critical targets in the cells. This is called direct action of radiation. It is the dominant process if the radiation has a high LET. On the other hand, the radiation particle may interact with other molecules in the cells, such as water, to produce free radicals. A water molecule can be ionized to produce an ion radical: $\text{H}_2\text{O} \rightarrow \text{H}_2\text{O}^+ + \text{e}^-$. The ion radical reacts with another water molecule to form the highly reactive hydroxyl radical (OH·):



These radicals can diffuse far enough to reach and damage the critical targets. This is called indirect action of radiation. It is estimated about two thirds of the x-ray damage to DNA in mammalian cells is caused by the hydroxyl radicals⁴. This is the dominant process in low LET radiation damage.

B. DNA strand breaks and chromosome aberrations

Since DNA is the critical target for the biological effect of radiation, damage to it may lead to cell killing, mutation and carcinogenesis, etc. DNA damage leads to single-strand break and double-strand break. Single-strand breaks can be repaired readily using the other strand as a template (Figure 3.1). It may result in a mutation if the repair is incorrect. If the breaks on the two strands are well separated, they also are readily repaired just like two separate single-strand breaks.

Nevertheless, if the breaks in the two strands are opposite one another or separated by only a few base pairs, they may lead to a double-strand break (Figure 3.1). The double strand breaks are the most important lesion produce by radiation. The interaction of two double-strand breaks may result in cell killing, mutation and carcinogenesis.

The fragments from the double-strand breaks can behave as follows:

- (1) The breaks may be rejoin in their original configuration and correctly repaired.
- (2) The breaks may fail to rejoin and give rise to an aberration, which results in a deletion at the next mitosis.
- (3) One broken end may rejoin another broken end to give rise to chromosomes that may result in a lethal damage at the following mitosis.

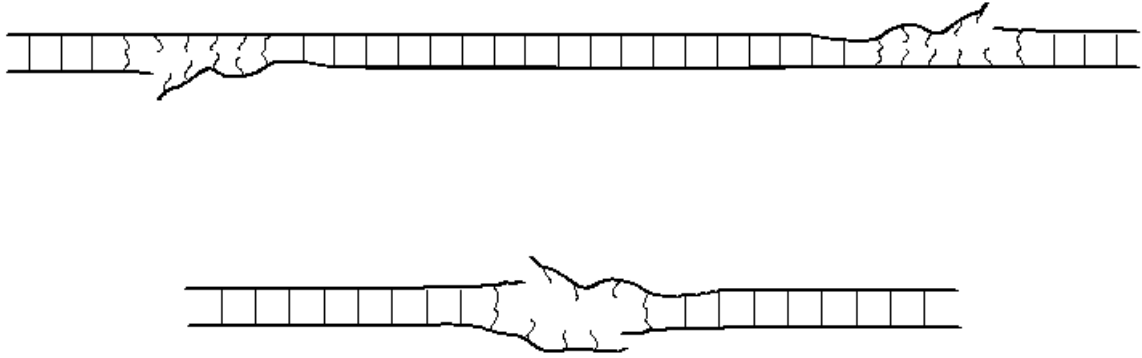


Figure 3.1 An idealized schematic comparing two single strand breaks (top) and one double strand break (bottom). A double strand break is formed when two or more strand breaks are formed in opposite strands of DNA within about 10 to 20 base pairs of each other. The lines between strands of DNA represent hydrogen bonds between complementary base pairs.

C. Apoptotic and mitotic death

Radiation induced apoptotic death will make the cell kill itself. Double-strand breaks occur in the linker regions nucleosomes, to produce DNA fragments that are multiples of approximately 185 base pairs. Radiation induced apoptosis is highly cell-type dependent.

The most common form of cell death from radiation is mitotic death. If the cell loses its proliferative ability, it will die in attempting to divide due to damaged chromosomes. It may die after one or several times of mitosis. Loss of reproductive ability is the critical response to irradiation.

D. Categories of radiation damage

Radiation damage to mammalian cells can be put into three categories:

(1) lethal damage, which is irreparable and leads to cell death;

(2) sublethal damage, which can be repaired in hours under normal circumstances; Sublethal damages can also combine and interact to form a lethal damage, which in turn leads to cell death.

(3) potentially lethal damage, which can be modified by postirradiation environmental conditions.

3.1.2 Models of radiation cell killing

A. Target theory

Model 1: single-target single-hit inactivation

There is only one sensitive target in the cell. Single hit by radiation on the target will lead to death of the cell. Assume hitting the target in a cell is a Poisson random process with respect to dose. In a small interval $D \rightarrow D+dD$, the probability of hitting the target is proportional to dD :

$$P(D, D + dD; \text{hit} = 1) = \frac{dD}{D_0}.$$

Considering only the first order of dD , at dose $D+dD$, the probability of hitting the target once can be expressed as

$$\begin{aligned} &P(0, D + dD; \text{hit} = 1) \\ &= P(0, D; \text{hit} = 1)P(D, D + dD; \text{hit} = 0) + P(0, D; \text{hit} = 0)P(D, D + dD; \text{hit} = 1) \\ &= P(0, D; \text{hit} = 1) \left(1 - \frac{dD}{D_0}\right) + P(0, D; \text{hit} = 0) \frac{dD}{D_0} \end{aligned}$$

Then it can be easily shown that the probability of zero hit at dose D is

$$P(0, D; \text{hit} = 0) = e^{-\frac{D}{D_0}}.$$

The probability of the target being hit n times at dose D is

$$P(0, D; \text{hit} = n) = \frac{\left(\frac{D}{D_0}\right)^n}{n!} e^{-\frac{D}{D_0}}.$$

The survival rate equals the probability of zero hit,

$$S = P(\text{survival}) = e^{-\frac{D}{D_0}}.$$

Model 2: single-target multiple-hit inactivation

There is only one sensitive target in the cell. n hits by radiation on the target will lead to death of the cell. With the same arguments as in Model 1, we can conclude that the survival rate is

$$S = \sum_{k=0}^{n-1} \frac{\left(\frac{D}{D_0}\right)^k}{k!} e^{-\frac{D}{D_0}}.$$

Especially, when $n=2$, we have

$$S = \left(1 + \frac{D}{D_0}\right) e^{-\frac{D}{D_0}}$$

Model 3: Multi-target single-hit inactivation

In this model, one hit on each of the n sensitive targets in a cell will lead to death of the cell. Assume each target is independent of the others. The probability of one target being hit is

$$P(\text{one target inactivated}) = 1 - e^{-\frac{D}{D_0}}.$$

Then the probability that all of the targets are hit is the product of the probabilities of each target being hit,

$$P(\text{death}) = P(\text{each target being hit}) = [P(\text{one target inactivated})]^n = \left(1 - e^{-\frac{D}{D_0}}\right)^n.$$

Thus the survival rate is

$$S = 1 - P(\text{death}) = 1 - \left(1 - e^{-\frac{D}{D_0}}\right)^n.$$

B. The lethal, potential lethal (LPL) damage model

Curtis proposed a lethal and potentially lethal (LPL) model to describe the cell killing effects of ionizing radiation in the 1980's⁵. In the LPL model, double-strand breaks are created at a rate proportional to the absorbed dose rate and then repaired or misrepaired.

There are two types of lesion: repairable (potential lethal) and non-repairable (lethal) lesions. Two types of repair processes are generally considered in the LPL model: repair and binary misrepair. Repair corresponds to the correct rejoining of the break-ends associated with a single double-strand-break (DSB) lesion. In the binary misrepair interaction process, the break-ends associated with two different DSB lesions are incorrectly rejoined to form a lethal (misrepaired) DNA damage. Mathematically, the formation, repair and misrepair of DSB lesions and fatal lesions is described by the following system of differential equations:

$$\frac{dL_{dsb}(t)}{dt} = \dot{D}(t)\eta_{PL} - \varepsilon_{PL}L_{dsb}(t) - \varepsilon_{2PL}L_{dsb}^2(t)$$

$$\frac{dL_f(t)}{dt} = \dot{D}(t)\eta_L + \varepsilon_{2PL}L_{dsb}^2(t)$$

$L_{dsb}(t)$ is the number of double-strand break lesions. $L_f(t)$ is the number of fatal lesions.

$\dot{D}(t)$ is the dose rate. η_{PL} and η_L are the number of potential lethal lesions produce per

unit dose rate and the number of irreparable lethal lesions produced per unit dose rate. ϵ_{PL} is the probability for a double-strand break repaired without a fatal result. ϵ_{2PL} is the probability of binary misrepair, in which two double-strand break ends rejoin and lead to a fatal result. It is the binary misrepair process leads to a quadratic component in cell killing (Figure 3.2).

If a magnetic field is present, we would like to know if η_{PL} and η_L could possibly change.

C. Repair saturation model

In this model, only one type of lesion and single-hit inactivation are postulated. However, dose-dependent repair is proposed. Repair saturation provides an explanation for radiobiological phenomena without the need for existence of “sublethal” damage as in dual radiation action model⁶.

D. The linear-quadratic model

Since the cell survival curves usually have a downward bending, they can be fitted with a quadratic polynomial. Thus we have

$$S = e^{-\alpha D - \beta D^2}.$$

This is just a mathematical fitting. Several other models derive similar expressions as the linear-quadratic model. Different models have their different explanations for this linear-quadratic expression.

Barendson used single-track and double-track effects to explain this model⁷. Kellerer and Rossi developed their Dual Radiation Action model and reached a similar linear-

quadratic expression⁸. Chadwick and Leenhout proposed that the linear and quadratic terms were associated with the probability of producing a DNA double-strand break either by a single particle track or by two independent tracks, respectively⁹. Tobias' repair-misrepair (RMR) model¹⁰ and Curtis' lethal-potential lethal (LPL) model also give very similar results to the linear-quadratic model.

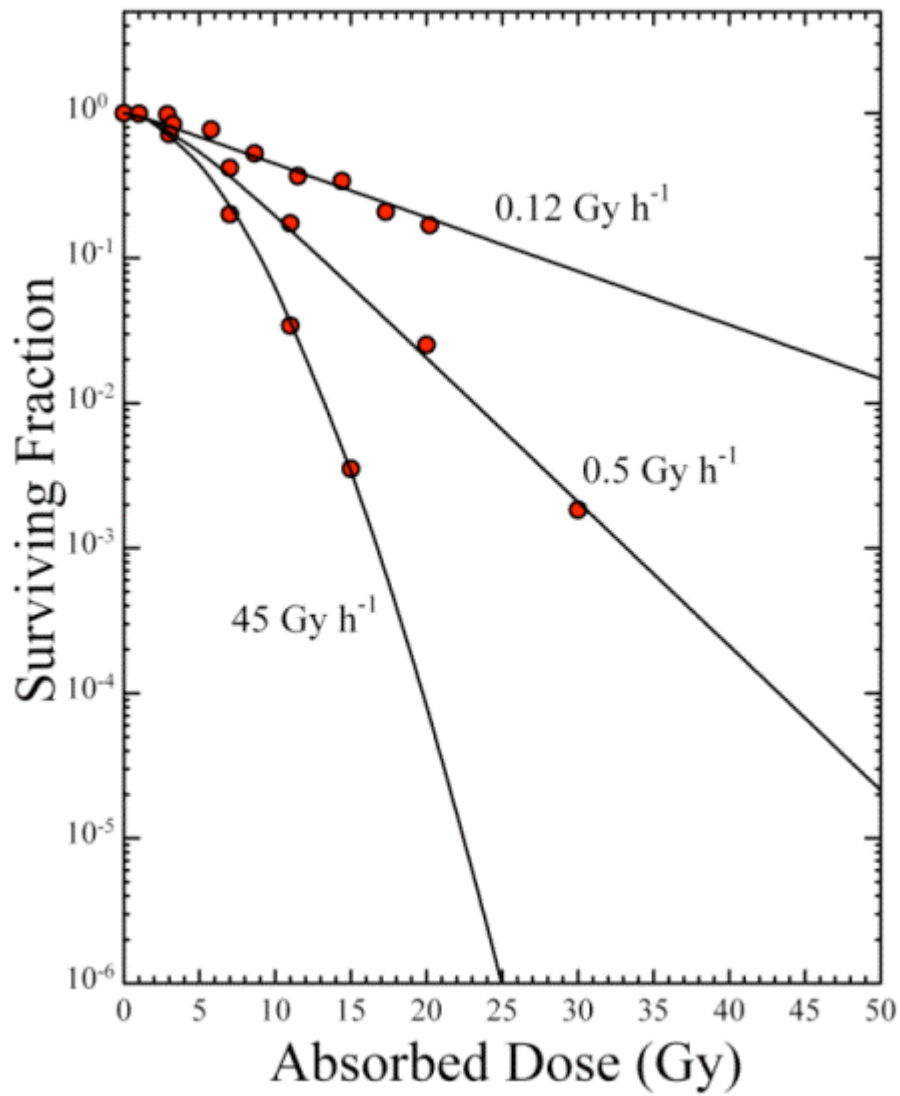


Figure 3.2 Graph showing the LPL-calculated survival response pattern of CHO 10B2 cells irradiated ¹³⁷Cs gamma-rays. Filled circles are the measured survival probabilities. (From M.A. Stackhouse and J.S. Bedford, An ionizing Radiation-Sensitive Mutant of CHO Cells: irs-20 I. Isolation and Initial Characterization. *Radiat. Res.*, **136**(2), 241-249 1993)

3.1.3 Relative biological effectiveness (RBE)

A. The definition of RBE

For a specific biological effect, the relative biological effectiveness of a radiation A, relative to another radiation B, is defined by

$$R = \frac{D_B}{D_A} \quad (3.1)$$

where D_A and D_B are the absorbed doses of the two radiation causing an equal effect. As an example, the biological effect could be 50% killing of the *Saccharomysis cerevisea* cells as in our experiment. Given two radiations, the RBE could be different for different biological effect.

B. Factors that can affect RBE

RBE depends on the following factors:

(1) Biological system

As shown in Figure 3.3, different cell lines may have different RBE for the same radiation.

(2) Biological effect

Killing effect may have different RBE from mutation effect. As shown in Figure 3.3, RBE may be different even for different killing rates.

(3) Radiation quality, including linear energy transfer (LET) and track structure

As an example, Figure 3.3 also shows that the efficiency of cells killing is different for different radiations. Some radiations have significantly different LET and track structure. Radiations with high LET, such as heavy ions, deliver energy more densely

along its track and have a high efficiency of cell killing (Figure 3.4). However, the efficiency decreases if the LET is too high (Figure 3.5). Because RBE is the ratio of doses producing equal biological effect, the more densely ionizing radiation has a lower RBE than the most efficient LET radiation. In other words, it is less effective per unit dose even though it is as effective per track.

In this thesis work, we are particularly interested in the effect of track structure while keeping LET unchanged. The presence of a magnetic field of several Tesla doesn't change the LET of the radiation. It only changes the trajectory of the charged particles, especially the secondary electrons. Our goal is to investigate whether such change would make the radiation more lethal.

(4) Radiation dose

Figure 3.4 also shows the dependence of RBE on dose. The three curves refer to RBE at different dose levels.

(5) Dose rate

The dose-rate effect results from the repair of the sublethal damage that occurs during a long exposure. The RBE reduces as the dose rate decreases and the exposure time is extended (Figure 3.6).

(6) Number of dose fractions

The dose-fraction effect results from the quadratic term in the linear-quadratic model. For the same dose, RBE decreases as the number of dose fractions increases.

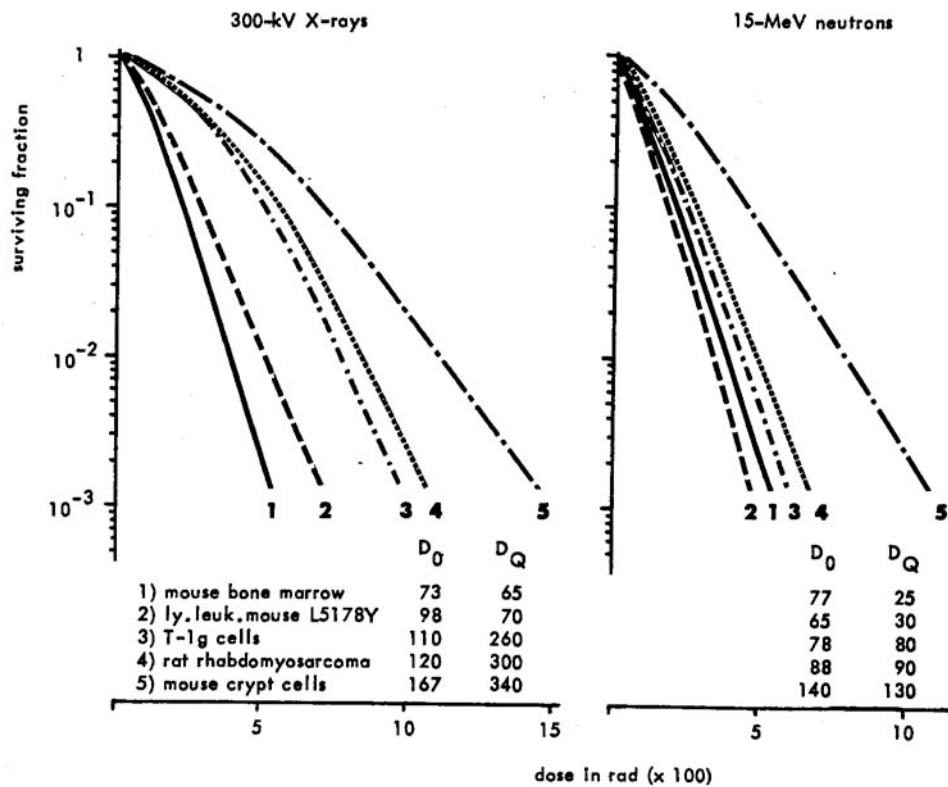


Figure 3.3 Survival curves for various types of clonogenic mammalian cells irradiated with 300-kV x-ray or 15-MeV $d^+ \rightarrow T$ neutrons. Note that the variation in radiosensitivity among different cell lines is markedly less for neutrons than for x-rays. (From Broerse JJ, Barendsen GW, Relative biological effectiveness of fast neutrons for effects on normal tissues. *Curr Top Radiat Res Q* 8, 305-350, 1973)

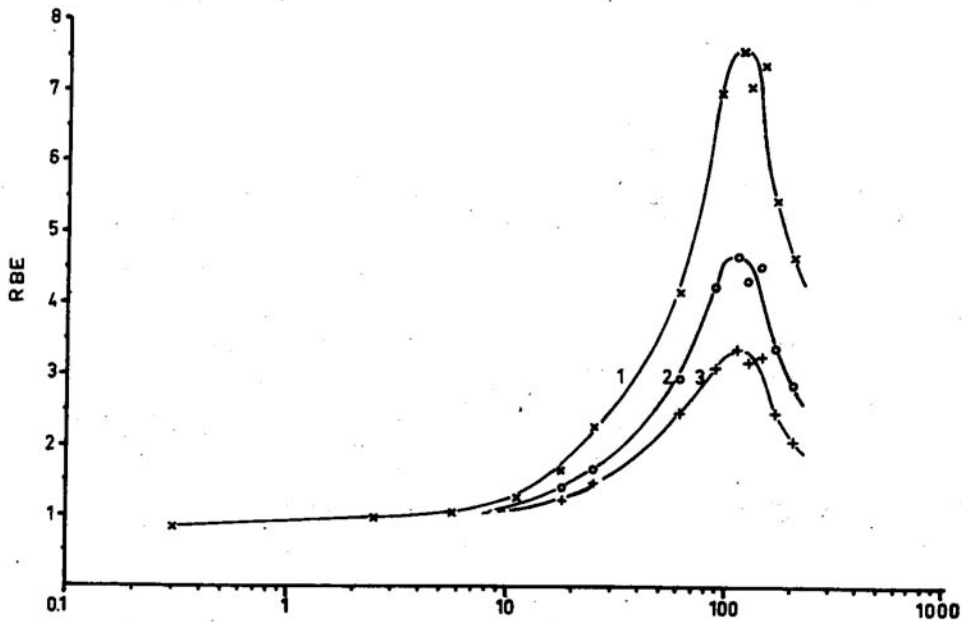


Figure 3.4 Variation of RBE with LET for survival of mammalian cells of human origin. The RBE rises to a maximum at an LET of about 100 keV/ μ m and falls for higher values of LET. Curves 1, 2 and 3 refer to cell-survival levels of 0.8, 0.1 and 0.01, respectively, illustrating that the absolute value of the RBE is not unique but depends on the level of biological damage and, therefore, the dose level. (From Barendson GW, Curr Top Radiat Res Q 4, 293-356, 1968)

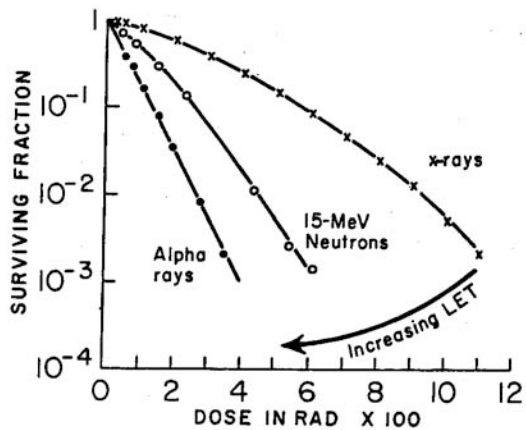


Figure 3.5 Survival curves for cultured cells of human origin exposed to 250-kVp x-rays, 15-MeV neutrons, and 4-MeV α -particles. As the linear energy transfer of radiation increases, the slope of the survival curves gets steeper. (Adapted from Broerse JJ, Barendsen GW, van Kersen GR, Curr Top Radiat Res Q 4, 293-356, 1968)

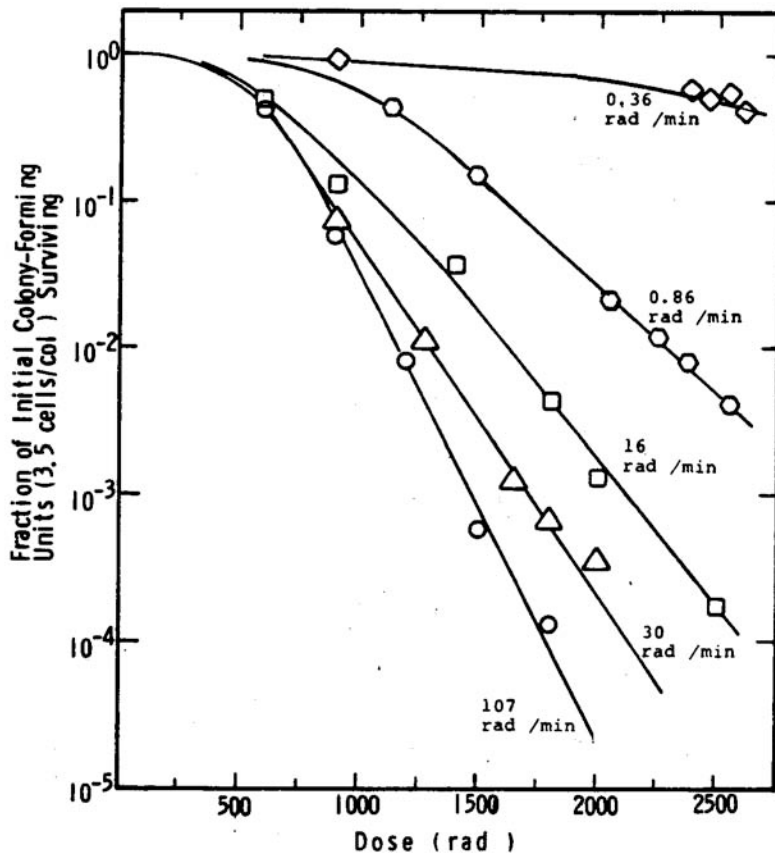


Figure 3.6 Dose-response curves for Chinese hamster cells (CHL-F line) grown *in vitro* and exposed to ^{60}Co γ -ray at various dose rates. At high doses a substantial dose-rate effect is evident even among 1.07, 0.3 and 0.16 Gy/min. The decrease in cell killing becomes even more dramatic as the dose rate is reduced further. (From Bedford JS, Mitchell JB: Dose rate effects in synchronous mammalian cells in culture. Radiation Research 54, 316-327, 1973)

3.1.4 Microdosimetric model of RBE

Based on the discussion in the previous section, we can propose the possible effect of the magnetic field on RBE. The radiobiology models in section 3.1.1 mainly deal with two processes: production of DNA damage and repair of DNA damage. The effect of the magnetic field on damage-repair is reasonably minimal. The effect should manifest itself in the damage-production stage. Since many models actually give similar results as the phenomenological linear-quadratic model, let's use the LQ model as an example.

As shown in Figure 3.7, if the magnetic field is strong enough, the radius of the circular motion can be comparable to or shorter than the CSDA range of the secondary electrons. Thus the possibility of double-strand break from single track, indicated by α in the LQ model, is increased. This model assumes the average interval between two energy deposition events is much longer than the diameter of the DNA double helix but comparable to the circumference of the circular motion. However, the probability to hit the DNA again in close vicinity after a circle is probably very small.

This single-track event can increase the productivity of double-strand break and hence increases RBE of the radiation.

Figure 3.8 illustrates another mechanism. In the presence of the magnetic field, secondary electrons are confined by the magnetic field and their trajectories are more likely to follow the field lines. The electrons travel in a more orderly way. Interactions between tracks may be changed. Therefore, the probability of producing a double-strand break by secondary electrons originated from two independent tracks, indicated by β in the LQ model, may change, which leads to a changed RBE of the radiation.

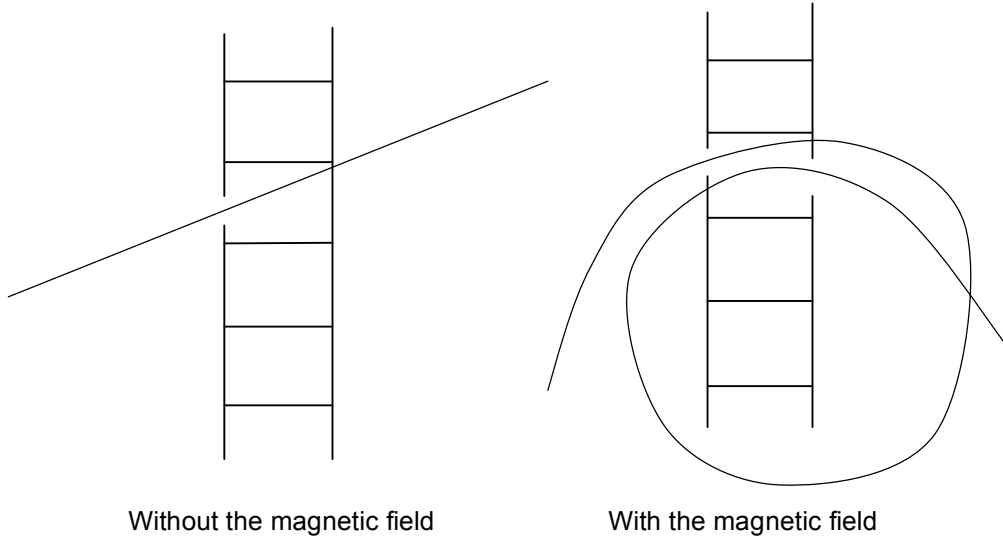


Figure 3.7 The schematic picture showing the effect of the magnetic field on α

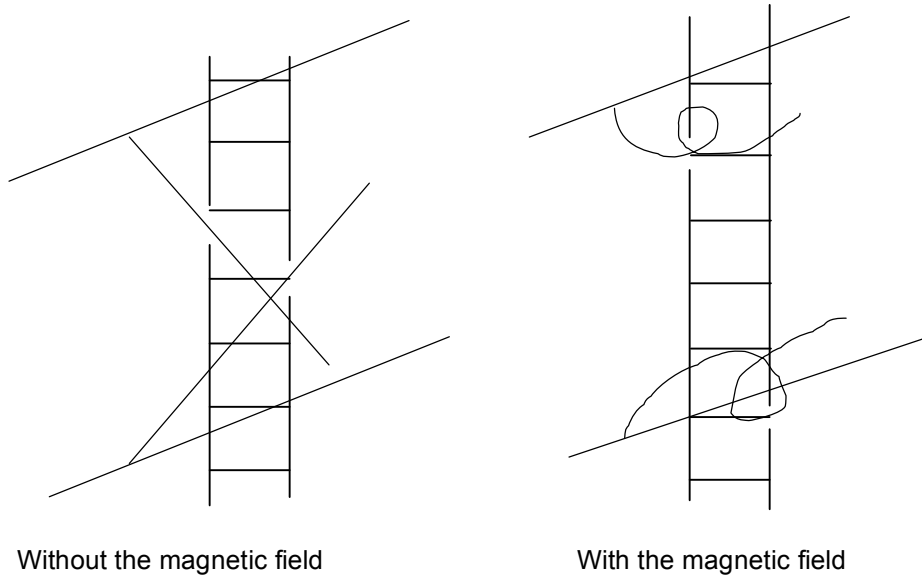


Figure 3.8 The schematic picture showing the effect of the magnetic field on β

3.1.5 Calculation of proximity function of energy deposition from simulated tracks

PENELOPE is the main dose calculation tool. Tracks are generated by this code. The proximity function of energy deposition is obtained from information in these tracks. Comparing the proximity functions of different magnetic fields, we can get information about RBE.

The energy deposition proximity function for a particle with energy E was calculated with the following expression¹¹:

$$t(x; E)dx = \frac{1}{E} \sum_{x < d_{ij} < x+dx} \sum \varepsilon_i \varepsilon_j$$

where ε_i and ε_j are the energies transferred at position i and j respectively, d_{ij} is the distance between i and j .

Figure 3.9-3.13 show the energy deposition proximity functions for B=0 T, 10 T, 100 T, 1000 T and 10000 T. It is clearly that the proximity function cannot be changed significantly for a magnetic field that our current technology allows. It seems to indicate a null effect on RBE in the presence of a magnetic field of the order of several Tesla.

However, there are limitations for this method. PENELOPE can only simulate particles with energy higher than 100 eV. The ionization energy for water is 12.6 eV¹². Between three and four water molecules are ionized for every 100 eV of energy absorbed in the form of ionizing radiation. When the velocity of the electron is perpendicular to a uniform magnetic field, the radius of the circular motion can be expressed by

$$R = \frac{1}{B} \sqrt{\frac{1}{c^2} \left(\frac{K}{e} \right)^2 + 2 \frac{m_0}{c} \left(\frac{K}{e} \right)},$$

where K is the kinetic energy of the electron, B is the magnetic field flux density, m_0 is the rest mass of an electron, c is the speed of light and e is the charge of an electron. Then the radius is $3.6 \mu\text{m}$ for a 10 eV electron in 3T magnetic field. For a cut-off energy as high as 100 eV , the radius is $11 \mu\text{m}$ for a 3 T uniform field. This value is much larger than the cross-section dimension of a DNA double strand. The diameter of the DNA double helix is only 2 nm . The mean range of 10 eV electrons in water is about 10 nm ¹³. This is much smaller than the radius of the circular motion in a magnetic field of the order of 1 T . It suggests null effect from these considerations.

The wavelength of an electron with kinetic energy K is

$$\lambda = \frac{hc}{\sqrt{K^2 + 2m_0c^2K}}$$

where h is Planck constant and m_0 is the rest mass of an electron.

The wave length of a 10 eV electron is 0.39 nm , which is only $1/10000$ of the radius of the circular motion in a 3 T magnetic field. The classical trajectory is still valid in this energy range.

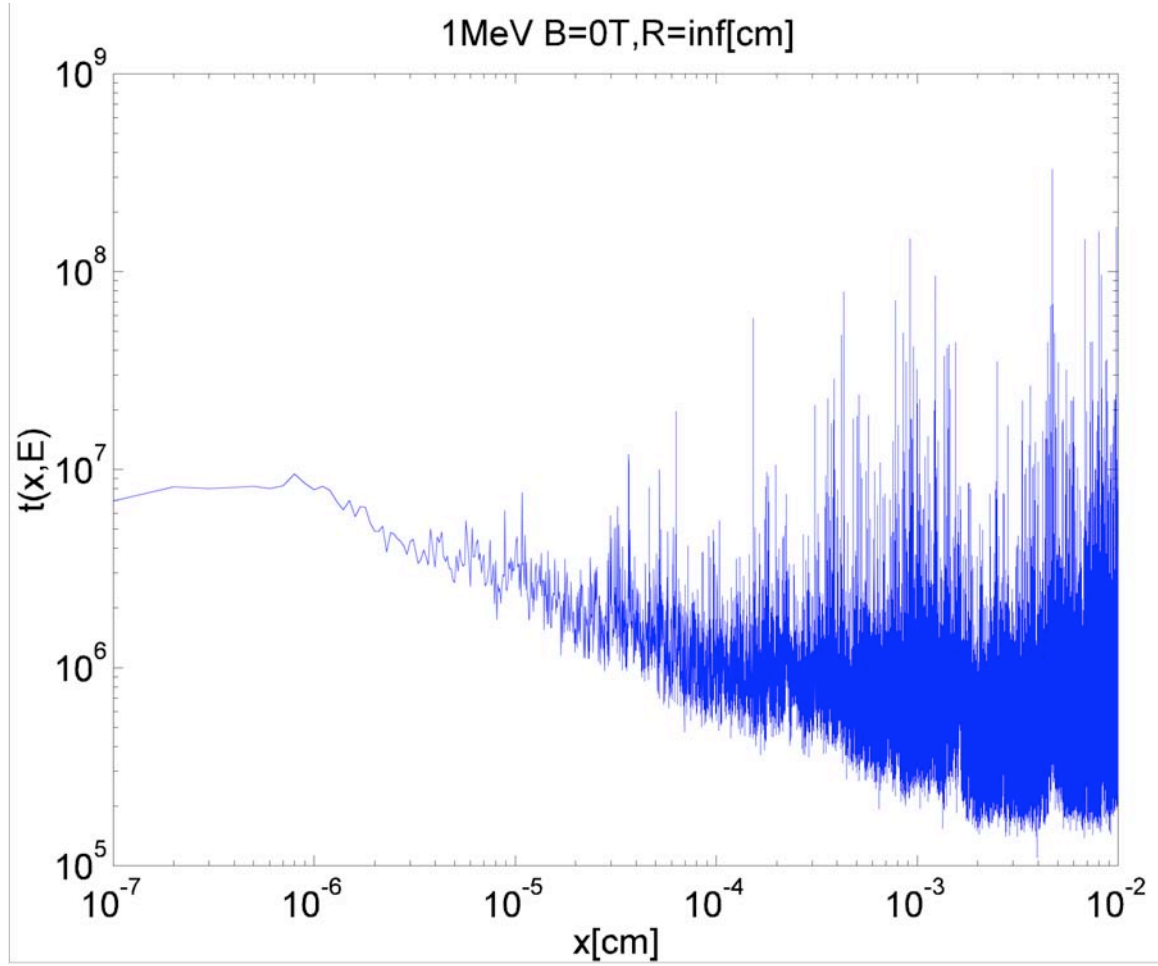


Figure 3.9 Energy deposition proximity function for $B=0$ T

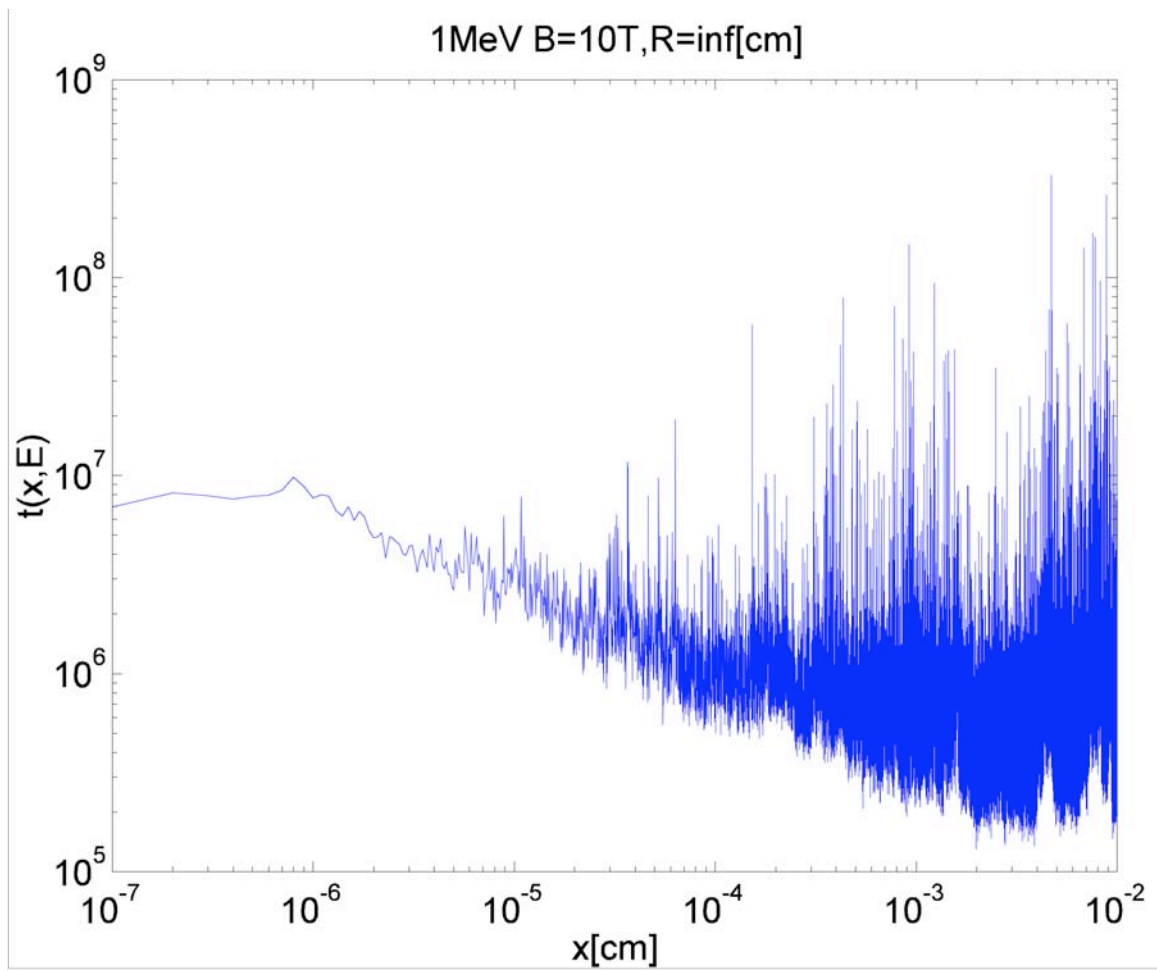


Figure 3.10 Energy deposition proximity function for $B=10$ T

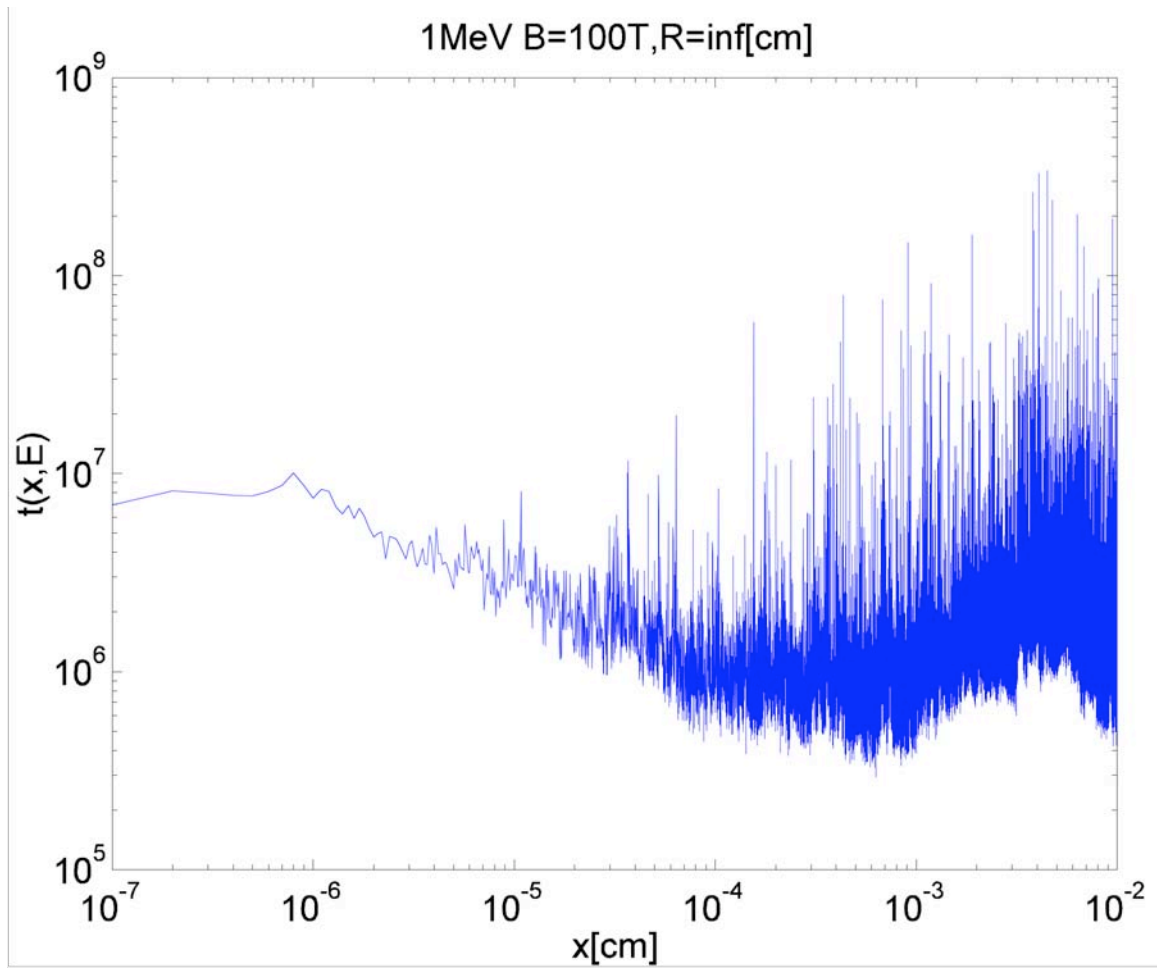


Figure 3.11 Energy deposition proximity function for $B=100$ T

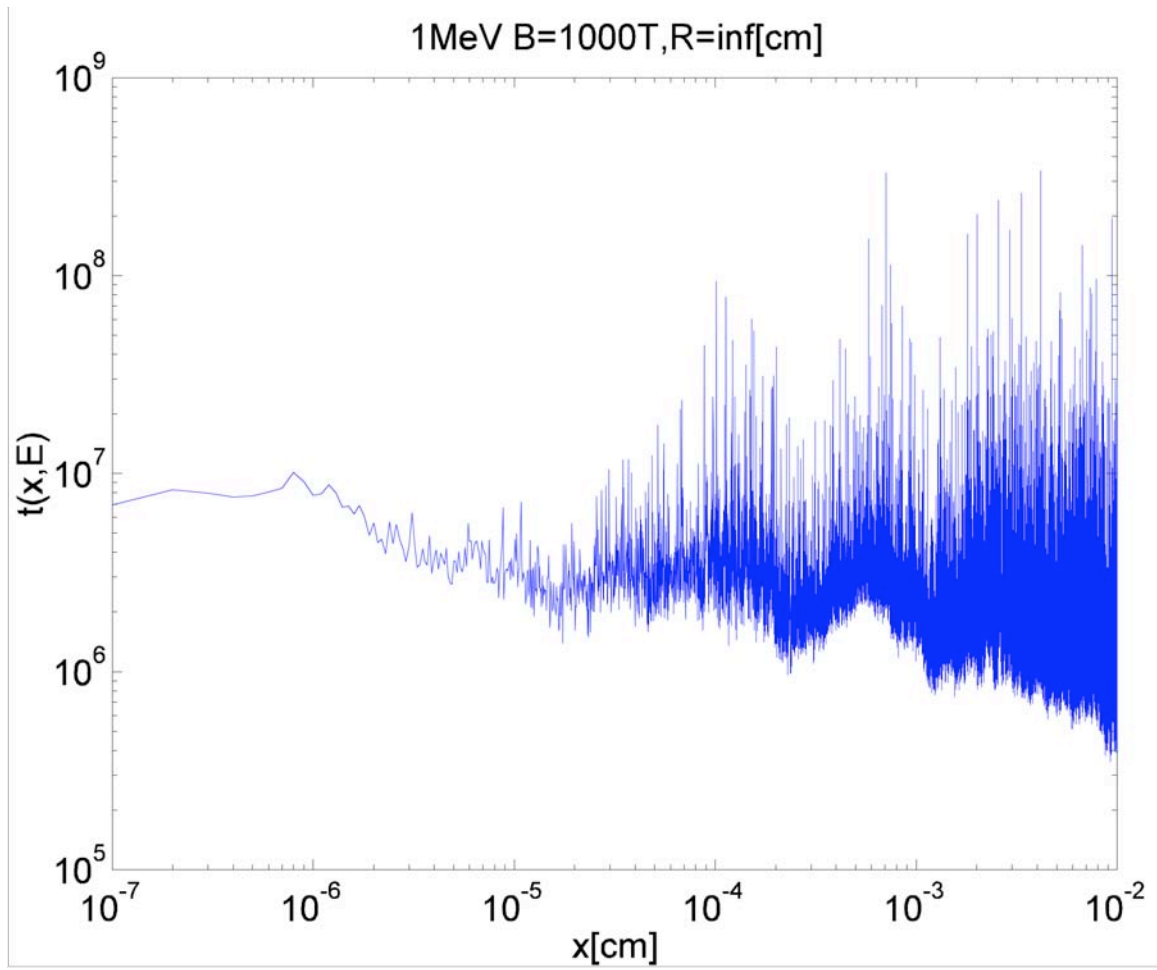


Figure 3.12 Energy deposition proximity function for $B=1000$ T

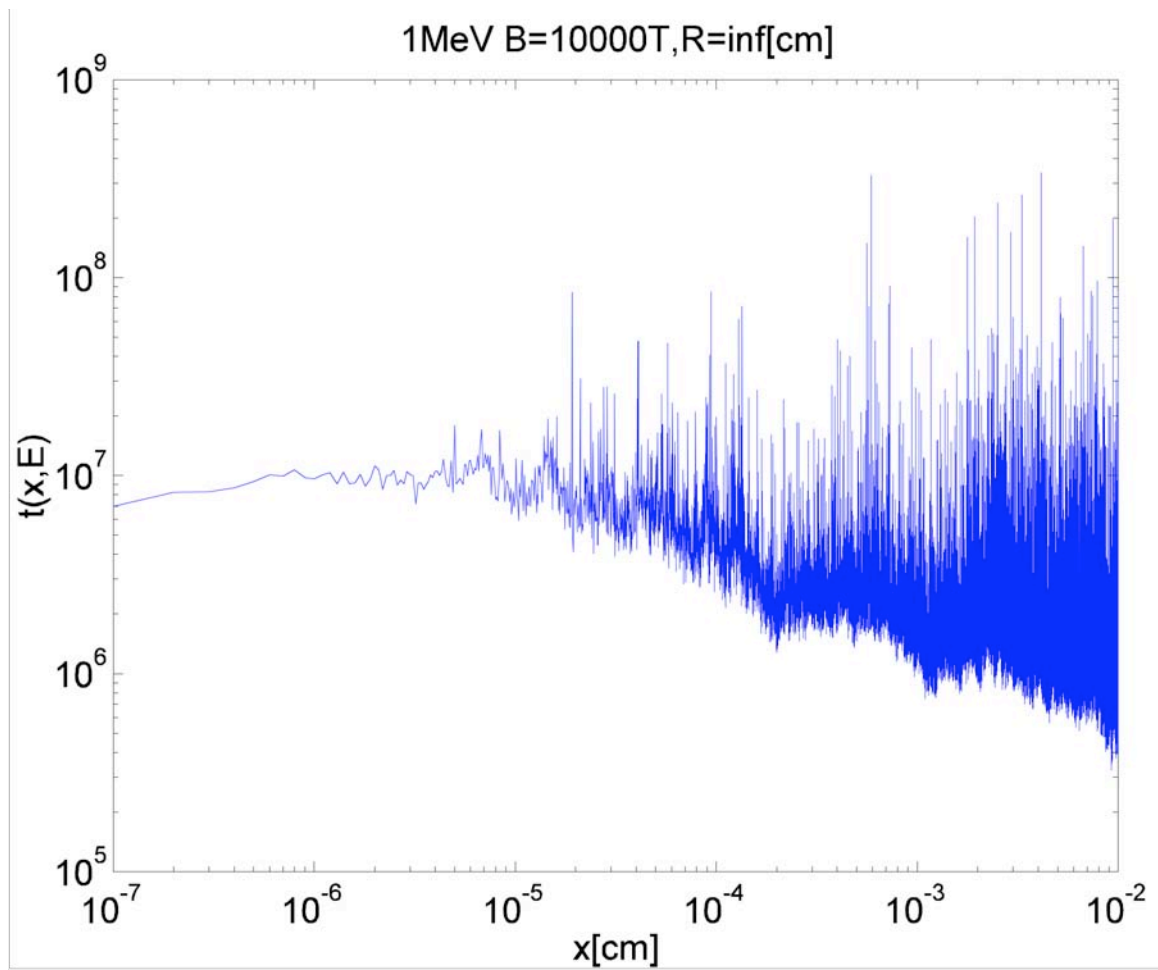


Figure 3.13 Energy deposition proximity function for $B=10000$ T

3.2 The experiment

3.2.1 Purpose of the experiment

Existing literature^{14,15} stated null effect of the magnetic field on RBE for a specific cell line, but the data had limited statistics. We want to find out if there is any evidence indicating a positive effect of the magnetic field on RBE and if so, what future work is needed to clarify this.

Nath, Schulz and Bongiorni studied the response of the Chinese-hamster lung cells irradiated with 30 MV X-ray in the presence of a uniform 2.0 T transverse magnetic field¹⁵. They concluded that no effect was detected with an experimental uncertainty in the range of 20%. Their experimental setup is shown in Figure 3.14. By fitting the experimental data with the survival rate equation

$$S = 1 - \left(1 - \exp\left(-\frac{D}{D_0}\right) \right)^n,$$

they got the results shown in Table 3.1. D_0 is the mean lethal dose and n is the mean number of hits to inactivate the cell.

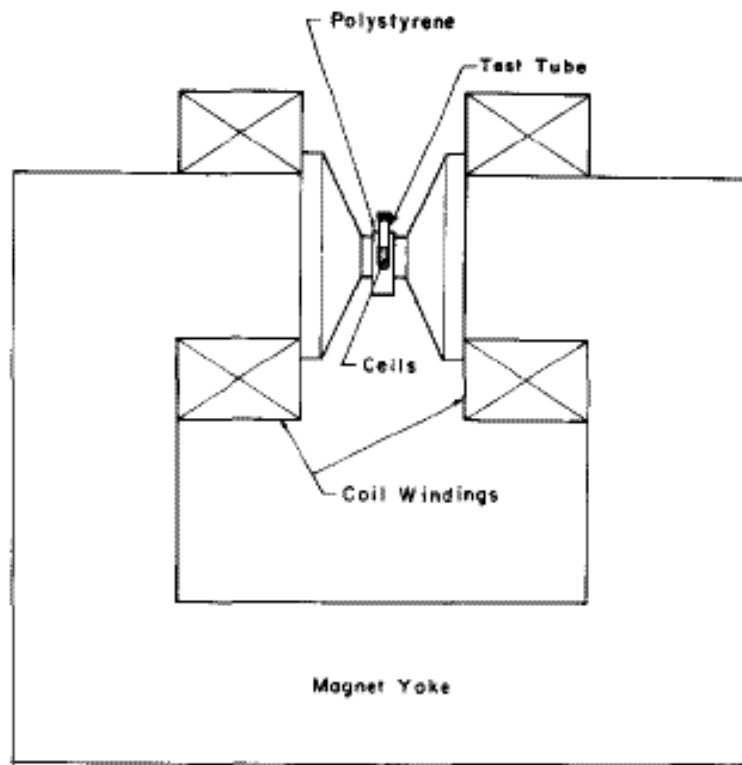


Figure 3.14 Front view of the electromagnet¹⁵

Experiment	D_0 Magnet		n Magnet	
	Off	On	Off	On
1	193	196	3.9	3.1
2	191	159	0.6	1.3
3	249	217	1.2	2.0
4	132	171	3.5	1.8
5	201	214	1.5	1.4
6	146	147	5.5	3.7
7	168	170	3.2	3.3
Meant†	183 ± 39	182 ± 27	2.8 ± 1.1	2.4 ± 1.0
8‡	143	151	5.4	4.7

Table 3.1 Experiments 1-7 were done in a uniform 2.05 T field for aerated cells.

3.2.2 Consideration about cells, radiation sources and magnetic fields

A. What is the appropriate cell line to be chosen for our experiment?

It must be easily obtained. It should not be easily contaminated. It should not be very sensitive to the surrounding environment during transport. It should be suitable for the parameters of the radiation source. It would be better if it is closely related to cancer treatment.

We considered colon cancer cells, fibroblast cells and yeast cells. We worked with another group who were investigating the radiation properties of the proton beams induced by high intensity laser pulses. They used colon cancer cells as the irradiation samples. The biggest problem they met was contamination during transport. The controls died easily. Fibroblast cells need to be incubated at 37°C. They also have requirements on humidity and concentration of CO₂.

Yeast cultures may survive periods of neglect and appear alive when subcultured, and they have consequently gained a reputation for robustness. The yeast *Saccharomyces cerevisiae* is now recognized as a model system representing a simple eukaryote whose genome can be easily manipulated. Normal laboratory haploid strains have a doubling time of 90 min in YPD medium during the exponential phase of growth. They can be easily obtained from biological stores and stored at 4° C for weeks. They can be cultured in normal room conditions and would not be easily contaminated during transport. The YPD medium is agar and does not have the disadvantages for liquid media. Therefore, the yeast *S. cerevisiae* is most suitable to our experiments.

B. What is the appropriate radiation source to be used in our experiment?

Its dose should be obtained precisely. Its dose should not be significantly affected by the magnetic field. It is preferred that charged particle equilibrium be obtained for the irradiated cells. Its strength should be appropriate to do significant damage to the cells chosen. Its environment should accommodate other experimental devices.

We have considered gamma sources, an electron linac, alpha sources, and a tandem Van de Graaff accelerator. Gamma radiation is not affected by a magnetic field. Thus they are ideal to achieve the same fluence with and without the magnetic field. The disadvantage is that the dose rate is low due to its low LET. A high activity gamma source is needed to deliver the appropriate dose in a reasonable amount of time. There are two gamma sources accessible to us at the University of Michigan. One is the 24530 Ci (9/1/1996) ^{60}Co source at the Phoenix Lab. The other is a 28 mCi ^{137}Cs source in Physics Department, which is too weak to deliver enough dose to do substantial damage to yeast cells.

We also can access a 1 mCi ^{244}Cm alpha source. Since the LET of alpha particles is much higher, the distance between the source and the cells must be controlled accurately to a sub-millimeter level. Likewise in air the distance from the source to the cells must be within a few centimeters. With the apparatus that are accessible to us, it is difficult to position the cells this accurately.

Electron linacs or microtrons can deliver electron beams with accurate energies and currents. The disadvantage is that the primary beam fluence will be changed by a magnetic field of the order of 1 T. Thus it becomes difficult to deliver the same amount of dose to the cells with and without the magnetic field.

We can also access the heavy ion tandem Van de Graaff accelerator at the University of Notre Dame. The facility has two 6 T solenoid superconducting magnets. These are the strongest magnets we can possibly use for our experiments. However, the gamma radiation produced by certain nuclear reactions is mixed with neutrons. It is difficult to obtain a pure radiation source from this accelerator.

Finally based on all factors, we chose the ^{60}Co source in Phoenix Lab for our experiment. The ^{60}Co rods are shown in Figure 3.15. Figures 3.16 and 3.17 show the well and the water pool for the source.

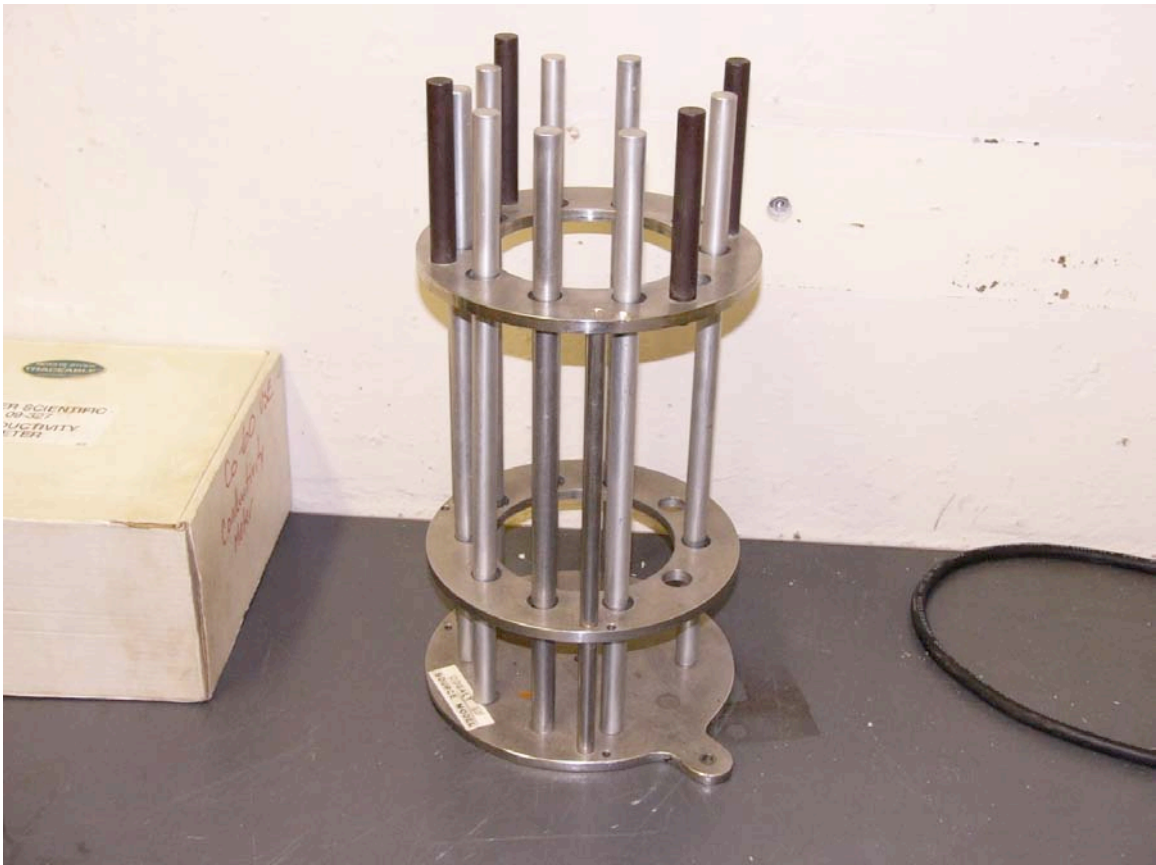


Figure 3.15 The rods of the ^{60}Co gamma source



Figure 3.16 The cover and the lid on the well of the gamma source



Figure 3.17 The source at the bottom of the water pool.

C. What are the available magnets that best suited for our experiment?

We have a 3 T superconducting magnet. It is a solenoid with a 20 cm bore (Figure 3.18). Although it is possible to put the samples inside the bore, there are some problems with regard to the source. If the ^{60}Co source was used with this magnet, it is impractical to put such a large magnet in the irradiation room with the source. The room is only about 3 m by 3 m. The door to this room is only 2 m by 0.75 m and there is a narrow hallway from the door to the room. The lid of the well to the water pool for the source and the cover of the source are made of iron. Therefore it is very difficult to fix the magnet to a stable platform. The advantage of the solenoid magnet is that it can provide a longitudinal magnetic field for the irradiation.

As an alternative one can buy permanent magnets with fixed strength 0.4~1 T. The permanent magnet is made of neodymium iron boron compound. Its general composition is $\text{Nd}_2\text{Fe}_{14}\text{B}$, often-abbreviated NdFeB. NdFeB magnets are not expensive and at room temperature, their magnetic flux density can be as high as 1.3 T near the surface of the magnet. In our application, due to the cell container and the requirement of charged particle equilibrium (CPE), we cannot put the cells very close to the magnet surface. Thus the highest field we can achieve is about 0.78 T. These permanent magnets are small and light compared to superconducting magnets. They don't need any power supply or cooling and are safe to be used in any circumstances. They are very suitable to be used in the small irradiation room of the ^{60}Co source in Phoenix Lab. Nevertheless, they have two disadvantages. First, they are weak compared to a superconducting magnet. Second, they can only provide transverse magnetic fields.

After these considerations, we chose the NdFeB permanent magnets for our experiments.

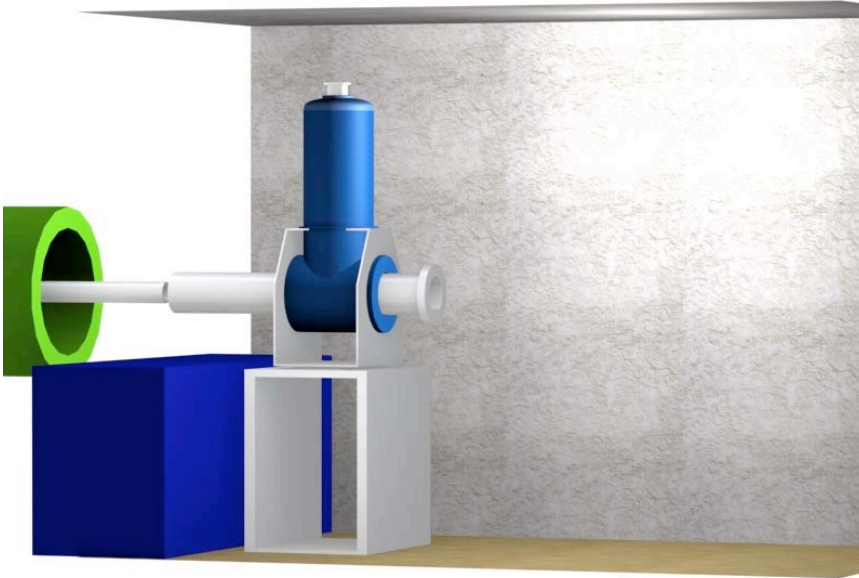


Figure 3.18 Schematic picture of the superconducting magnet

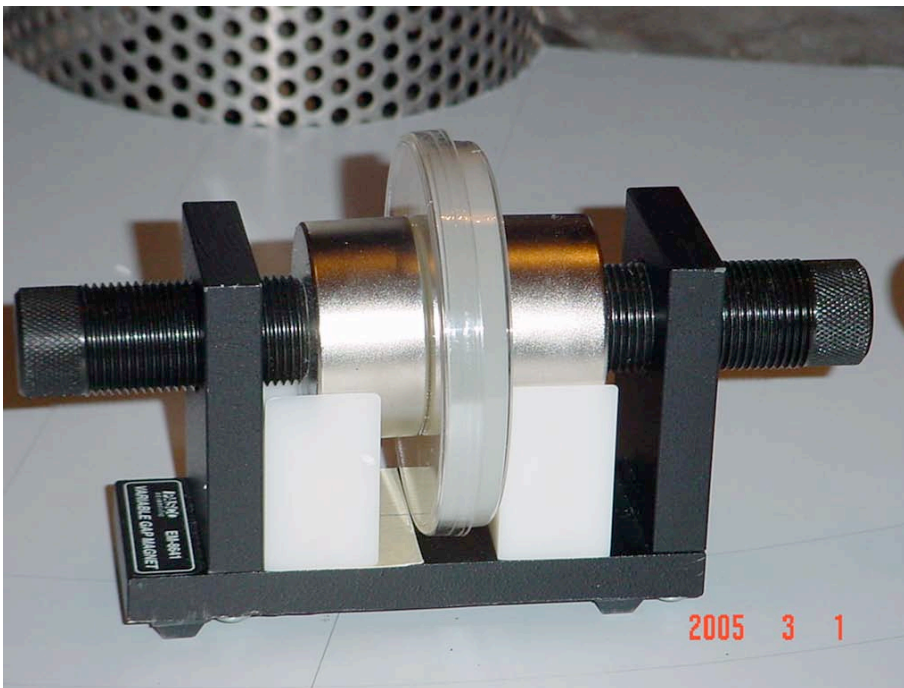


Figure 3.19 Picture of the permanent magnet

3.2.3 Experimental setup

The diameter of the cover of the source is 18.0 cm. A polycarbonate plastic board is placed on top of the steel well as a platform for the magnets, “fake” magnets ($B=0$ but with the same material) and the samples. Half circles with constant radius are marked on the board. We chose $r=39$ cm as the radial location for the samples. At this distance, the gradient of the primary photon fluence is small enough to maintain a relatively uniform radiation field. At the same time, the irradiation time needed for 50% killing rate can be achieved in about 33 minutes. This time interval is appropriate to irradiate four groups of samples and to guarantee the whole experiment be finished in one day. The experimental apparatus and setup are shown in Figures 3.20 and 3.21. The detailed dimensions are shown in Figures 3.22 and 3.23.

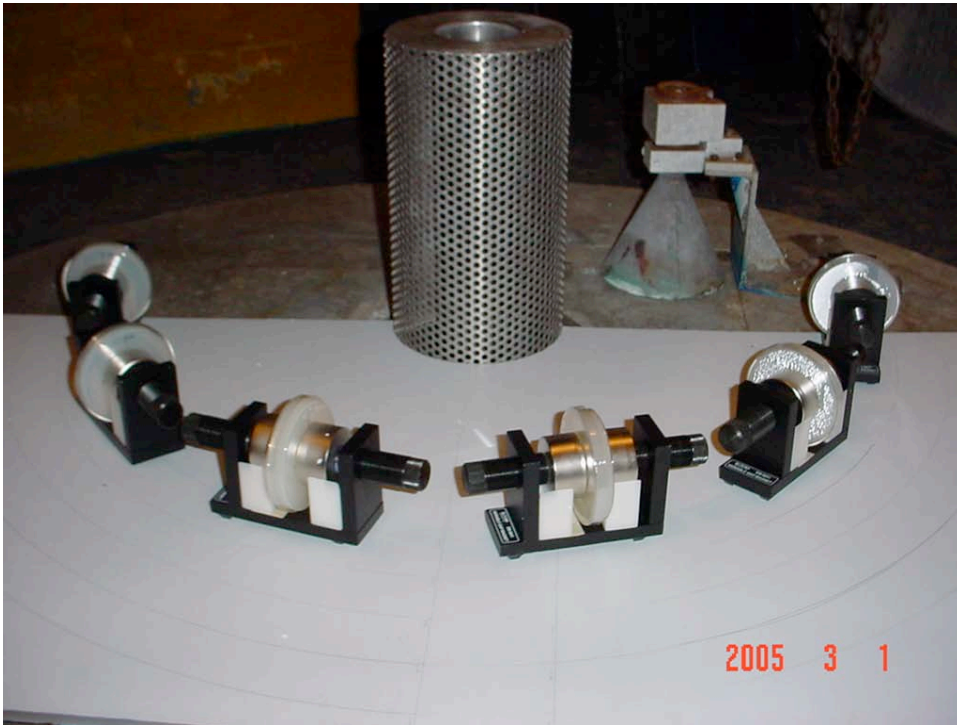


Figure 3.20 Experimental setup

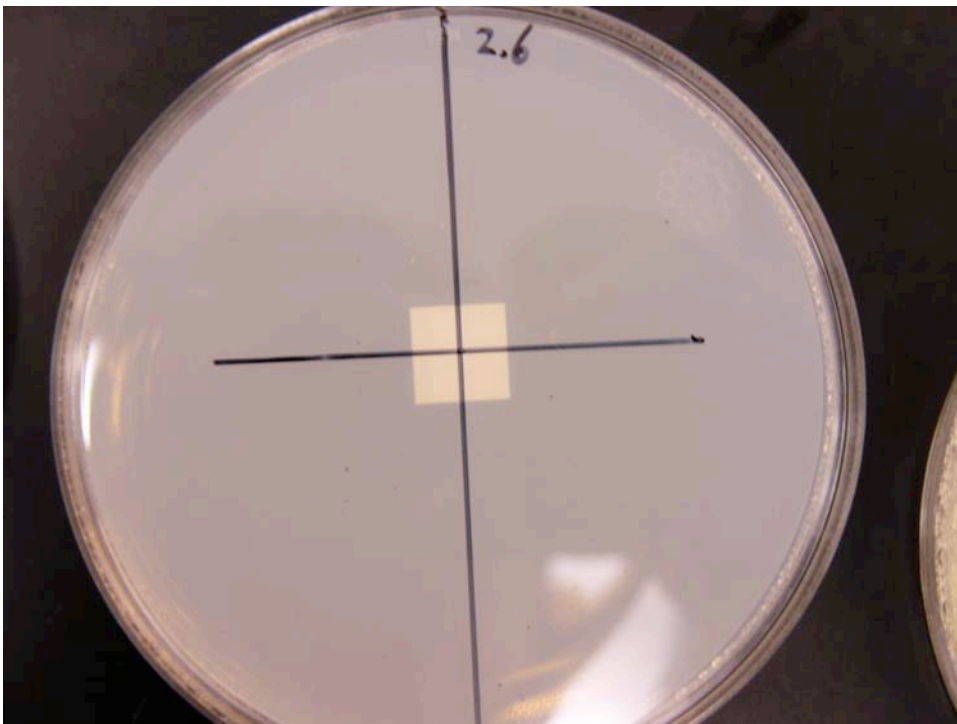


Figure 3.21 Geometry of the membrane and a non-nutrient agar plate

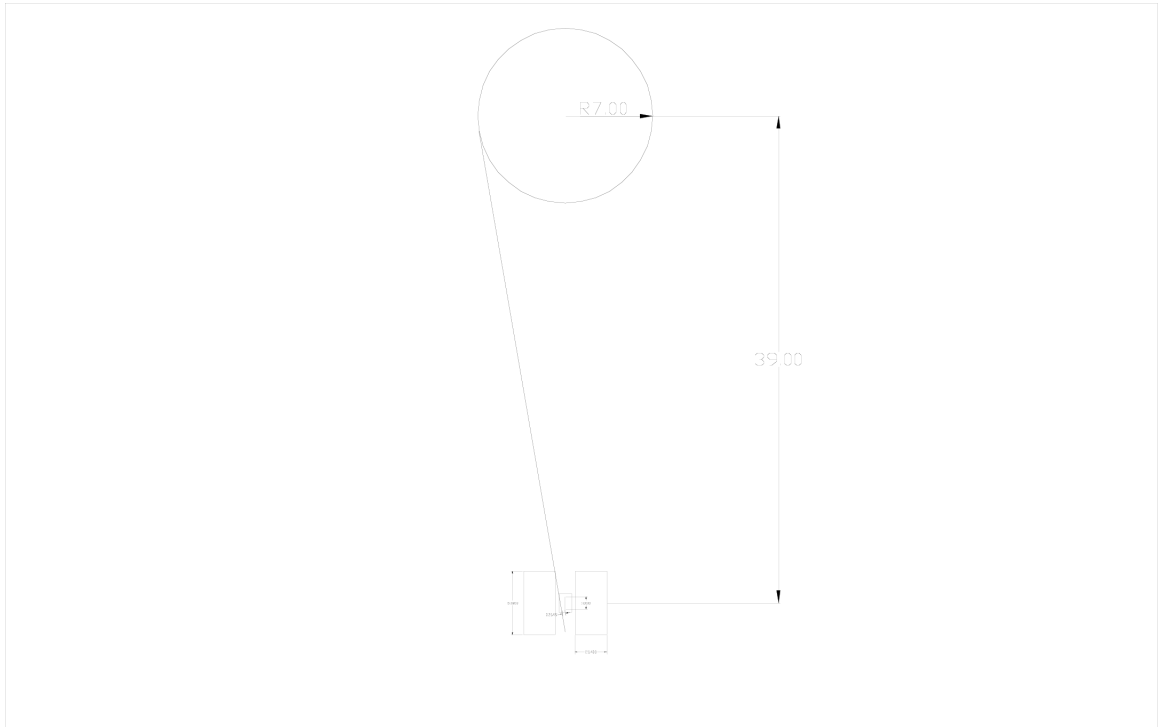


Figure 3.22 Top view of the set up. The circle is the source and the blocks are the magnets.

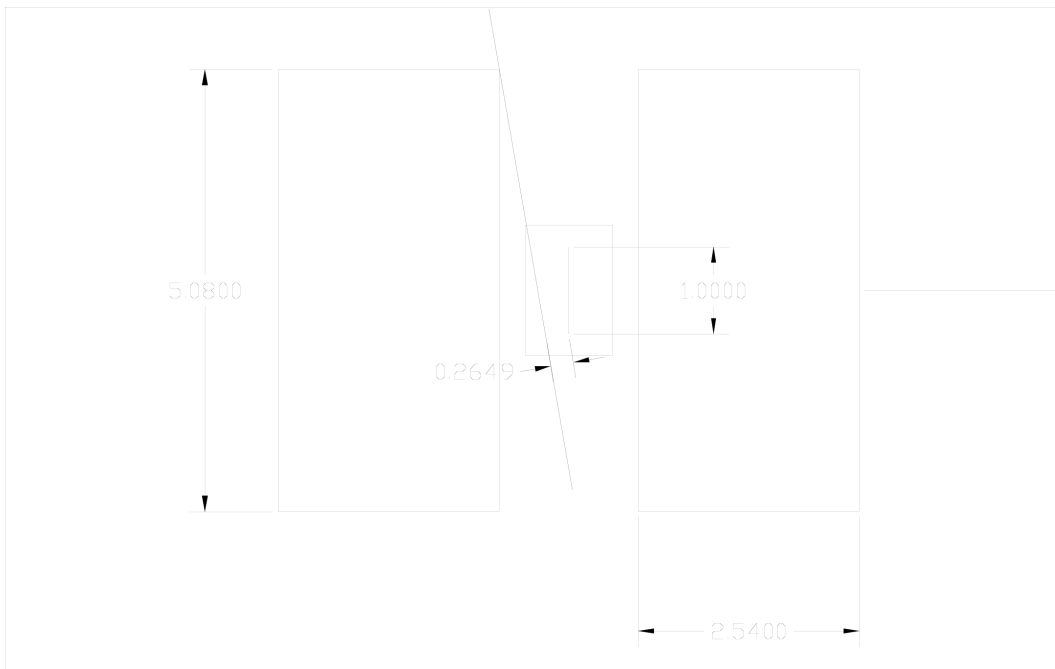


Figure 3.23 Detailed view of the magnets and the nitrocellulose membrane. The membrane is located at the center between the two magnets.

3.2.4 Dose calculation

A. The radiation field

The length of each rod of the nine rods containing ^{60}Co is $L = 13$ inch (Figure 3.15). The diameter of the rod is 0.5 inch. The centers of the rods are located at 2.5 inch from the well center. We assume that each rod can be treated as a line since its diameter is much smaller than its length and the radial distance that we put the samples. Let A be the total activity of the rod. Then the primary fluence for one rod is

$$\Phi = \frac{A}{L} \frac{1}{4\pi r} \left[\tan^{-1} \left(\frac{L}{2r} - \frac{z}{r} \right) - \tan^{-1} \left(\frac{-L}{2r} - \frac{z}{r} \right) \right].$$

The source consists of nine rods with the same dimension. The total fluence of the source is

$$\begin{aligned} \Phi &= \sum_{i=1}^9 \Phi_i (A_i, |\vec{r} - \vec{R}_i|, z) \\ &= \sum_{i=1}^9 \frac{A_i}{4\pi L |\vec{r} - \vec{R}_i|} \left[\tan^{-1} \left(\frac{L}{2|\vec{r} - \vec{R}_i|} - \frac{z}{|\vec{r} - \vec{R}_i|} \right) - \tan^{-1} \left(\frac{-L}{2|\vec{r} - \vec{R}_i|} - \frac{z}{|\vec{r} - \vec{R}_i|} \right) \right] \end{aligned}$$

where z is the axial position of the sample and \vec{r} is the position of the sample in the $z=0$ plane. Samples were located at about $z=-10$ cm. The center of the rod is at $z=0$.

The iso-fluence lines are plotted in Figure 3.24. The variation of the primary photon fluence along a circle at $r=39$ cm is plotted in Figure 3.25. We can also determine the change in fluence along the radius from Figure 3.26.

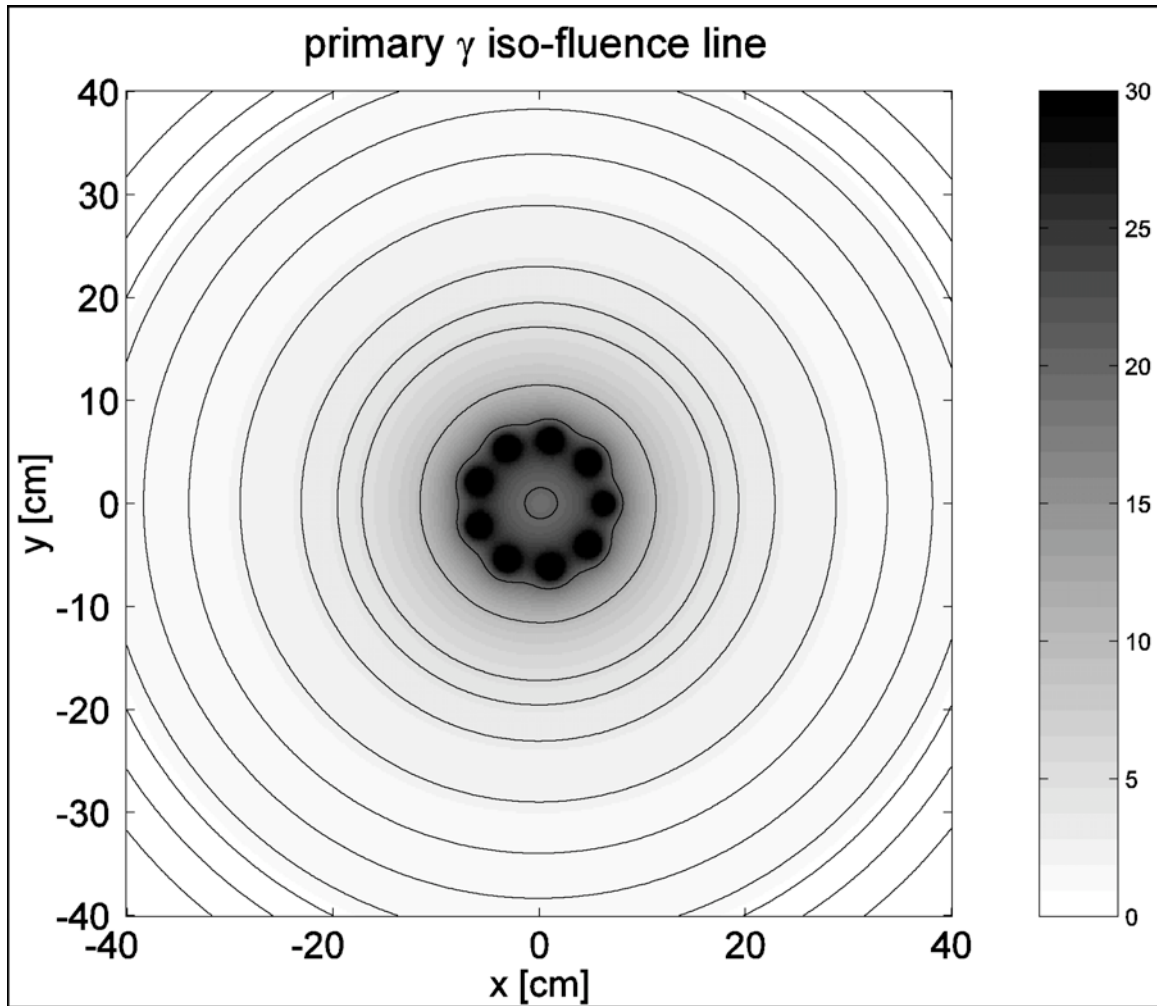


Figure 3.24 The iso-fluence lines of the primary photons of the ^{60}Co source

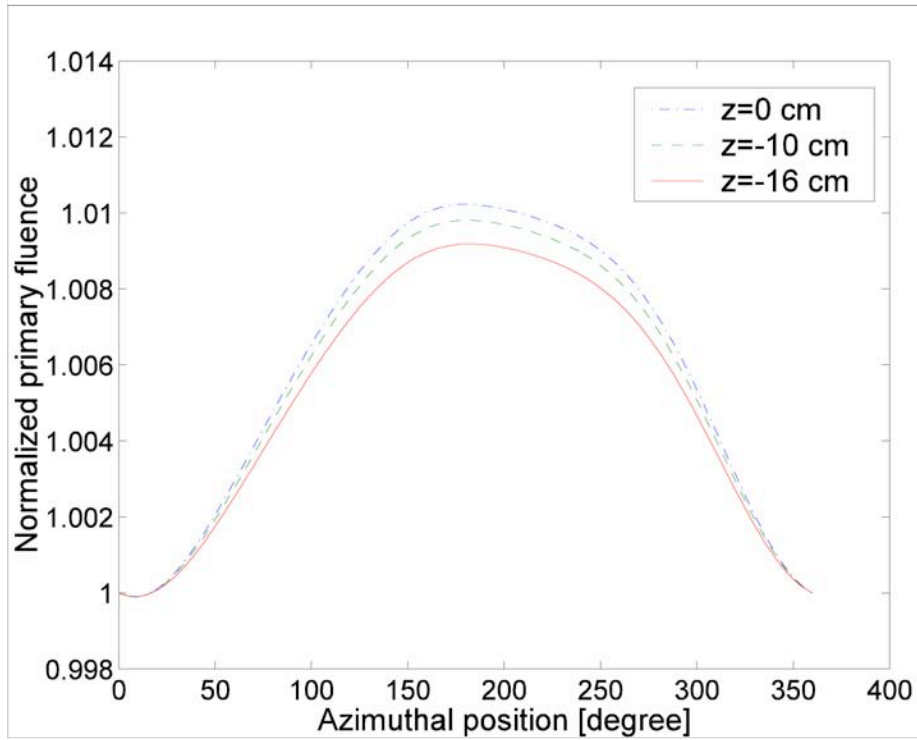


Figure 3.25 This plot shows the uniformity of the primary photon fluence at radial position where the samples are irradiated.

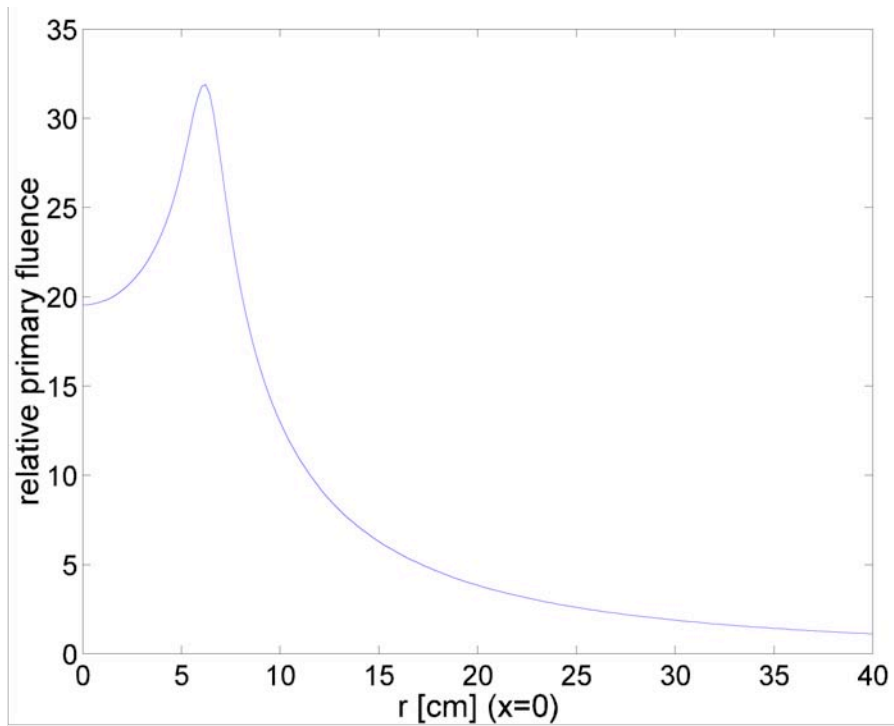


Figure 3.26 The primary fluence as a function of its radial position

B. The magnetic field

The magnetic field was calculated with FEMLAB.

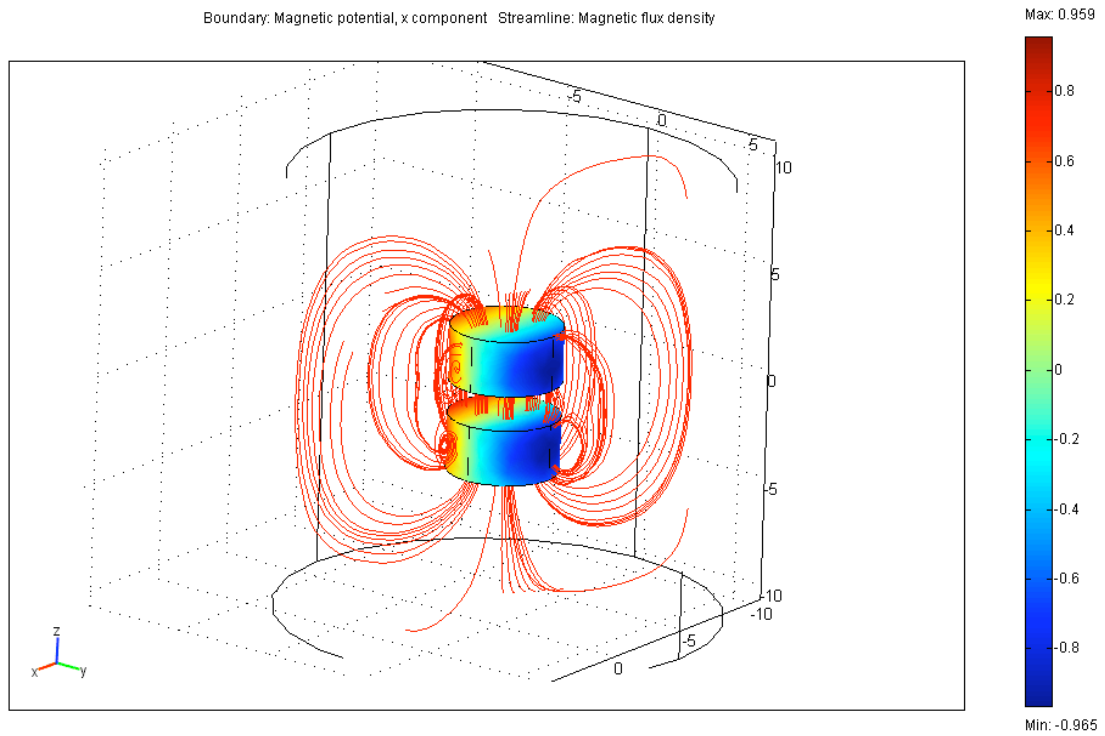


Figure 3.27 Three-dimensional plot of the magnetic field of a pair of permanent magnets of 2 inch diameter

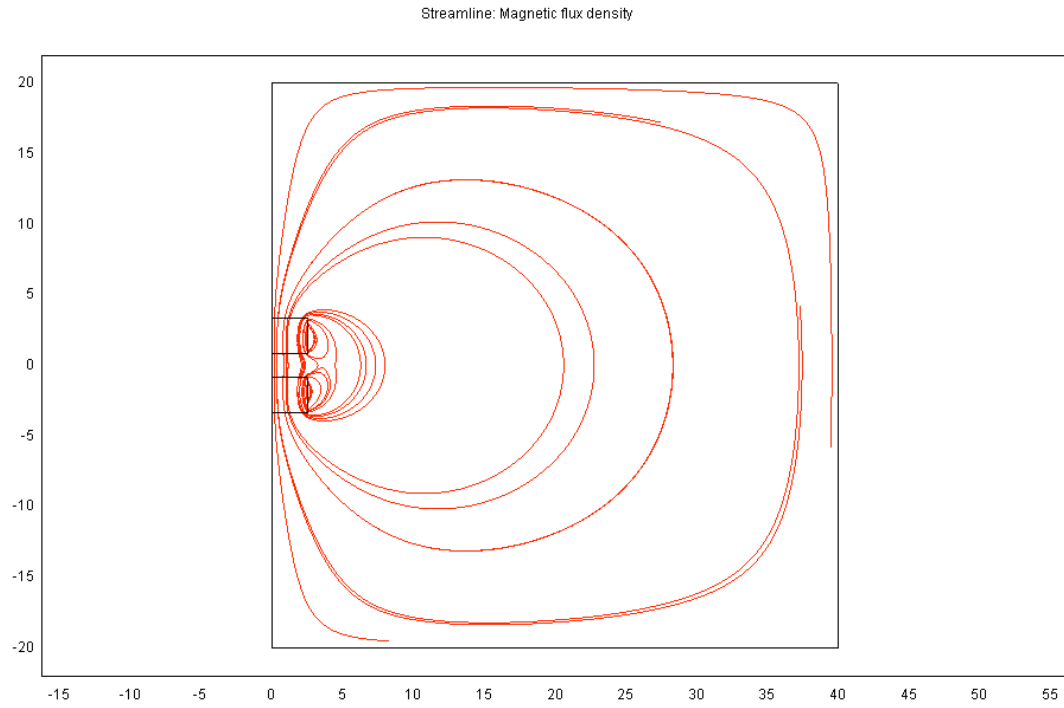


Figure 3.28 The magnetic field in the cross section area of the 2 inch diameter magnets

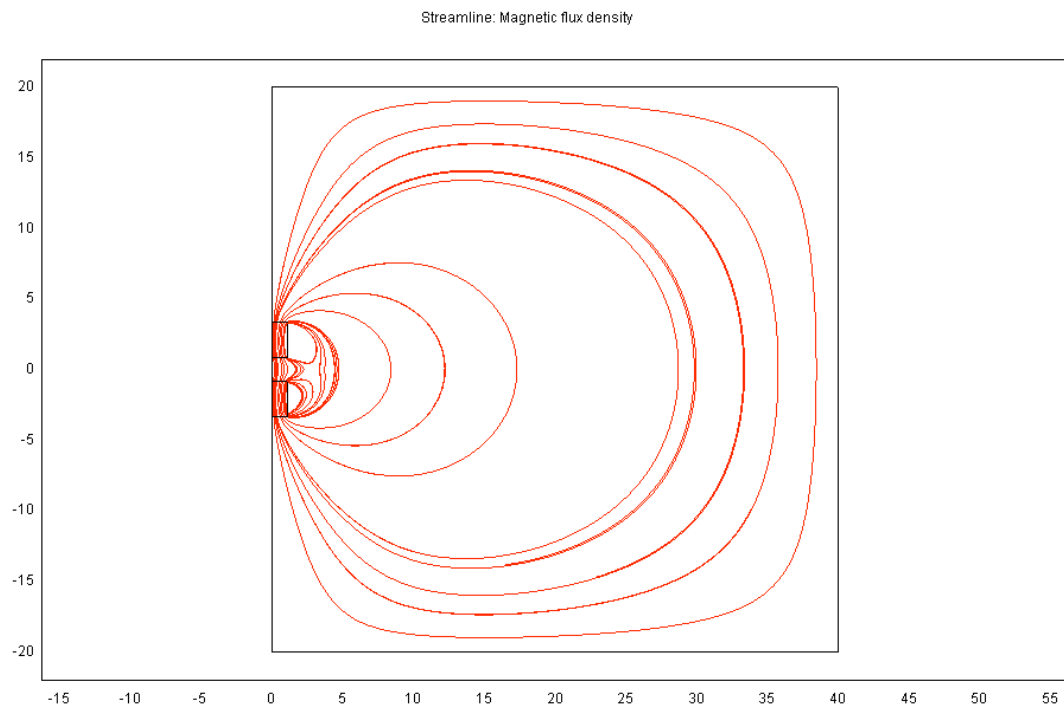


Figure 3.29 The magnetic field in the cross section area of the 7/8 inch diameter magnets

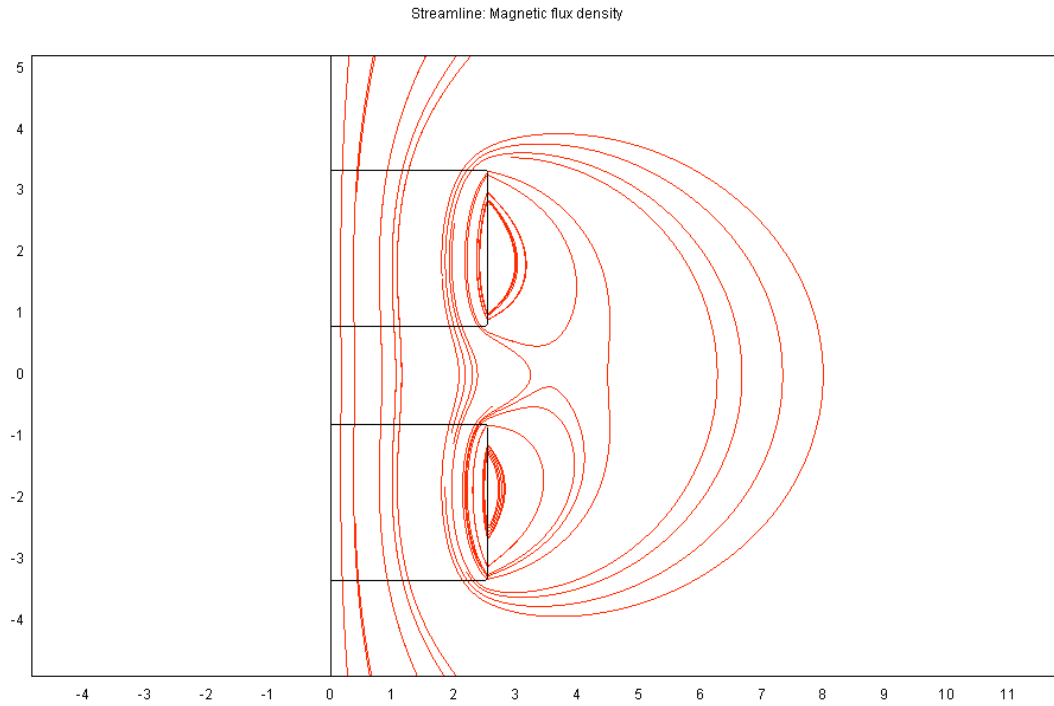


Figure 3.30 Detailed view of the magnetic field in the cross section area of the 2 inch diameter magnets

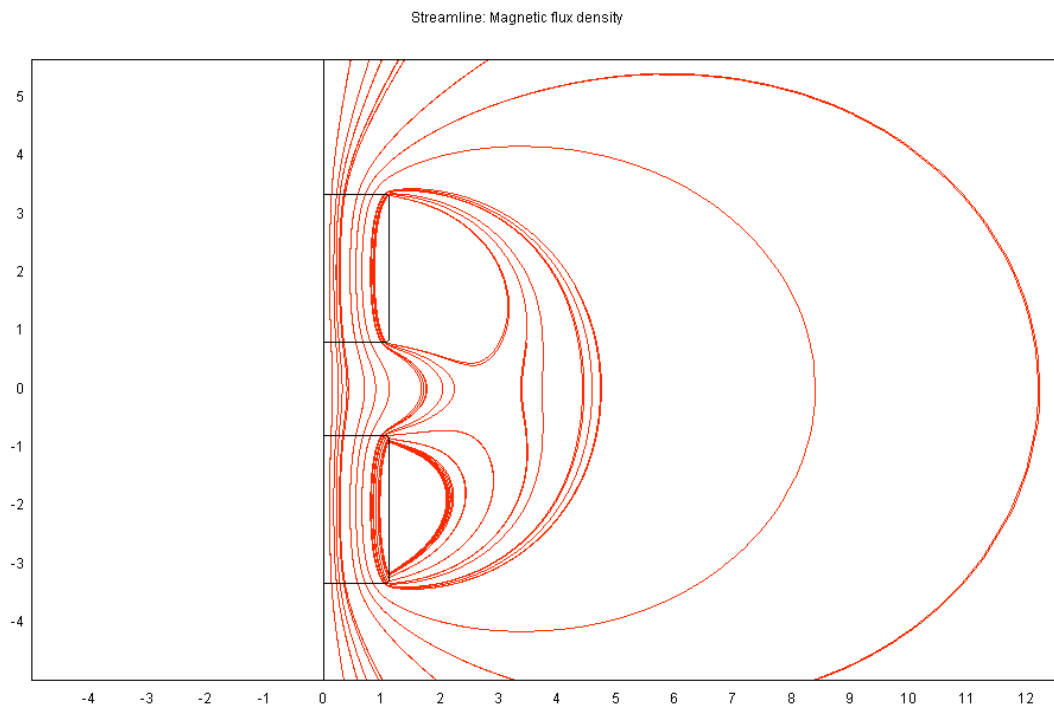


Figure 3.31 Detailed view of the magnetic field in the cross section area of the 7/8 inch diameter magnets

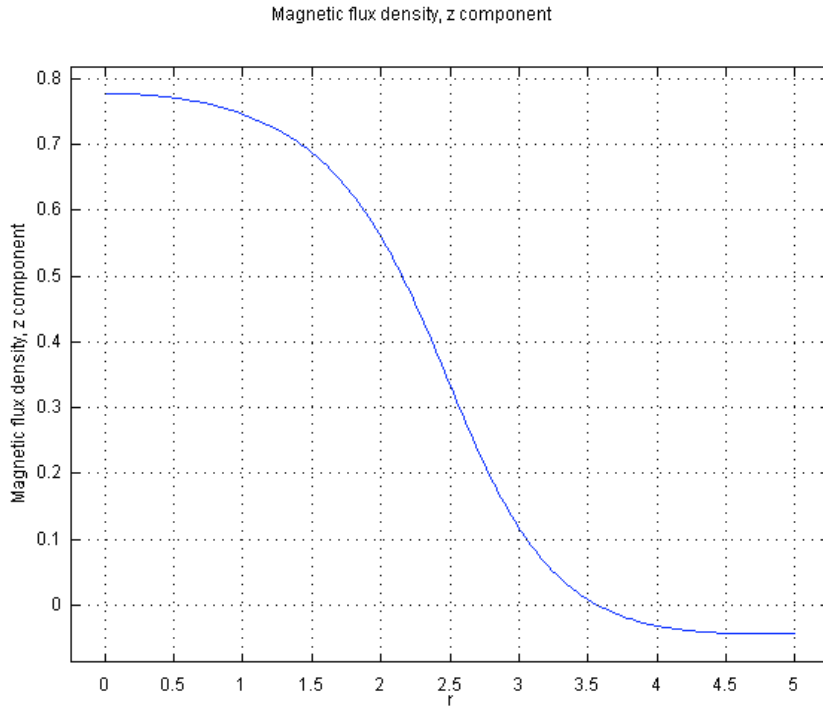


Figure 3.32 The magnetic field flux density plotted as a function of its radial position for the 2 inch diameter magnets.

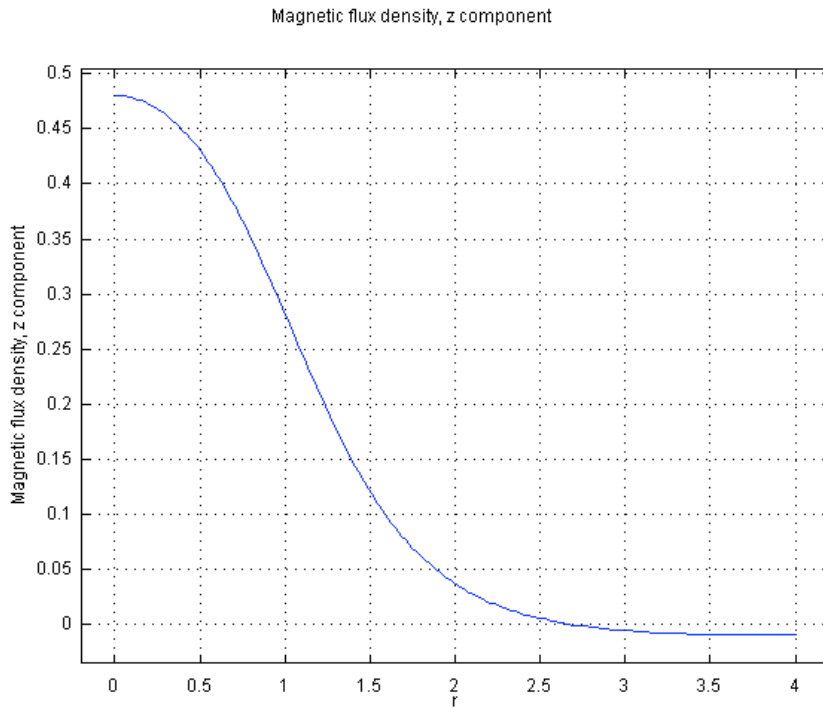


Figure 3.33 The magnetic field flux density plotted as a function of its radial position for the 7/8 inch diameter magnets.

C. The effect of the magnetic field on the dose distribution

The goal of our experiment is to determine RBE in the presence of a magnetic field. Nonetheless, we didn't measure the dose to produce the same biological effect directly. The same biological effect is very difficult to achieve due to practical reasons. The same biological effect cannot be achieved without many trials with different doses. So many trials cannot be finished in a single day. If the trials were done in several days, the environment such as temperature and humidity would change. In each experiment, the *S. cerevisiae* cells need to be transported from the central campus to the north campus for irradiation and then back to the central campus for plating and incubation. The time interval during the process might change, too. The results show that the survival rate varies several percent for different experiments. Therefore, instead of trying to achieve the same biological effect, we tried to make the dose the same with and without the magnetic field and then counted the survival number of cells. Thus the critical step in the experiment is to maintain a constant dose with and without the magnetic field and use proper controls.

C.1 Dose distributions in simplified models

In order to put the cells at an appropriate position for irradiation, the cells are transferred to a nitrocellulose membrane. The membrane can then be attached to clean non-nutrient agar in the Petri dish. The Petri dish can be held at an appropriate position for irradiation. Although the membrane can be attached on the surface of the non-nutrient

agar, it is sandwiched by two layer of agar to achieve charged particle equilibrium. Now we want to know the dose distribution with and without the magnetic field.

We used a transverse uniform magnetic field of 1 T for the simulation. Model 1 (Figure 3.34) has the following assumptions:

- (1) The photon source is a point source with energy 1.25 MeV.
- (2) The phantom is made of water, which is valid because 97.7% of the non-nutrient agar is water.
- (3) The phantom is a cylinder with 1 cm diameter and 10 cm long.
- (4) The distance from the source to the center of the water phantom is 39 cm.
- (5) A transverse uniform magnetic field is applied.

We simulated the situations with and without the magnetic field. The central depth doses of these two cases are compared in Figure 3.36. The size of the sample is 1 cm by 1 cm. The result shows that the doses are the same with and without the magnetic field. Figure 3.37 shows the radial dose profiles at the center of the phantom where the samples are located. The doses are the same in the region where charged particle equilibrium (CPE) is reached. The plot shows that CPE is reached about 3 mm from the surface into the phantom.

It is clear that the surface dose is not uniform with respect to its azimuthal position for a certain z position. Nevertheless, the average surface dose is increased due to the magnetic field. The magnetic field can be decomposed into a component parallel to the surface tangent and component perpendicular to the surface tangent for a specific

azimuthal position. The parallel component will change the surface dose as illustrated in the next model.

Model 2 (Figure 3.35) has the following assumptions:

- (1) The photon source is a point source with energy 1.25 MeV.
- (2) The phantom is made of water.
- (3) The phantom is a cylinder with 10 cm diameter and 1 cm long.
- (4) The distance from the source to the center of the water phantom is 39 cm.
- (5) A transverse uniform magnetic field is applied.

The phantom is equivalent to an infinite large slab of water since we are only interested in the region near the central axis. The central depth dose is plotted in Figure 3.38. When the magnetic field is present, for a unit area, the number of secondary electrons that can go into the front surface of the phantom is reduced. Here the secondary electrons are those produced outside of the phantom. The magnetic field inside the phantom tends to reduce the region where charged particle equilibrium is not reached. However the overall effect is that the front surface dose is reduced.

On the contrary, the back surface dose of the phantom is almost doubled. This effect results from the fact that secondary electrons generated in the phantom and going out of the phantom can return back into the phantom due to the presence of the magnetic field. These secondary electrons lose their energy during going out and back into the phantom and this doubles the dose in that region.

Nonetheless, in the middle part of the phantom, about 3 mm from the surface, the dose is the same with and without the magnetic field.

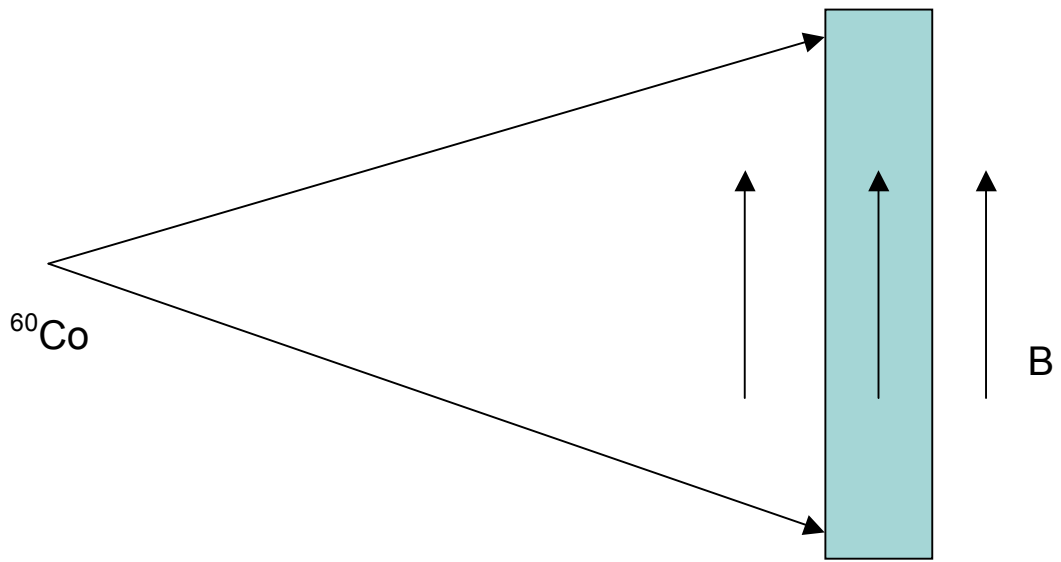


Figure 3.34 Schematic geometry of Model 1.

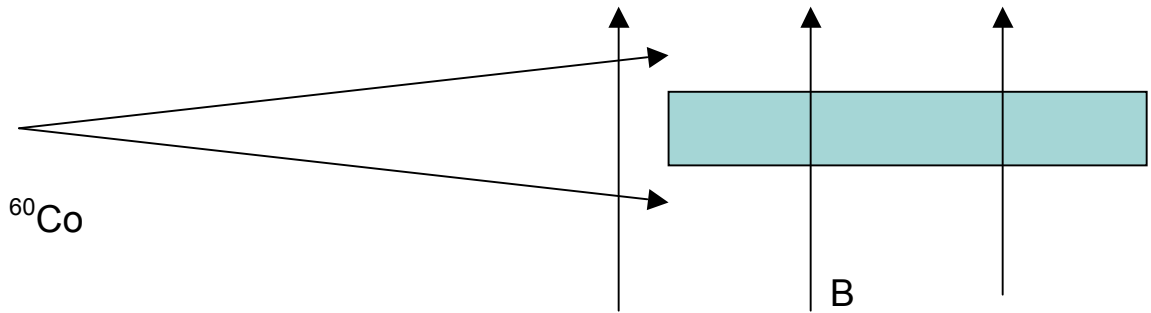


Figure 3.35 Schematic geometry of Model 2

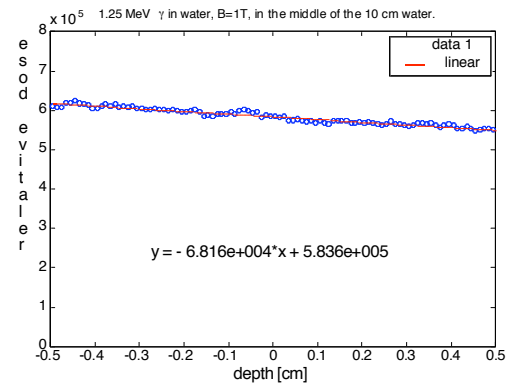
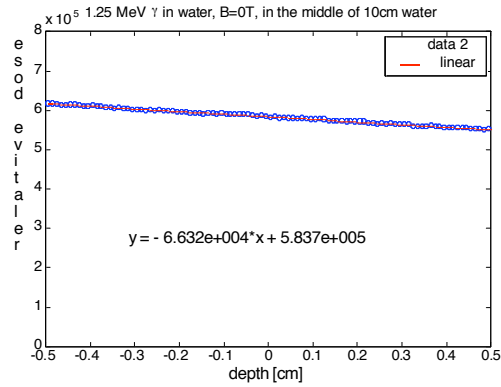


Figure 3.36 Comparison of the depth dose in the middle of the water phantom with and without a transverse magnetic field

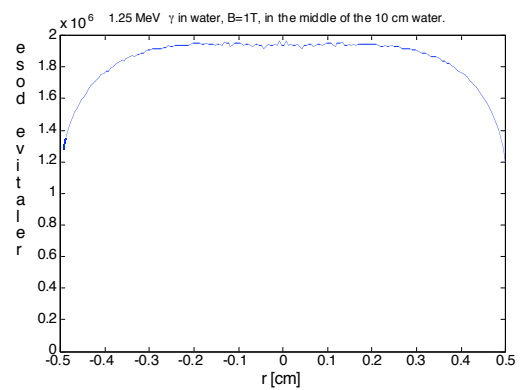
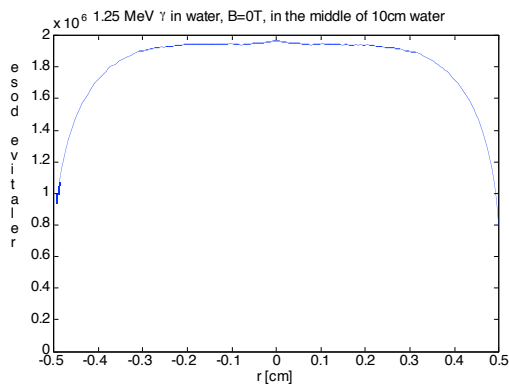


Figure 3.37 Comparison of the radial dose in the middle of the water phantom with and without a transverse magnetic field

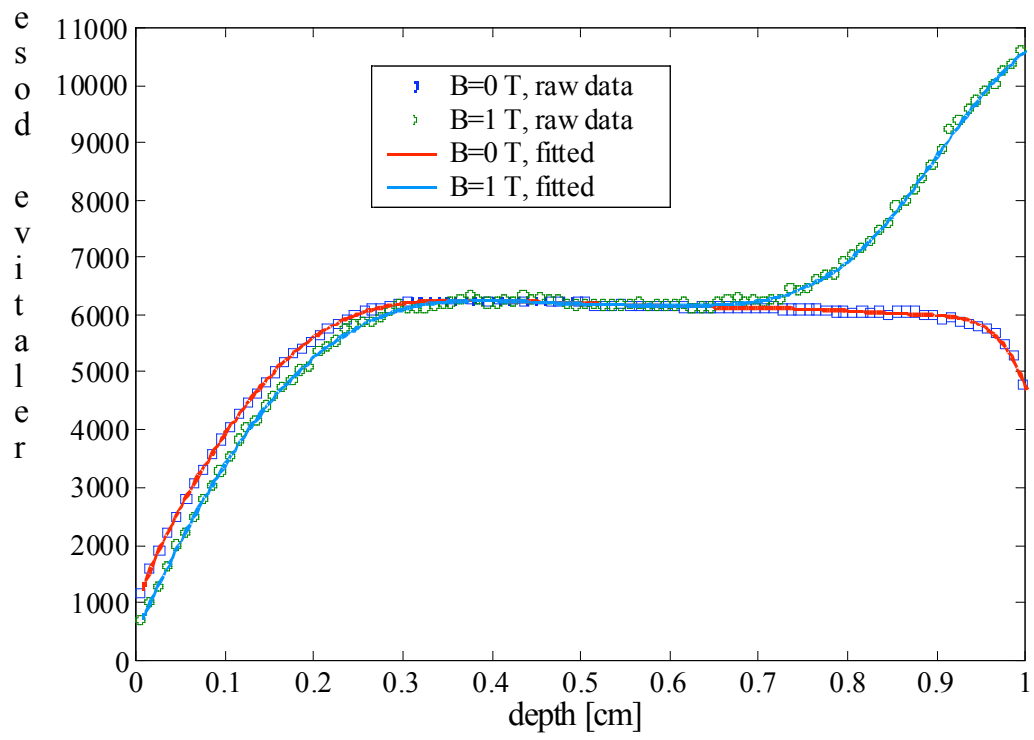


Figure 3.38 Comparison of the depth dose of a 1 cm slab of water with and without a transverse magnetic field.

C.2 Charged particle equilibrium (CPE)

Charged particle equilibrium exists for the volume V if each charged particle of a given type and energy leaving V is replaced by an additional particle of the same energy entering, in terms of expectation values¹⁶. From Figures 3.36 and 3.37, we can see that charged particle equilibrium (CPE) can be reached as long as the thickness of the non-nutrient agar is larger than 3 mm. The thickness of the non-nutrient agar used in the experiments is about 6 mm (Figure 3.39). When CPE is reached, the dose is close to uniformity except for a decay factor. This decay factor mainly results from the decay of the primary photon fluence. In the region of CPE, the dose doesn't change significantly, which leads to a nearly uniform killing rate.

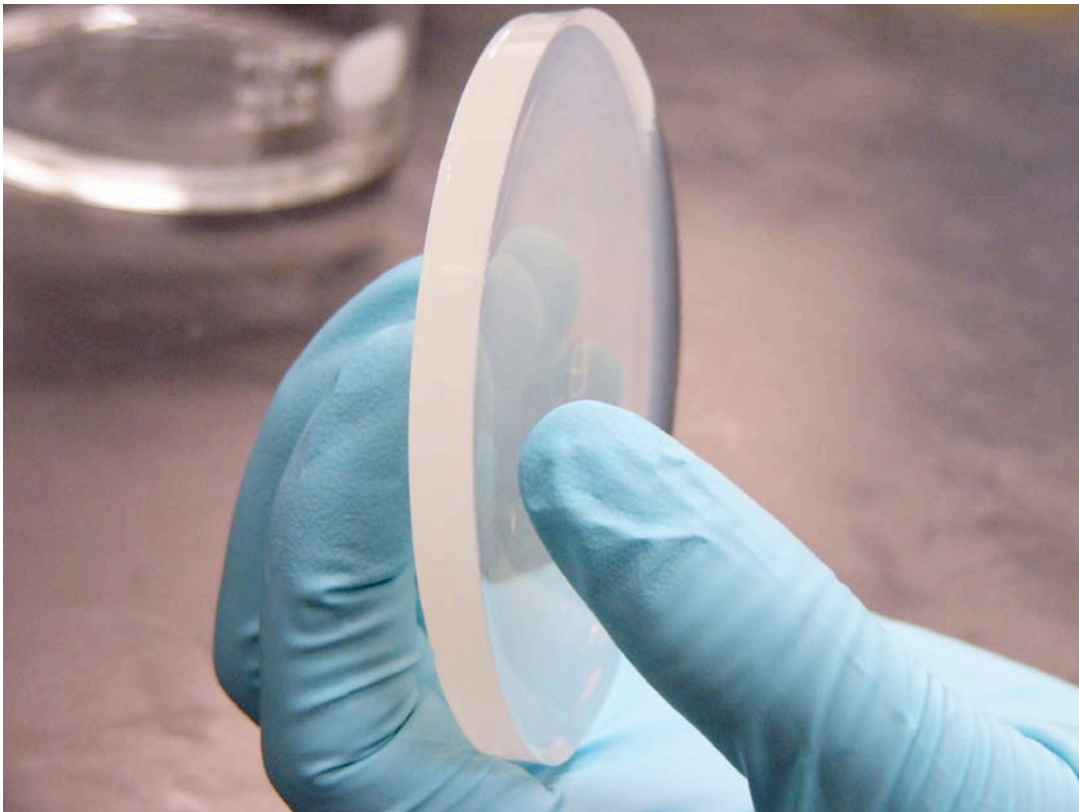


Figure 3.39 One layer of non-nutrient agar

3.2.5 Preparation, irradiation and growth of the cells

The cell line we used is *Saccharomyces cerevisiae*. It is one kind of yeast cells. It is widely used in the experiments to determine the killing effect of radiations¹⁷. It can be cultured and stored easily. Yeast strains can be stored at 4°C on YPD medium (Yeast Extract Peptone Dextrose) in Petri dishes for a short period of time such as a month from our experience. Although most strains can live at 4°C for at least one year, many strains fail to survive even for a few months.

We bought the original cells from Connecticut Valley Biological Supply. The strain we used is radioresistive. We need a radioresistive cell line to be used due to the strong ⁶⁰Co source in the Phoenix Lab. A radioresistive cell line also has a high $\frac{\alpha}{\beta}$ ratio in the linear-quadratic model. This indicates the leading effect will be due to the linear term or α . The parameter α represents the intensity of the double strand breaks due to single track events. We are expecting the main effect of the magnetic field on RBE results from the change in the double strand breaks due to single track events (Figure 3.7).

The original cells are stored in a closed tube at 4°C. The tube contains the YPD medium and some water. The colonies in the tube often contain many dead cells and thus are not suitable for direct use. Colonies of living cells need to be cultured before the cells are used for irradiation. A small amount of cells are scraped from the surface of the tube. These cells are spread on a YPD Petri dish and kept at 26°C. After 3-4 days, the cells grow into continuous colonies. These cells are to be used to make samples to be irradiated.

On the day before irradiation, the cells are transferred to nitrocellulose membranes. The membranes are used to carry the cells and fix them at a specific position. We used 1 cm by 1 cm membranes for both the 2-inch diameter magnets and the 7/8-inch diameter magnets. We also tried 0.5 cm by 0.5 cm membranes for 7/8-inch magnets.

A 2-mL micro tube is used to prepare the cell broth. A small sample of cells were scraped from the Petri dish containing newly cultured cells plated three days prior to making the broth. The sample was put into the micro tube and dissolved in the autoclaved water. The sample usually contained 10^6 cells. We didn't know the exact number in the broth. The micro tube was then put on a Vortex stirring machine for several minutes to de clot the cells and make the broth uniform. The resulting broth is almost clear.

The clean nitrocellulose membrane was cut into 1 cm by 2 cm pieces and laid on the preparation table. Then 8~10 μL of the broth was transferred to each membrane with a pipette and 2 μL of the broth was transferred for the 0.5 cm by 1 cm membranes. The sample of broth would spread on the membrane. The membrane was large enough to guarantee the cells stayed within the boundary of the membrane. The broth dried in several minutes. Then the membrane was folded and the cells were covered by the membrane.

We used non-nutrient agar Petri dishes to carry the membranes and to maintain an environment in CPE for the irradiated cells. The diameter of the Petri dish is 95 mm and the thickness is 15 mm. The non-nutrient agar is about 6 mm thick (Figure 3.39). There were two layers of agar in one Petri dish and the membrane was placed between the two layers. Figure 3.40 shows the agar after the membrane was removed. The membrane could be well embedded in the agar after air was pushed out. There were one or two

membranes in one Petri dish. If more membranes were added, the agar would break when we squeezed out air bubbles between the two layers of agar.

The cells don't grow on the non-nutrient agar. The plates were stored at 4°C before irradiation on the next day. A cross mark was drawn on the Petri dish to ensure the samples to be placed at the center of the magnets.

On the day of irradiation, the sample plates were transported from the central campus to the north campus. The yeast cells are very suitable for transport. Unlike colon cancer cells, yeast cells do not need liquid medium during transport. They can survive for a long time without nutrient. Since the cells are sealed by the non-nutrient agar, contamination during transport and irradiation also is minimized.

A carbonate plastic board was placed on the lid covering the ^{60}Co source well. The magnets and fake magnets ($B=0$) used for control were placed at the $r=39$ cm curve. A T-square was used to make the magnetic field perpendicular to the radius. The gap between the two magnets on the yoke was 1.6 cm. The Petri dish directly touched the magnets. The position of the magnets and fake magnets was fixed by the plastic holder underneath the magnets or fake magnets. The plastic holders were made with exactly the same dimensions.

The sets of magnets and fake magnets were placed alternatively along the circle. In some of the experiments, another set of stand-alone control samples were placed between the magnets and fake magnets. The stand-alone samples were placed on foam pad holders. There were another set of controls located in the hallway near the door where the dose was near the value for the outside ambient environment.

It took about 33 minutes for each irradiation to achieve a 50% survival rate. Usually four irradiations were done in the morning. The positions of the magnets, fake magnets and the controls were fixed in one day's experiment. However, in the experiment of the next date we tried to exchange the positions of the magnets and the fake magnets to minimize the fluence difference due to the non-uniformity of the ^{60}Co irradiation field.

After irradiation, the cell samples were transported back to central campus. They were store at 4°C before plating. Although the exact number of cells on one membrane was not known before the cells grew into visible colonies, we could estimate the number by the following method. The original cell broth can be stored at 4°C and the cells remain alive for at least several weeks. The number of cells in the broth is constant within weeks. Thus we can sample the broth and grow a known amount of broth in a Petri dish. This should be done 2~3 days before the cells are transferred to the membranes. Then by the time of transferring, the cells in the Petri dish have grown into colonies. Now we count the number of colonies and determine roughly the cell concentration in the broth. We didn't control the number of cells on a membrane. Instead, we chose the appropriate dilution to make the number of colonies grown in the Petri dishes to be between 50~300. It is difficult to count the number if it is more than 300 in one plate. However, the statistical relative error increases if the number is too small. The number is ideal for about 100~200.

The cells were washed off the membranes and 20 μL of the broth was sampled and put in the YPD agar plates. The sample of broth was spread across the surface of the agar with a sterilized spreader. The water was almost absorbed and evaporated after spreading. Thus the cells were immobilized and fixed at their locations. If the amount of broth

dropped in the plate was too much, the liquid might flow over the surface and brought some of the new cells to other places. The YPD plates should be flipped up side down after plating. This procedure can prevent condensation accumulating on the agar surface.

The plated cells were incubated at 25~26°C. The size of a yeast cell is about 5~7 μm . The cell is invisible to naked eyes. The living cells began to grow after being plated into the YPD agar plates. Most laboratory strains are haploid. Haploid cells can grow mitotically indefinitely with a doubling time as low as 90 minutes on rich medium¹⁸. The colonies were well formed 72 hours after plating. The un-irradiated cells grew into colonies of similar size as shown in Figure 3.41. However, as shown in Figure 3.42, the size of irradiated cells varies. The colony formed by un-irradiated cells was round and well-shaped. Most of the colony formed by irradiated cells was round but some of them appear to mutate and grow into irregular shapes (Figure 3.43). The number was first counted 48 hours after plating. It was counted again 72 hours after plating. Usually we counted the number once more 96~120 hours after plating. The number counted 72 hours differed substantially from that counted 48 hours. The number gradually became stationary after 72 hours.

Colonies were visible about 36 hours after plating. We started counting 48 hours after plating. After 72 hours, some of the colonies grew large such that they merged. It was difficult to count the number if several colonies merged together. This problem was especially prominent in the case of irradiated cells. Small colonies were engulfed by large ones. We marked the counted cells such that we would not re-count them the next time (Figure 3.41). We didn't count those colonies smaller than 0.5 mm 72 hours after plating.

These colonies remained the same size even 120 hours after plating while the others would grow even larger. This indicates that they died after several generations.

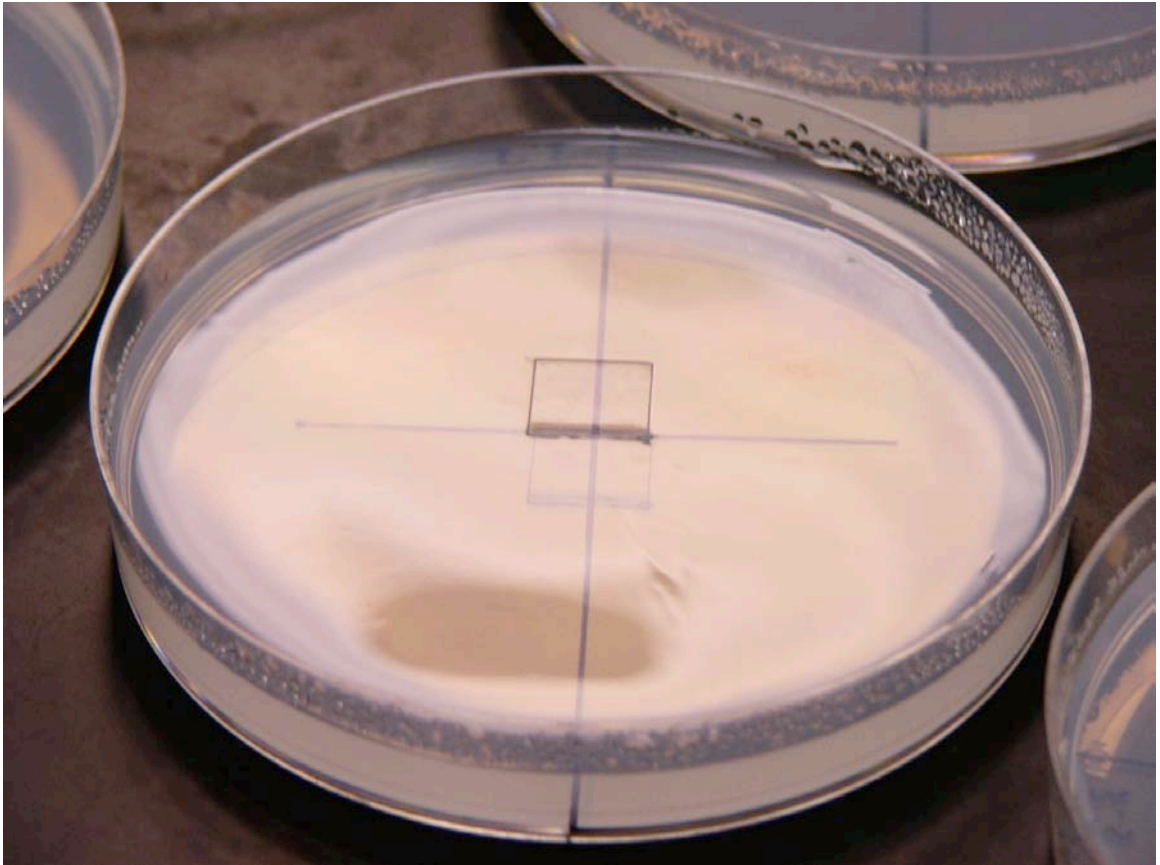


Figure 3.40 The non-nutrient agar plate with the membrane removed



Figure 3.41 Cells without irradiation grew into colonies of similar size.

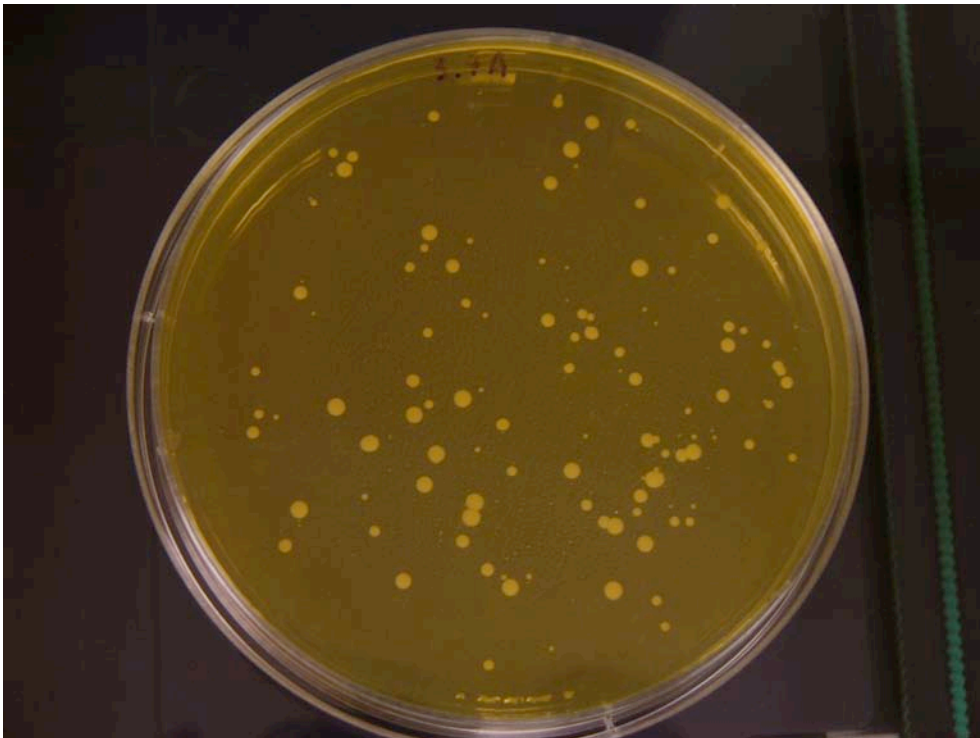


Figure 3.42 Irradiated cells grew into colonies of different sizes.

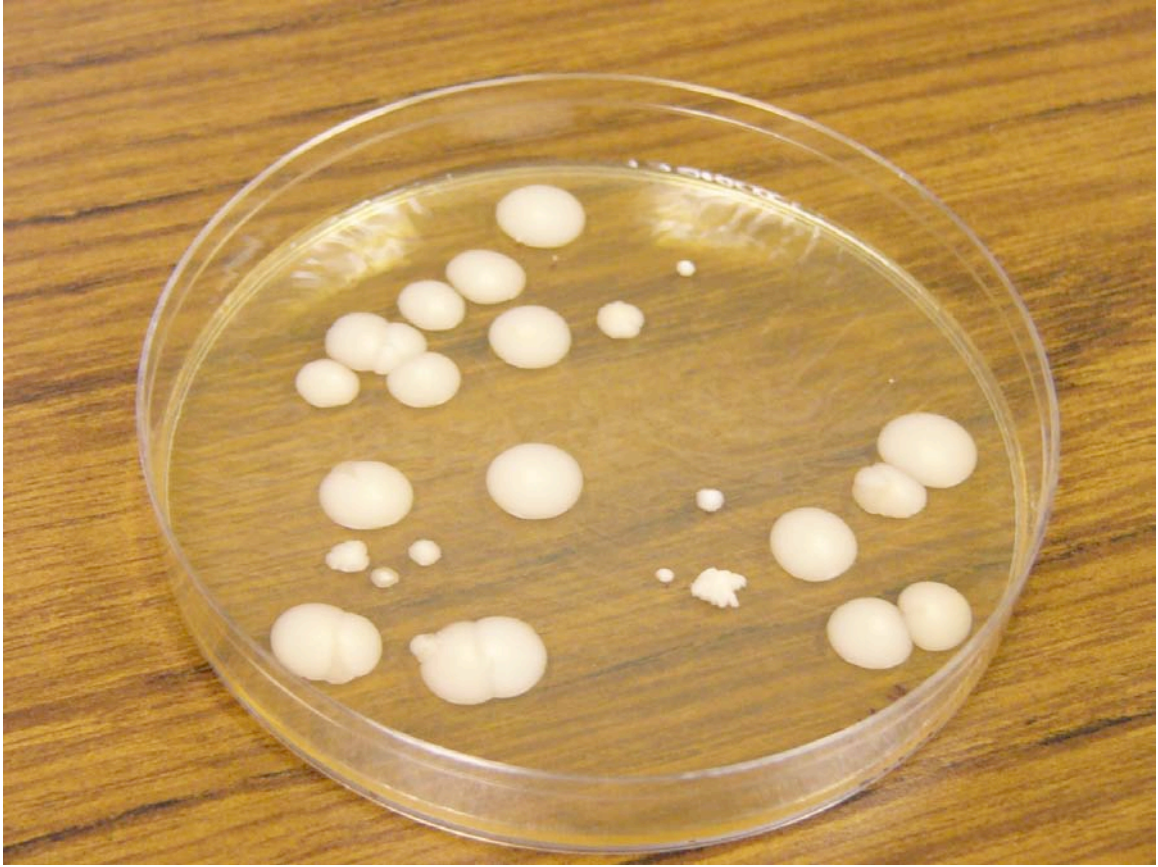


Figure 3.43 Mutants are those colonies of irregular shapes.

3.2.6 Statistical properties of the cultured colonies

A. The minimum uncertainty that we can obtain for our experiment

Our experiment is basically a series of binomial processes. The whole process can be divided into several steps:

(1) Sampling of the original cell broth

The cell broth in a micro tube contains millions of cells in 1.5~2 mL of autoclaved distilled water. The sampling was to transfer 2~10 μL of the broth onto a membrane. This process can be treated as a binomial process with $\text{Bino}(N, n, p_1)$, *i.e.*, taking n cells out of N with a probability $p_1 = \frac{v}{V}$. V is the volume of the broth and v is the volume of the pipet.

(2) Killing of the cells

The sample cells were sealed in the non-nutrient agar and irradiated. The killing process was a binomial process with $\text{Bino}(n, m, p_2)$. m out of n cells survived after the irradiation with a probability p_2 , where $p_2 = 1$ for the sample cells without irradiation.

(3) Washing the cells

The membranes were put in a micro tube and 1.5 mL of water was added. The micro tubes are stirred on a Vortex machine for several minutes. A few cells might not be washed off the membrane. The washing process can be treated as a binomial process with $\text{Bino}(m, b, p_3)$. b out of m cells were washed off the membrane with a probability p_3 .

(4) Dilution and sampling of the broth

The broth containing the cells washed off the membrane was appropriately diluted and 20~30 μL of the broth was put in the YPD agar plates. This process also can be treated as a binomial process with $\text{Bino}(b, d, p_4)$. d cells in the plate was out of b cells in the broth with a probability p_4 .

(5) Plating of the cells

Assume d cells were put in the YPD agar plates and were spread across the surface of agar medium. Only k out of them can grow into colonies. The ratio $p_5 = \frac{k}{d}$ for the cells without irradiation is called the plating efficiency. Again, the process can be treated as a binomial process with $\text{Bino}(d, k, p_5)$.

If we ignore any other uncertainties in these processes, the whole process is a series of binomial processes. It is shown in Appendix B that the whole process is equivalent to a single binomial process. The probability p for the whole process can be expressed as

$$p = p_1 p_2 p_3 p_4 p_5.$$

The pdf of the whole process is

$$\text{Bino}(N, k, p) = \frac{N!}{k!(N-k)!} p^k (1-p)^{N-k},$$

where k is the number that grow into colonies out of N in the broth. Thus the minimum variance we can possibly get from the experiment can be expressed as $\sigma^2 = Np(1-p)$.

The minimum relative error is $\frac{\sigma}{\mu} = \sqrt{\frac{1-p}{Np}}$ with $\frac{\sigma}{\mu} \approx \frac{1}{\sqrt{\mu}}$ when $p \ll 1$ as in our

experiments. This indicates similarity to a Poisson distribution.

B. Uncertainties related to the apparatus and method used in the experiments

The actual uncertainty in the results was much larger than the minimum derived above. This is due to that fact that the probabilities p_i 's in some of steps were not constant for different plates. The probability p for the cells in one plate can differ from that in another plate. The cells in one plate are correlated one another. Thus the probability distribution of the number of cells in one plate is not a simple binomial distribution.

The total probability p of the whole process has its own distribution $f(p)$. The distribution may result from the following factors:

(1) The plating efficiency may be different for different plates.

As noted, the cells in one plate are correlated.

(2) The precision of the pipette is limited.

There are at least five times of pipetting during the process. The first one is for transferring the cells to the membrane. Two of them are pipetting for dilutions. Two of them are for plating. The precision ranges 1~5%.

(3) The cells may leak out of the membrane.

Sometimes the membrane was not folded exactly to cover itself. There might be some area of the inner surface of the membrane touching the non-nutrient agar. Thus some of the cells might stick to the non-nutrient agar. In some cases, the agar was a bit wet. Thus the cells might move out due to water.

(4) The variance of primary fluence at different location and the variance of position of the membrane might result in variance of p .

According to central limit theorem, the distribution of $f(p)$ should approach normal distribution. In order to find an analytical form for $f(p)$, we use beta distribution.

$Beta(p; \alpha, \beta) = \frac{1}{B(\alpha, \beta)} p^{\alpha-1} (1-p)^{\beta-1}$ is the standard beta distribution¹⁹ where

$B(\alpha, \beta) = \frac{\Gamma(\alpha + \beta)}{\Gamma(\alpha)\Gamma(\beta)}$ is the beta function²⁰.

For a standard beta distribution, then mean is $\mu = \frac{\alpha}{\alpha + \beta}$ and the variance is

$$\sigma^2 = \frac{\alpha\beta}{(\alpha + \beta)^2 (\alpha + \beta + 1)}.$$

Given μ_p and σ_p , we can find

$$\alpha = \frac{1 - \mu_p}{\left(\frac{\sigma_p}{\mu_p}\right)^2 - \mu_p} = \mu_p \left(\frac{\mu_p (1 - \mu_p)}{\sigma_p^2} - 1 \right), \quad \beta = (1 - \mu_p) \left(\frac{\mu_p (1 - \mu_p)}{\sigma_p^2} - 1 \right).$$

In our experiments, μ_p is the mean probability of the whole process and σ_p^2 is its variance. When $\alpha \gg 1$ and $\beta \gg 1$, $Beta(p; \alpha, \beta)$ approaches normal distribution. The random variable p in $Beta(p; \alpha, \beta)$ must be from 0 to 1, which is realistic.

Now let's calculate the distribution function of the whole process. The binomial distribution can be rewritten as a beta distribution

$$\begin{aligned} Bino(N, k, p) &= \frac{N!}{k!(N-k)!} p^k (1-p)^{N-k} \\ &= \frac{1}{N+1} \frac{p^k (1-p)^{N-k}}{B(k+1, N-k+1)}, \\ &= \frac{Beta(p; k+1, N-k-1)}{N+1} \end{aligned}$$

The distribution of the whole process becomes

$$\begin{aligned}
 P(N, k) &= \int_0^1 \frac{\text{Beta}(p; k+1, N-k+1)}{N+1} f(p) dp \\
 &= \int_0^1 \frac{\text{Beta}(p; k+1, N-k+1)}{N+1} \text{Beta}(p; \alpha, \beta) dp . \\
 &= \frac{N}{k(N-k)} \frac{B(N, \alpha + \beta)}{B(k, \alpha)B(N-k, \beta)}
 \end{aligned}$$

The mean value is $\bar{k} = \sum_{k=0}^N kP(N, k)$ and the variance is $\text{var}[k] = \sum_{k=0}^N k^2 P(N, k) - \bar{k}^2$.

The increase in variance is shown in Figure 3.44 where the relative error of p is 10%.

We can not determine the variance until the colonies are formed. Therefore we can not separate the process to single out the step that has the largest uncertainty. There is only one step that can be singled out—washing. We can directly plate the samples from the appropriately diluted broth without transferring the cells to the membrane and washing them off. However, the results showed little difference from those with washing.

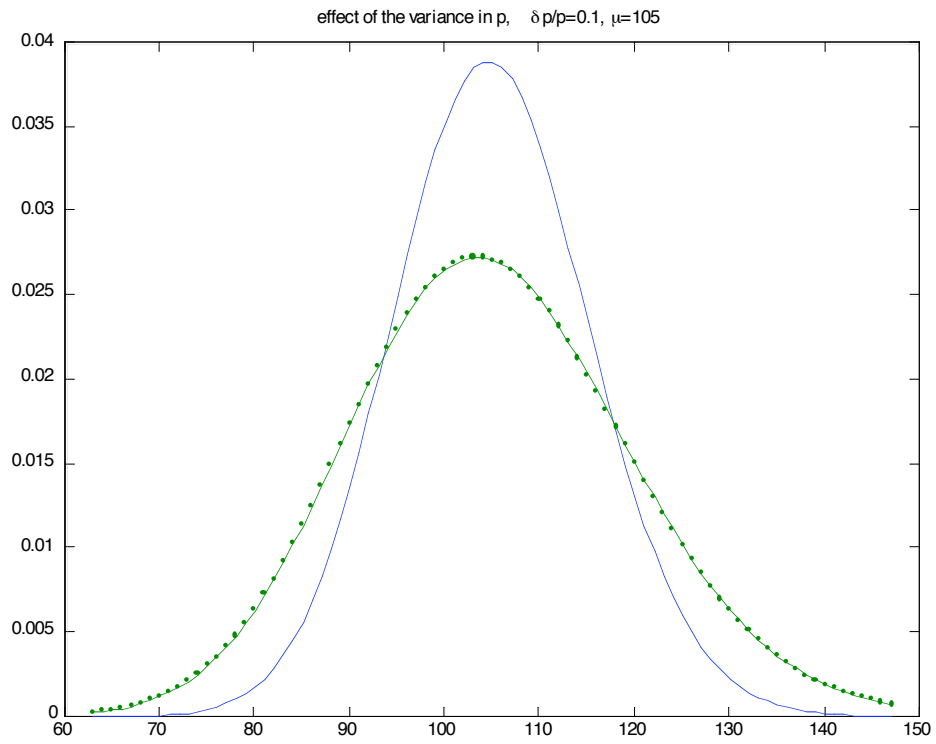


Figure 3.44 Variation in p leads to a broadened binomial distribution.

C. Error reduction

Then the question is how we reduce the relative error. There are several ways. One is to increase the size of the YPD agar plates thus the total number of cells. This method can increase the work load in colony-counting while greatly increase the total number of cells plated. However, calculation (Figures 3.45 and 3.46) shows that it cannot reduce the relative error due to the correlation in one plate if the number of plates is unchanged.

The second way to reduce the uncertainty is to increase the number of YPD plates while keep the size of the plate unchanged. The relative error can be reduced this way but the work load will increase greatly and may not be finished in one day. Longer processing time will bring in more uncertainties. Thus the number of plates can only be limited to a practical number.

The third way to reduce the uncertainty is to first mix the membranes in a tube, sample the broth, and then plate the samples. This method can reduce the variance result from cell transferring and washing. However, it cannot reduce the variance in plating efficiency. We didn't try this method in the experiments. It should be tried in future work.

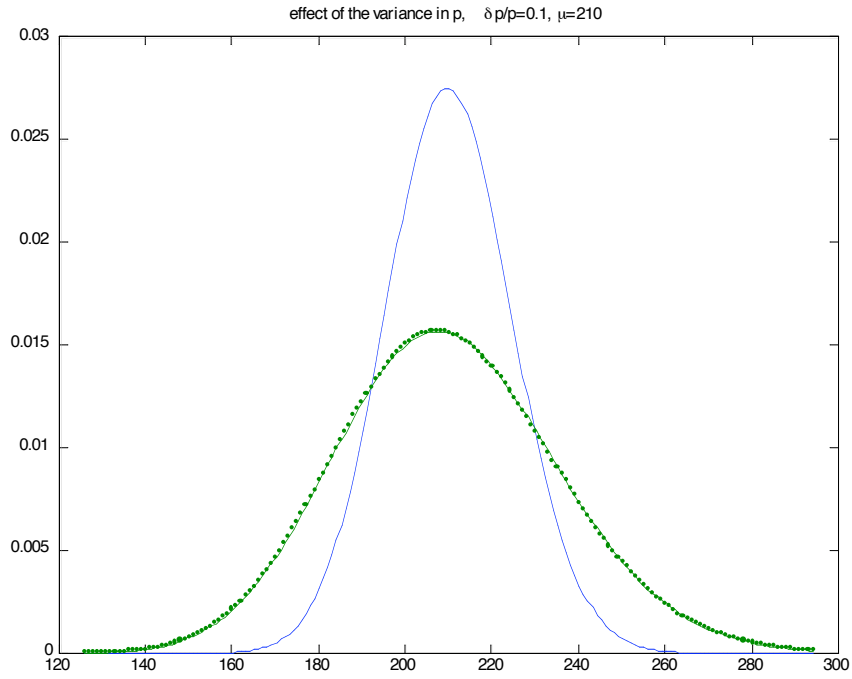


Figure 3.45 A broadened distribution for 210 cells in average.

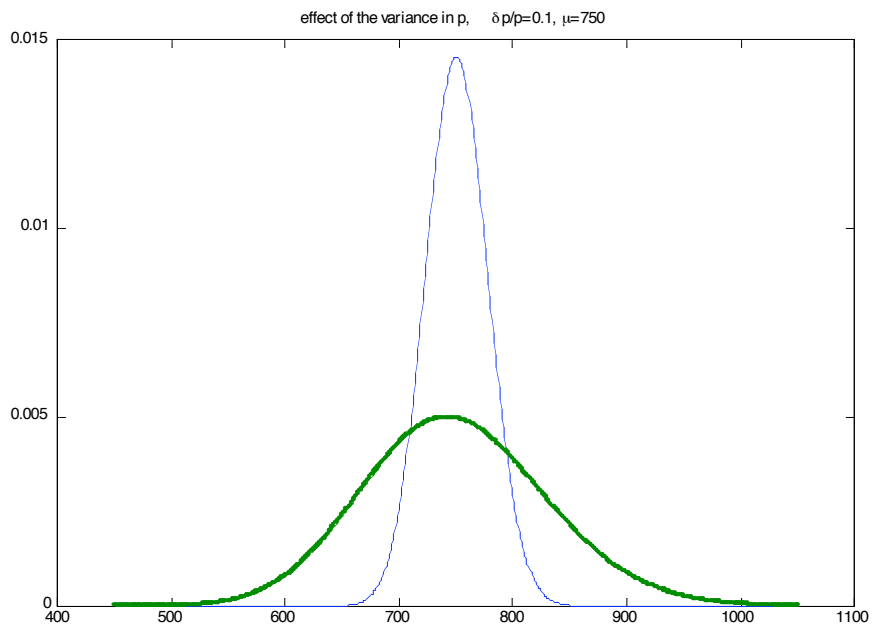


Figure 3.46 A broadened distribution for 750 cells in average.

3.2.7 Results and test of hypotheses

A. Irradiation parameters

Dose rates were measured with a Reuter-Stokes ion chamber model RS-C4-1606-207, serial number Z-8943, which is calibrated annually by the manufacturer or Phoenix against a National Institute of Standards & Technology source.

Table 3.2 Irradiation parameters

Irradiation date	Distance from irradiator [cm]	Gamma dose rate [rad/hr]	Irradiation time [hr]	Gamma dose [rad]
09/21/2004	30	55173	0.544	30297
10/04/2004	30	54916	0.544	30155
10/11/2004	30	54778	0.544	30079
11/23/2004	30	56454	0.527	30058
11/30/2004	30	56312	0.527	29676
12/07/2004	30	56170	0.794	44886
12/20/2004	30	55908	0.543	30685
01/10/2005	30	55487	0.543	30438
01/24/2005	30	55208	0.543	30284
03/01/2005	30	54497	0.543	29895

B. Numbers of survival cells and survival rates for the 7/8-inch magnets

The magnets used in the first set of experiments were 7/8 inch in diameter and 1 inch long. The magnetic flux density was 0.48 T. The nitrocellulose membranes used are 1 cm by 1 cm except for the irradiation on 11/23/2004 and 11/30/2004. The membranes used in those two experiments are 0.5 cm by 0.5 cm.

We counted the numbers of colonies for four different groups—magnet, fake magnet, stand-alone and hall way. “Magnet” represents the group of cells irradiated with the magnetic field. “Fake magnet” represents the group irradiated without the magnetic field but in the same configuration (same geometry and same material) as the magnet group. “Stand-alone” represents the group whose Petri dishes were put on foam pads thus irradiated without the magnetic field and the yoke. “Hall way” represents the group on the floor in the hall way near the entrance door where radiation is close to zero.

(1) Irradiation on 9/21/2004

Counting date	Magnet (B=0.48T)	Fake magnet (B=0)	Stand-alone	Hall way
9/25	111.6±6.1	95.8±4.8	106±12	249±17
9/27	117.6±6.3	104.8±4.9	111±12	249±17
10/5	118.3±6.4	106.3±4.9	112±12	249±17

Survival rate:

Counting date	Magnet (B=0.48T)	Fake magnet (B=0)	Stand-alone
9/25	44.7%	38.4%	41.7%
9/27	47.15%	42.03%	44.37%
10/5	47.45%	42.60%	44.87%

(2) Irradiation on 10/04/2004

Counting date	Magnet (B=0.48T)	Fake magnet (B=0)	Stand-alone	Hall way
10/7	72.7±1.9	68.2±2.5	66.6±3.0	146.5±7.0
10/8	78.1±1.6	75.0±2.4	74.4±3.3	147.8±6.9
10/10	84.8±1.8	80.4±2.2	79.3±3.4	147.8±6.9

Survival rate:

Counting date	Magnet (B=0.48T)	Fake magnet (B=0)	Stand-alone
10/7	49.60%	46.57%	45.46%
10/8	52.85%	50.73%	50.33%
10/10	57.36%	54.38%	53.62%

(3) Irradiation on 10/11/2004

Counting date	Magnet (B=0.48T)	Fake magnet (B=0)	Stand-alone	Hall way
10/15	128.8±3.0	111.8±3.0	113.6±3.2	180.5±9.1
10/17	138.6±3.0	121.6±3.2	121.6±3.4	180.5±9.1

Survival rate:

Counting date	Magnet (B=0.48T)	Fake magnet (B=0)	Stand-alone
10/15	71.35%	61.95%	62.97%
10/17	76.83%	67.40%	67.37%

(4) Irradiation on 11/23/2004

Counting date	Magnet (B=0.48T)		Fake magnet (B=0)		Stand-alone		Hall way	
		std		std		std		std
11/26	62.7±3.4	19.0	69.3±3.1	17.4	63.6±2.4	13.6	112.6±4.7	26.6
11/27	69.2±3.7	20.9	76.7±3.2	17.9	69.7±2.5	13.9	112.7±4.7	26.7

Survival rate:

Counting date	Magnet (B=0.48T)	Fake magnet (B=0)	Stand-alone
11/26	55.66%	61.52%	56.50%
11/27	61.43%	68.05%	61.87%

(5) Irradiation on 11/30/2004

Counting date	Magnet (B=0.48T)	Fake magnet (B=0)	Stand-alone	Hall way
12/02	99.0±3.9	106.1±4.6	105.5±4.8	162.2±7.8
12/04	111.9±4.2	119.6±4.9	116.8±5.1	162.3±7.8

Survival rate:

Counting date	Magnet (B=0.48T)	Fake magnet (B=0)	Stand-alone
12/02	61.03%	65.38%	65.02%
12/04	68.92%	73.67%	71.97%

C. Numbers of survival cells and survival rates for the 2-inch magnets

The magnets used in these experiments were 2 inches in diameter and 1 inch long.

The magnetic flux density was 0.78 T. The membranes used are 1 cm by 1 cm.

(1) Irradiation on 12/07/2004

Counting date	Magnet (B=0.78T)	Fake magnet (B=0)	Stand-alone	Hall way
12/10	139.8±6.3	150.9±3.0	180.3±5.4	285.9±6.0
12/17	157.5±6.1	168.9±3.0	194.9±5.5	285.9±6.0

Survival rate:

Counting date	Magnet (B=0.78T)	Fake magnet (B=0)	Stand-alone
12/10	19.56%	21.11%	25.23%
12/17	22.03%	23.63%	27.27%

(2) Irradiation on 12/20/2004

Counting date	Magnet (B=0.78T)		Fake magnet (B=0)		Stand-alone		Hall way	
		std		std		std		std
12/23	103.8±2.6	14.6	113.3±2.2	12.4	128.9±2.7	15.4	245.5±5.6	31.2
12/24	115.0±2.8	16.0	123.9±2.5	14.1	138.7±2.7	15.3	245.5±5.6	31.2
12/27	118.8±2.8	15.7	127.4±2.6	14.9	141.3±2.8	15.6	245.5±5.6	31.2

Survival rate:

Counting date	Magnet (B=0.78T)	Fake magnet (B=0)	Stand-alone
12/23	42.29%	46.14%	52.51%
12/24	46.87%	50.49%	56.50%
12/27	48.42%	51.91%	57.56%

(3) Irradiation on 01/10/2005

Counting date	Magnet (B=0.78T)	Fake magnet (B=0)	Stand-alone	Hall way
01/14	131.4±2.6	118.9±2.4	137.1±5.0	243.2±4.7

Survival rate:

Counting date	Magnet (B=0.78T)	Fake magnet (B=0)	Stand-alone
01/14	54.03%	48.88%	56.38%

(4) Irradiation on 01/24/2005

Counting date	Magnet (B=0.78T)	Fake magnet (B=0)	Stand-alone	Hall way
01/27	65.3±2.0	65.6±2.7	68.6±2.9	179.3±6.0
01/29	79.3±2.1	79.6±3.1	81.8±3.3	179.9±6.0

Survival rate:

Counting date	Magnet (B=0.78T)	Fake magnet (B=0)	Stand-alone
01/27	36.38%	36.59%	38.26%
01/29	44.10%	44.24%	45.45%

(5) Irradiation on 03/01/2005

Counting date	Magnet (B=0.78T)	Fake magnet (B=0)
03/08	114.5±3.4	120.4±3.5

D. t-test for the difference between the survival number for magnets and that for fake magnets (B=0)

Assume the variance $\sigma_m^2 = \sigma_f^2$. Then we have

$$\frac{(\bar{M} - \bar{F}) - (\mu_m - \mu_f)}{S \sqrt{\frac{1}{n_m} + \frac{1}{n_f}}} \sim t(n_m + n_f - 2).$$

\bar{M} is the unbiased estimate of the number of survival cells for the magnets. \bar{F} is the unbiased estimate of the number of survival cells for the fake magnets. n_m and n_f are the number of sample plates for the magnets and fake magnets respectively.

$$S^2 = \frac{(n_m - 1)S_m^2 + (n_f - 1)S_f^2}{n_m + n_f - 2},$$

where S_m^2 and S_f^2 are the sample variance. $t(n_m + n_f - 2)$ is

the Student distribution of freedom $n_m + n_f - 2$.

We did t-test for the null hypothesis. $H_0: \mu_m = \mu_f$, $H_1: \mu_m \neq \mu_f$. We set a confidence level to $1 - \alpha = 0.95$. The results are listed in Table 3.3.

We can not reject H_0 in every experiment. Here we should divide the experiments into two groups. The first group includes the experiments on 9/21/2004, 10/04/2004 and 10/11/2004. In these three experiments, the survival rate increased when the magnetic field was present. This was due to the non-uniformity of magnetic field. The membranes were not small enough compared with the diameter of the magnets. Since the flux density goes higher as its position goes close to the poles, the dose decreased in the region between the center of the magnetic field and the surface of the poles. The dose increased close to the surface of the pole. Therefore, the dose delivered in the presence of the

magnetic field was less than that without the magnetic field in these three experiments. In other words, the effect on RBE might be neutralized by the reduction of dose.

In the rest of the seven experiments, the ratio of the width of the membrane over the diameter of the magnets was about 0.2. It is small enough such that the magnetic field over the cells can be treated as a uniform field. Thus the doses delivered with and without the magnetic field would be the same. The results are shown in Figure 3.47. The results indicate that the killing ability of the radiation increases in the presence of the magnetic field. Therefore, the RBE increases slightly in the presence of the magnetic field. In our cases, at $B=0.78$ T with the cells and doses we used, the effect of the magnetic field on the survival rate is about $-3.9\% \pm 2.7\%$.

Table 3.3 Results of the experiments

Irradiation date	$\bar{M} - \bar{F}$	$S \sqrt{\frac{1}{n_m} + \frac{1}{n_f}}$	$\frac{\bar{M}}{\bar{F}}$	Reject H_0
9/21/2004	15.8	7.7	1.16	yes
10/04/2004	4.4	3.2	1.07	no
10/11/2004	17.0	4.3	1.15	yes
11/23/2004	-6.6	4.6	0.90	no
11/30/2004	-7.1	6.1	0.93	no
12/07/2004	-11.1	7.0	0.93	no
12/20/2004	-9.4	3.4	0.92	yes
01/10/2005	12.5	3.6	1.11	yes
01/24/2005	-0.4	3.3	0.99	no
03/01/2005	-5.9	4.9	0.95	no

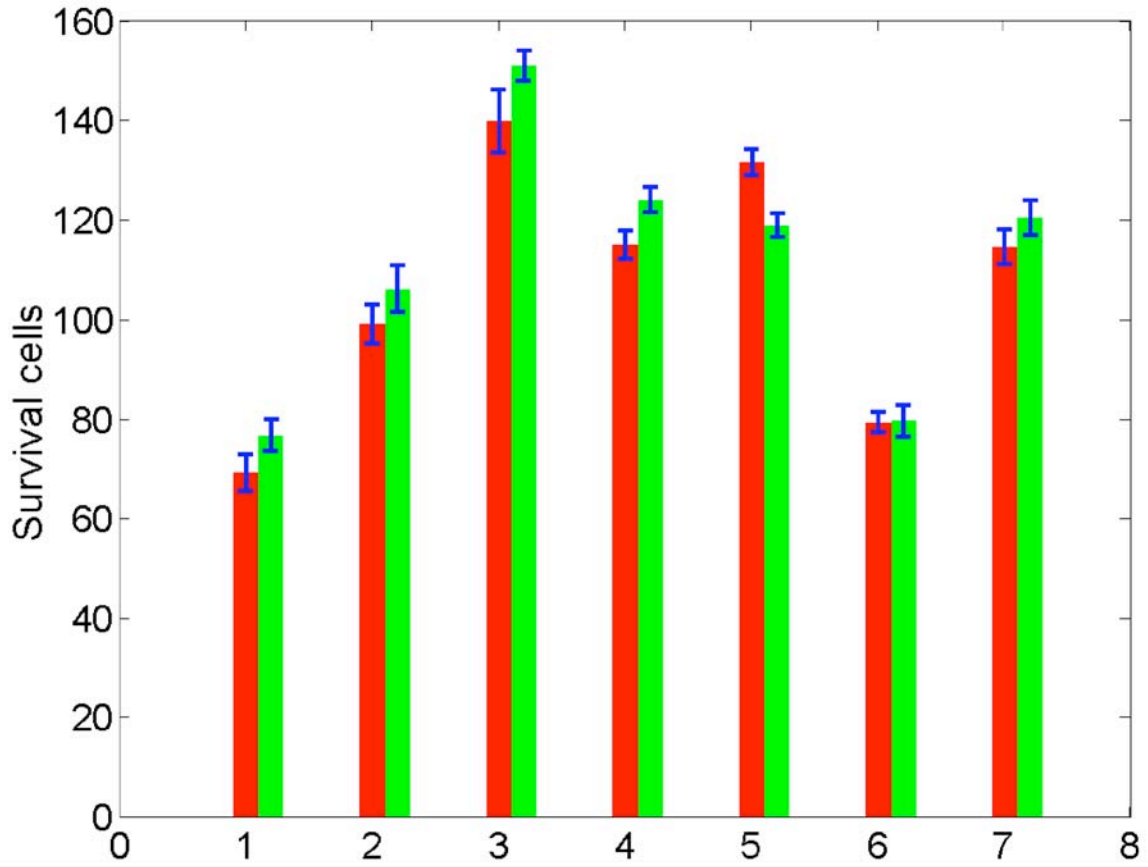


Figure 3.47 The number of survival cells and the standard deviation of the mean are plotted for the experiments where the ratio of the width of the membrane to the diameter of the magnet is 0.2. The left bars are the numbers with the magnet field. The right bars are the numbers without the magnetic field.

3.3 Future work

Although we can set limits at $B=0.78$ T, the results are still inconclusive. The uncertainties are still large due to the limited sample size and the effect observed is of the same order as the uncertainty.

More experimental work should be done to reduce the uncertainties and if possible, a stronger magnetic field should be used to make the effect more prominent.

More theoretical work is needed to explain the possible effect of magnetic fields on RBE.

Likewise, radiobiological electron transport codes should be modified to account for the effect of magnetic fields if the RBE changes in the presence of high magnetic fields.

We are presently investigating the possibility of modifying track structure codes to include magnetic fields. Other studies will likely carry on this work, including studies using electrophoresis of DNA.

References to Chapter 3

-
- ¹ D. Frankenberg, M. Frankenberg-Schwager, D. Blöcher and C. Adamczyk, "Evidence for DNA double strand breaks as the critical lesions in yeast cells irradiated with sparsely or densely ionizing radiation under oxic or anoxic conditions", *Radiation Research* **88**, 524-532 (1981)
- ² M. Frankenberg-Schwager, D. Frankenberg, D. Blöcher, C. Adamczyk, "The linear relationship between DNA double-strand breaks and radiation dose (30 MeV electrons) is converted into a quadratic function by cellular repair", *Int. J. Radiat. Biol.* **37**, NO . 2, 207-212 (1980)
- ³ M. Frankenberg-Schwager, R. Harbich, S. Beckonert and D. Frankenberg, "Half-life values for DNA double-strand break rejoining in yeast can vary by more than an order of magnitude depending on the irradiation conditions", *Int. J. Radiat. Biol.* , 1994, VOL. **66**, NO. 5, 543-547
- ⁴ E. J. Hall, "Radiobiology for the radiologist", Lippincott Williams &Wilkins, 2000, pp 13
- ⁵ S. B. Curtis, "Lethal and potentially lethal lesions induced by radiation--a unified repair model", *Radiat Res.* **106**(2):252-70 (1986) Published erratum appears in *Radiat. Res.* **119** (3), 584 Sep (1989)
- ⁶ D. T. Goodhead, "Saturable repair models of radiation action in mammalian cells", *Radiat. Res.* **104** S58-67 (1985)
- ⁷ G. W. Barendsen, "Dose-survival curves of human cells in tissue culture irradiated with alpha, beta and x-radiation", *Nature* **193** 1153-5 (1962)
- ⁸ A. M. Kellerer and H. H. Rossi, "The theory of dual radiation action", *Curr. Top. Radiat. Res. Quart.* **8** 85-158 (1972)
- ⁹ K. H. Chadwick and H. P. Leenhouts, "The rejoining of DNA double-strand breaks and a model for the formation of chromosomal rearrangements", *Int. J. Radiat. Biol.* **33** 517-29 (1978)
- ¹⁰ C. A. Tobias, "The repair-misrepair model in radiobiology: comparison to other models", *Radiat. Res.* **104** S77-95 (1985)
- ¹¹ R. Taschereau, R. Roy, J. Pouliot, "A comparison of methods to calculate biological effectiveness (RBE) from Monte Carlo simulations", *Med Dosim.* **28**(1):21-6 (2003)
- ¹² D. W. Anderson, "Absorption of Ionizing Radiation", University Park Press 1984 pp 2

-
- ¹³ J. Meesungnoen, J. Jay-Gerin, A. Filali-Mouhim and S. Mankhetkorn, "Low-Energy Electron Penetration Range in Liquid Water," *Radiation Research* **158**, 657-660 (2002)
- ¹⁴ S. Rockwell, "Influence of a 1400-gauss magnetic field on the radiosensitivity and recovery of EMT6 cells *in vitro*", *Int. J. Radiat. Biol.* **31**, 153-160 (1977)
- ¹⁵ R. Nath, R. J. Schults and P. Bongiorni, "Response of mammalian cells irradiated with 30 MV X-rays in the presence of a uniform 20-kilogauss magnetic field", *Int. J. Radiat. Biol.* **38** No. 3, 285-292 (1980)
- ¹⁶ F. H. Attix, "Introduction to Radiological Physics and Radiation Dosimetry", John Wiley & Sons, Inc. ISBN 0-471-01146-0, pp 65
- ¹⁷ F. Sherman, "Getting started with yeast, *Methods Enzymol*", 350, 3-41 (2002)
- ¹⁸ M. F. Tuite and S. G. Oliver, "Saccharomyces", Plenum Press, pp 101, 1991
- ¹⁹ J. L. Devore, "Probability and Statistics for engineering and the sciences", Duxbury Brooks/Cole, pp 183, 2000
- ²⁰ M. Abramowitz and I. A. Stegun, (Eds.) "Beta Function" and "Incomplete Beta Function" §6.2 and 6.6 in "*Handbook of Mathematical Functions with Formulas, Graphs, and Mathematical Tables, 9th printing*" New York: Dover, pp. 258 and 263, 1972

Chapter 4

Conclusion

In chapter 2, we used the Monte Carlo code PENELOPE to simulate existing experimental data¹. The experimental dose profiles are generally reproduced in the simulation to within a few percent. By comparing the simulations with the experiments, we demonstrate that the non-uniform longitudinal magnetic field generated by a solenoid can provide both transverse and longitudinal confinement of an electron beam dose profile. The “3D” confinement results from the focusing effect of the magnetic lens, reduction of lateral scattering of the electrons, and the mirror effect of the magnetic field. Our results show that the MC code PENELOPE has the basic capability of calculating the dose with realistic magnetic fields. However, the primary electron beam energy and the beam-line geometry need to be carefully verified and modeled in order to get an accurate simulation.

From our simulations, we can see that electron dose profiles can be manipulated by the appropriate combination of the beam energy, the strength of the magnetic field, and the position of the target media in the magnetic field. Stereotactic treatment appears possible using magnetically-confined electron beams. The physical collimation and the magnetic confinement have to be suitably adjusted to optimize the dose profile. Since intense primary electron beams are readily available, a high dose rate can be obtained.

In the experiments aimed to investigate the possible effect of the magnetic field on RBE, there is indication that the killing ability of the radiation increases in the presence of a moderate magnetic field. Therefore, the RBE increases slightly in the presence of a modest magnetic field. However, the uncertainties are still large due to the limited sample size as the effect is of the same order as the uncertainty.

Our calculation of the energy deposition proximity function by simulating the track structure with PENELOPE failed to show a significant change in the presence of a magnetic field of the order of 1 T. This might be due to the limitation of the code as it can only track the particles with energy higher than 100 eV while the break of a DNA strand can happen with particle energy as low as tens of eV. Since the mean track length for 100 eV electrons is only tens of nm, there might be other reasons for the effect.

More experimental work should be done in the near future to reduce the uncertainties. Stronger magnetic field should be used to make the effect more prominent. More theoretical work is needed to explain the possible effect of magnetic fields on RBE and radiobiological electron transport codes may need to be modified to account for the effect of magnetic fields if the RBE changes in the presence of magnetic fields. We are investigating the possibility of modifying track structure codes to include magnetic fields.

References to Chapter 4

¹ D. W. Litzenberg, B. A. Fraass, D. L. McShan, T. W. O'Donnell, D. A. Roberts, F. D. Becchetti, A. F. Bielajew, J. M. Moran, "An Apparatus for Applying Strong Longitudinal Magnetic Fields to Clinical Photon and Electron Beams", *Phys Med Bio* V**46** no. 5, pp. N105-N115, (2001)

Appendices

Appendix A

The primary fluence of the ^{60}Co source

The source consists of 9 rods. The length of the rods is 13 inch. The diameter of each rod is 0.5 inch. The centers of the rods are located along a circle with radius 2.5 inch. The activities of the rods are listed in the following table:

Rod #	1	2	3	4	5	6	7	8	9
Activity [Ci]	2660	2770	2660	2690	2850	2610	2720	2800	2770

Let's consider a single rod first. Assume the ^{60}Co source is evenly distributed along the rod. The length of the rod is L . The radial position of the sample is r and the height of the sample is z . The nearest distance from the rod to a sample is 30cm. The mean distance from the rod to the samples is 40 cm while the radius of the rod is 0.635 cm. Thus we

have $\frac{r}{\text{radius of the rod}} > 47$. Since the distance from

the rod to the samples irradiated is much longer than the radius of the rod, let's treat the rod as a thin rod.

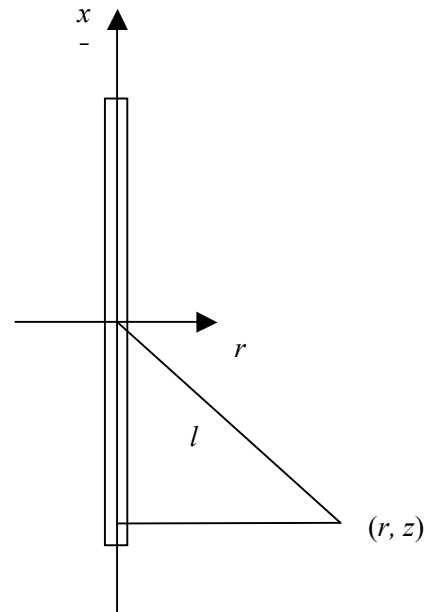
$$l^2 = (z - x)^2 + r^2$$

Let A be the activity of the rod. The fluence generated by the infinitesimal piece from z to $z+dz$ at position (r, z) is

$$d\Phi = \frac{A}{L} \frac{dx}{4\pi l^2} = \frac{A}{4\pi L} \frac{dx}{(z - x)^2 + r^2}$$

$$= \frac{A}{4\pi L r} \frac{d\left(\frac{x}{r}\right)}{1 + \left(\frac{x}{r} - \frac{z}{r}\right)^2}$$

Let $u = \frac{x}{r} - \frac{z}{r}$. We have



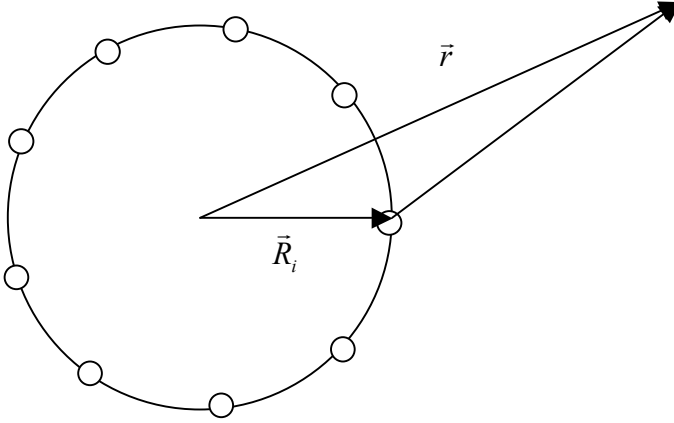
$$\Phi = \int d\Phi = \frac{A}{4\pi L r} \int \frac{du}{1+u^2} = \frac{A}{4\pi L r} \tan^{-1} \left(\frac{x}{r} - \frac{z}{r} \right) \Bigg|_{x=-\frac{L}{2}}^{\frac{L}{2}}$$

$$= \frac{A}{4\pi L r} \left[\tan^{-1} \left(\frac{L}{2r} - \frac{z}{r} \right) - \tan^{-1} \left(\frac{-L}{2r} - \frac{z}{r} \right) \right]$$

Assume the center of the rods lie on the plane of $z=0$. In the plane $z=0$, the position of the rods are $\vec{R}_i, i=1, 2, \dots, 9$. Then the total primary fluence is

$$\Phi = \sum_{i=1}^9 \Phi_i (A_i, |\vec{r} - \vec{R}_i|, z)$$

$$= \sum_{i=1}^9 \frac{A_i}{4\pi L |\vec{r} - \vec{R}_i|} \left[\tan^{-1} \left(\frac{L}{2|\vec{r} - \vec{R}_i|} - \frac{z}{|\vec{r} - \vec{R}_i|} \right) - \tan^{-1} \left(\frac{-L}{2|\vec{r} - \vec{R}_i|} - \frac{z}{|\vec{r} - \vec{R}_i|} \right) \right]$$



Appendix B

Serial Binomial Process

Prove: Two steps of binomial process can be viewed as one binomial process with parameter $p_1 p_2$.

First step, choose M from N with probability p_1 .

$$P(m) = \frac{n!}{m!(n-m)!} p_1^m (1-p_1)^{n-m}$$

Second step, choose K from M with probability p_2 .

$$P(k | M = m) = \frac{m!}{k!(m-k)!} p_2^k (1-p_2)^{m-k}$$

$$\begin{aligned} P(k) &= \sum_{m=k}^n P(k | M = m) P(m) \\ &= \frac{n!}{k!} p_2^k \sum_{m=k}^n \frac{1}{(n-m)!(m-k)!} p_1^m (1-p_1)^{n-m} (1-p_2)^{m-k} \end{aligned}$$

Let $s=m-k$ and $t=n-k$.

$$\begin{aligned} P(k) &= \frac{n!}{k!} p_2^k \sum_{s=0}^t \frac{1}{s!(t-s)!} p_1^{k+s} (1-p_1)^{-s} (1-p_2)^s \\ &= \frac{n!}{k!(n-k)!} (p_1 p_2)^k \sum_{s=0}^t \frac{t!}{s!(t-s)!} (p_1 - p_1 p_2)^s (1-p_1)^{-s} \\ &= \frac{n!}{k!(n-k)!} (p_1 p_2)^k (p_1 - p_1 p_2 + 1 - p_1)^{n-k} \\ &= \frac{n!}{k!(n-k)!} (p_1 p_2)^k (1 - p_1 p_2)^{n-k} \end{aligned}$$

In the case of more than two processes, we can always combine the consecutive two binomial processes into one binomial process. Continue this way until all the processes are combined. The same argument can be applied to a series of finite number of binomial

processes. Thus we proved that a series of binomial processes is equivalent to one single binomial process.

Appendix C

Colonies counts for all the experiments

1. Irradiation on 09/21/2004

9/23/04		Magnet		Fake magnet		Stand-alone		Hallway	
dose	6 ⁻¹	#1	#2	#3	#4	#5	#6	#7	#8
303 Gy	A	96	68	58	51	73	89	149	221
	B	71	65	63	62	78	85	248	214
303 Gy	A	74	55	71	70	85	65	218	303
	B	89	69	59	70	71	73	229	336
303 Gy	A	100	65	78	53	23	114	288	
	B	97	60	81	39	28	119	283	

9/25/04		Magnet		Fake magnet		Stand-alone		Hallway	
dose	6 ⁻¹	#1	#2	#3	#4	#5	#6	#7	#8
303 Gy	A	125	88	80	75	106	104	149	221
	B	96	94	90	89	106	109	248	215
303 Gy	A	119	88	104	104	113	91	219	303
	B	151	103	105	97	98	119	230	336
303 Gy	A	145	101	120	88	29	170	289	
	B	122	107	125	73	42	160	284	

9/27/04		Magnet		Fake magnet		Stand-alone		Hallway	
dose	6 ⁻¹	#1	#2	#3	#4	#5	#6	#7	#8
303 Gy	A	131	94	83	85	110	109	149	221
	B	103	98	99	95	111	114	248	215
303 Gy	A	127	91	114	111	120	102	219	303
	B	161	109	112	109	110	124	230	336
303 Gy	A	148	107	130	101	32	177	289	
	B	129	113	135	84	48	171	284	

10/05/04		Magnet		Fake magnet		Stand-alone		Hallway	
dose	6 ⁻¹	#1	#2	#3	#4	#5	#6	#7	#8
303 Gy	A	132	95	85	86	110	109	149	221
	B	104	98	100	97	111	114	248	215
303 Gy	A	128	91	116	113	122	102	219	303
	B	163	110	114	111	113	124	230	336
303 Gy	A	149	107	130	102	37	178	289	
	B	130	113	136	85	48	175	284	

2. Irradiation on 10/04/2004

10/06/04		Magnet		Fake magnet		Stand-alone		Hall way	
	7 ⁻¹	#1	#2	#3	#4	#5	#6	#7	#8
Group 1 (302Gy)	A	55	50	48	40			105	184
	B	54	52	63	71			95	159
	C	60	60	50	57			103	210
Group 2 (302Gy)	A	42	12	50	55			117	150
	B	51	10	59	45			127	143
	C	56	17	53	49			137	144
Group 3 (302Gy)	A	40	57	38	33			180	156
	B	49	44	48	47			166	152
	C	48	61	41	44			159	150

10/07/03		Magnet		Fake magnet		Stand-alone		Hall way	
	7 ⁻¹	#1	#2	#3	#4	#5	#6	#7	#8
Group 1 (302Gy)	A	71	74	64	57	4	58	105	184
	B	69	68	79	90	5	58	95	159
	C	80	81	69	80	3	59	103	210
Group 2 (302Gy)	A	66	16	74	71	60	53	117	150
	B	69	12	81	62	65	65	127	143
	C	78	21	71	73	64	54	137	144
Group 3 (302Gy)	A	59	86	58	47	76	92	180	156
	B	69	68	69	63	73	90	166	152
	C	69	83	59	61	65	67	159	150

10/08/04		Magnet		Fake magnet		Stand-alone		Hall way	
	7 ⁻¹	#1	#2	#3	#4	#5	#6	#7	#8
Group 1 (302Gy)	A	76	77	68	66	4	65	106	185
	B	79	75	84	99	5	65	99	160
	C	83	86	81	86	4	69	106	211
Group 2 (302Gy)	A	74	18	85	76	73	59	117	150
	B	72	13	84	67	73	71	128	144
	C	82	24	75	76	72	56	139	145
Group 3 (302Gy)	A	65	89	74	56	86	100	182	156
	B	77	76	73	70	83	99	167	155
	C	76	85	65	65	72	74	159	152

10/10/04		Magnet		Fake magnet		Stand-alone		Hall way	
	7 ⁻¹	#1	#2	#3	#4	#5	#6	#7	#8
Group 1 (302Gy)	A	82	80	73	74	6	69	106	185
	B	84	82	88	100	5	70	99	160
	C	86	94	87	93	4	71	106	211
Group 2 (302Gy)	A	83	21	90	79	80	63	117	150
	B	78	16	87	78	77	75	128	144
	C	91	25	81	82	78	59	139	145
Group 3 (302Gy)	A	69	95	79	60	89	102	182	156
	B	84	87	78	75	86	106	167	155
	C	83	94	72	71	79	85	159	152

3. Irradiation on 10/11/2004

10/13/04	(20 μ L)	Magnet		Fake magnet		Stand-alone		Hall way	
	6 ⁻¹	#1	#2	#3	#4	#5	#6	#7	#8
Group 1 (301Gy)	A	118	23	72	64	89	119	255	153
	B	111	19	70	104	96	106	240	150
	C	114	31	87	109	91	98	283	158
	D	98	21	80	90	78	98	275	150
Group 2 (301Gy)	A	104	88	86	94	109	114	71	170
	B	93	91	83	76	99	117	113	187
	C	89	86	92	87	77	106	90	189
	D	108	82	88	72	95	96	95	185
Group 3 (301Gy)	A	138	119	93	95	132	4	149	106
	B	100	118	104	119	117	10	128	110
	C	112	138	106	92	102	13	131	85
	D	126	112	111	120	128	6	156	103
Group 4 (301Gy)	A	117	104	106	101	80	78	143	185
	B	120	90	88	99	98	84	142	193
	C	120	100	115	102	94	92	148	173
	D	116	99	99	106	77	81	132	197

10/14/04	(20 μ L)	Magnet		Fake magnet		Stand-alone		Hall way	
	6 ⁻¹	#1	#2	#3	#4	#5	#6	#7	#8
Group 1 (301Gy)	A	128	26	83	77	95	133	257	154
	B	125	25	79	117	105	118	241	153
	C	134	34	105	132	108	115	285	159
	D	104	26	94	105	87	112	278	151
Group 2 (301Gy)	A	132	107	104	111	127	133	71	172
	B	119	106	104	89	117	135	114	189
	C	108	118	112	99	89	119	90	192
	D	136	109	106	90	111	115	96	187
Group 3 (301Gy)	A	165	150	111	105	140	5	151	108
	B	123	139	122	132	132	13	133	110
	C	133	156	133	108	124	14	133	86
	D	148	134	137	144	155	7	157	103
Group 4 (301Gy)	A	138	130	129	118	94	92	143	186
	B	147	109	118	121	113	99	142	197
	C	138	115	135	119	116	109	149	175
	D	133	121	115	123	95	94	134	200

10/17/04	(20μL)	Magnet		Fake magnet		Stand-alone		Hall way	
	6 ⁻¹	#1	#2	#3	#4	#5	#6	#7	#8
Group 1 (301Gy)	A	140	33	95	88	100	143	257	154
	B	134	29	87	124	107	121	241	154
	C	144	36	113	139	113	125	285	159
	D	111	29	98	113	92	118	279	151
Group 2 (301Gy)	A	139	114	112	126	136	142	71	172
	B	126	120	111	101	123	145	115	190
	C	122	135	126	103	101	129	90	192
	D	143	115	127	99	121	121	96	187
Group 3 (301Gy)	A	173	162	123	110	148	6	151	108
	B	135	152	137	144	139	13	135	110
	C	142	157	143	114	137	15	135	87
	D	162	144	150	152	169	7	157	103
Group 4 (301Gy)	A	152	137	142	127	108	98	144	187
	B	157	118	128	127	116	106	144	197
	C	147	125	148	126	124	113	150	175
	D	146	130	126	133	108	101	134	201

4. Irradiation on 11/23/2004

11/25/2004	(12 μ L)	Magnet		Fake magnet		Stand-alone		Hall way	
	direct	#1	#2	#3	#4	#5	#6	#7	#8
Group 1 (301Gy)	A	48	32	56	31	47	41	92	114
	B	49	32	36	34	47	38	82	127
	C	44	37	39	21	54	34	106	98
	D	44	32	42	21	48	36	80	101
Group 2 (301Gy)	A	62	40	69	37	32	41	146	88
	B	62	43	59	35	42	41	162	72
	C	58	59	48	39	48	27	147	78
	D	46	49	50	45	43	44	140	70
Group 3 (301Gy)	A	19	39	70	42	74	62	130	109
	B	16	45	51	43	47	56	134	118
	C	23	49	48	40	51	54	139	114
	D	21	40	54	33	55	59	131	102
Group 4 (301Gy)	A	52	33	39	53	38	42	83	123
	B	71	36	62	55	31	38	81	120
	C	54	25	57	41	39	41	83	153
	D	52	26	52	38	35	45	98	134

11/26/2004	(12 μ L)	Magnet		Fake magnet		Stand-alone		Hall way	
	direct	#1	#2	#3	#4	#5	#6	#7	#8
Group 1 (301Gy)	A	66	43	80	47	63	55	94	114
	B	83	55	64	55	69	54	83	127
	C	69	56	62	38	68	50	109	98
	D	64	46	67	36	68	46	80	101
Group 2 (301Gy)	A	86	57	104	49	43	52	146	88
	B	84	68	102	54	60	53	163	72
	C	95	76	89	63	64	42	151	78
	D	76	70	82	63	62	60	141	70
Group 3 (301Gy)	A	26	60	95	61	100	84	133	112
	B	28	66	83	58	78	84	138	118
	C	40	77	79	64	73	80	145	118
	D	33	70	86	57	74	87	136	103
Group 4 (301Gy)	A	82	52	57	65	62	63	86	125
	B	86	47	90	82	47	57	81	122
	C	84	37	85	65	64	57	83	153
	D	82	41	78	56	54	62	99	135

11/27/2004	(12 μ L)	Magnet		Fake magnet		Stand-alone		Hall way	
11RB	direct	#1	#2	#3	#4	#5	#6	#7	#8
Group 1 (301Gy)	A	70	53	89	56	65	61	94	114
	B	91	64	68	61	79	58	83	127
	C	77	65	66	47	76	56	109	98
	D	76	49	76	41	75	50	80	101
Group 2 (301Gy)	A	92	66	113	55	50	57	146	88
	B	96	79	106	58	68	60	163	72
	C	104	82	103	69	75	45	151	78
	D	82	77	92	75	63	68	141	70
Group 3 (301Gy)	A	30	67	99	67	102	94	133	112
	B	30	73	90	63	85	91	138	118
	C	42	91	88	69	76	86	146	118
	D	34	78	94	64	84	90	136	106
Group 4 (301Gy)	A	90	56	63	74	68	71	86	125
	B	89	48	97	90	55	67	81	122
	C	92	42	94	76	71	61	83	153
	D	87	43	82	69	57	67	99	135

5. Irradiation on 11/30/2004

12/01/2004	(12 μ L)	Magnet		Fake magnet		Stand-alone		Hall way	
11RB	direct	#1	#2	#3	#4	#5	#6	#7	#8
Group 1 (297Gy)	A	74	63	96	63	75	65	94	114
	B	97	72	77	69	89	62	83	127
	C	84	77	72	56	85	63	109	98
	D	86	55	82	57	84	53	80	101
Group 2 (297Gy)	A	95	71	116	58	60	63	146	88
	B	97	85	107	64	75	66	163	72
	C	107	85	109	73	83	47	151	78
	D	86	84	98	78	65	73	141	70
Group 3 (297Gy)	A	33	80	102	68	108	98	133	112
	B	31	82	99	69	95	99	138	118
	C	44	97	95	69	83	91	146	118
	D	39	90	100	69	90	101	136	106
Group 4 (297Gy)	A	94	67	67	78	73	78	86	125
	B	95	57	103	97	58	70	81	122
	C	97	51	101	85	80	70	83	153
	D	90	47	92	73	63	72	99	135

12/02/04	(16 μ L)	Magnet		Fake magnet		Stand-alone		Hall way	
11RB	direct	#1	#2	#3	#4	#5	#6	#7	#8
Group 1 (297Gy)	A	137	77	122	63	117	66	136	143
	B	133	72	114	83	119	83	126	172
	C	103	84	114	70	108	86	142	150
	D	105	79	107	73	104	81	148	131
Group 2 (297Gy)	A	92	105	181	98	116	84	216	103
	B	94	99	161	77	94	80	207	124
	C	109	115	139	86	97	99	166	89
	D	114	94	138	84	100	84	242	103
Group 3 (297Gy)	A	43	93	116	102	134	150	199	177
	B	32	81	115	108	153	149	191	188
	C	33	84	123	89	160	126	203	197
	D	32	100	125	81	154	139	181	169
Group 4 (297Gy)	A	115	82	104	128	95	85	118	208
	B	129	69	93	119	86	80	105	177
	C	118	83	81	97	85	65	94	235
	D	138	68	106	97	106	90	115	236

12/04/04	(16 μ L)	Magnet		Fake magnet		Stand-alone		Hall way	
11RB	direct	#1	#2	#3	#4	#5	#6	#7	#8
Group 1 (297Gy)	A	153	84	135	70	128	76	136	143
	B	145	80	129	88	136	95	126	172
	C	121	91	122	82	117	96	142	150
	D	115	89	114	88	120	91	149	131
Group 2 (297Gy)	A	109	120	195	113	130	92	216	103
	B	105	110	173	92	102	93	207	124
	C	131	129	148	103	105	104	167	89
	D	126	111	150	97	116	99	242	103
Group 3 (297Gy)	A	47	114	126	110	149	165	199	177
	B	44	97	129	124	160	165	192	188
	C	39	101	149	108	173	135	204	197
	D	42	111	156	89	175	145	181	169
Group 4 (297Gy)	A	125	88	116	143	106	95	118	208
	B	144	76	103	135	94	87	105	177
	C	132	93	93	116	92	79	94	235
	D	153	80	119	112	117	102	115	236

6. Irradiation on 12/07/2004

12/09/04	(20 μ L)	Magnet		Fake magnet		Stand-alone		Hall way	
12RB		#1	#2	#3	#4	#5	#6	#7	#8
Group 1 (449Gy)	A	90	113	108	119	130	140	224	306
	B	95	94	95	116	133	126	253	302
	C	79	99	101	117	130	128	248	329
	D	79	80	86	101	119	149	295	312
	E	91	107	112	102	126	128	246	301
Group 2 (449Gy)	A	108	40	70	91	123	129	317	292
	B	94	48	65	104	109	130	319	288
	C	97	58	75	77	115	143	330	272
	D	90	50	98	81	115	118	324	325
	E	100	51	86	93	114	132	290	272
Group 3 (449Gy)	A	161	75	134	110	135	179	297	230
	B	131	58	113	113	118	178	310	248
	C	126	84	119	115	105	202	331	245
	D	133	82	96	88	124	181	264	249
	E	129	78	99	105	136	181	291	245

12/10/04	(20 μ L)	Magnet		Fake magnet		Stand-alone		Hall way	
12RB		#1	#2	#3	#4	#5	#6	#7	#8
Group 1 (449Gy)	A	137	154	160	158	172	184	225	307
	B	143	136	145	164	184	174	253	302
	C	125	156	151	160	188	187	248	330
	D	134	133	129	155	170	192	295	313
	E	144	163	165	156	169	184	247	301
Group 2 (449Gy)	A	163	69	119	145	158	162	317	292
	B	158	93	104	155	144	170	319	288
	C	169	102	140	131	143	185	330	272
	D	157	87	135	150	157	158	326	325
	E	152	102	134	167	147	184	294	272
Group 3 (449Gy)	A	205	105	174	155	187	225	297	230
	B	178	86	162	161	156	227	311	250
	C	189	131	166	166	144	264	332	245
	D	187	129	170	146	159	224	266	250
	E	194	113	138	165	174	237	293	246

12/17/04	(20μL)	Magnet		Fake magnet		Stand-alone		Hall way	
12RB		#1	#2	#3	#4	#5	#6	#7	#8
Group 1 (449Gy)	A	149	161	169	172	182	193	225	307
	B	157	151	152	173	195	185	253	302
	C	138	162	160	170	197	198	248	330
	D	147	159	151	179	177	204	295	313
	E	152	171	180	165	178	194	247	301
Group 2 (449Gy)	A	187	99	137	162	170	173	317	292
	B	181	110	124	167	167	187	319	288
	C	187	120	154	162	151	208	330	272
	D	172	106	158	170	172	178	326	325
	E	169	119	148	178	163	193	294	272
Group 3 (449Gy)	A	222	119	201	174	203	237	297	230
	B	195	116	178	191	179	243	311	250
	C	214	154	183	186	165	278	332	245
	D	210	150	192	182	182	250	266	250
	E	210	137	168	181	190	255	293	246

7. Irradiation on 12/20/2004

12/23/04	(20 μ L)	Magnet		Fake magnet		Stand-alone		Hall way	
12RB	6 ⁻¹	#1	#2	#3	#4	#5	#6	#7	#8
Group 1 (301Gy)	A	103	105	104	106	119	114	253	271
	B	91	122	101	120	134	130	233	198
	C	86	97	108	99	131	132	240	225
	D	95	106	90	106	116	107	260	221
Group 2 (301Gy)	A	94	97	110	132	110	155	277	201
	B	120	131	103	120	113	123	264	206
	C	119	110	100	125	98	152	230	189
	D	108	110	112	121	100	153	304	884
Group 3 (301Gy)	A	102	97	124	127	135	127	281	291
	B	98	80	103	115	122	122	259	265
	C	94	88	104	109	122	141	243	307
	D	107	70	109	117	141	135	266	276
Group 4 (301Gy)	A	128	108	105	115	148	122	221	244
	B	116	92	93	126	149	129	251	249
	C	134	118	123	137	147	117	225	216
	D	100	96	117	143	147	133	242	200

12/24/04	(20 μ L)	Magnet		Fake magnet		Stand-alone		Hall way	
12RB	6 ⁻¹	#1	#2	#3	#4	#5	#6	#7	#8
Group 1 (301Gy)	A	108	117	114	109	131	120	253	271
	B	98	135	106	130	143	136	233	198
	C	91	104	120	105	136	141	240	225
	D	100	112	95	116	122	116	260	221
Group 2 (301Gy)	A	113	113	127	145	118	168	277	201
	B	132	148	115	125	125	140	264	206
	C	132	124	113	134	114	161	230	189
	D	124	120	125	139	117	163	304	884
Group 3 (301Gy)	A	112	108	135	137	145	139	281	291
	B	111	91	115	125	128	134	259	265
	C	106	101	119	120	132	147	243	307
	D	124	78	115	133	155	146	266	276
Group 4 (301Gy)	A	136	117	114	124	153	124	221	244
	B	127	99	102	136	160	138	251	249
	C	147	127	143	151	159	129	225	216
	D	114	112	126	153	157	141	242	200

12/27/04	(20μL)	Magnet		Fake magnet		Stand-alone		Hall way	
12RB	6 ⁻¹	#1	#2	#3	#4	#5	#6	#7	#8
Group 1 (301Gy)	A	110	121	115	110	136	121	253	271
	B	99	139	110	135	144	136	233	198
	C	96	105	122	106	136	142	240	225
	D	102	117	97	117	128	118	260	221
Group 2 (301Gy)	A	115	118	132	147	118	172	277	201
	B	137	149	118	131	126	141	264	206
	C	138	128	117	141	115	162	230	189
	D	126	120	126	142	120	164	304	884
Group 3 (301Gy)	A	114	110	139	143	146	140	281	291
	B	113	99	117	128	130	138	259	265
	C	111	105	122	126	134	151	243	307
	D	132	83	117	136	159	150	266	276
Group 4 (301Gy)	A	139	120	117	129	156	129	221	244
	B	129	107	106	140	162	143	251	249
	C	149	133	148	156	164	132	225	216
	D	121	118	130	157	162	146	242	200

8. Irradiation on 01/10/2005

1/12/05	(20 μ L)	Magnet		Fake magnet		Stand-alone		Hall way	
13RB	6 ⁻¹	#1	#2	#3	#4	#5	#6	#7	#8
Group 1 (304Gy)	1A	69	77	69	11	77	67	273	256
	1B	57	83	51	10	71	80	254	245
	2A	71	71	70	56	108	104	255	249
	2B	82	61	81	57	106	96	246	263
Group 2 (304Gy)	1A	84	63	53	69	88	75	216	257
	1B	90	62	48	70	102	82	233	243
	2A	83	92	68	86	106	98	249	94
	2B	106	85	72	62	113	98	199	99
Group 3 (304Gy)	1A	103	70	7	73	90	100	286	221
	1B	85	83	12	65	88	89	249	236
	2A	80	79	70	41	62	117	233	212
	2B	104	82	81	50	49	131	273	254
Group 4 (304Gy)	1A	74	76	74	79	110	109	276	195
	1B	80	67	75	72	107	78	278	199
	2A	90	91	96	78	42	98	256	208
	2B	96	98	71	76	54	90	251	200

1/14/05	(20 μ L)	Magnet		Fake magnet		Stand-alone		Hall way	
13RB	6 ⁻¹	#1	#2	#3	#4	#5	#6	#7	#8
Group 1 (304Gy)	1A	111	127	123	24	120	112	275	256
	1B	110	124	97	21	137	115	255	247
	2A	127	124	134	109	159	154	256	250
	2B	129	112	128	112	172	146	247	265
Group 2 (304Gy)	1A	149	103	99	107	139	128	217	258
	1B	150	114	100	113	151	139	233	244
	2A	139	146	116	141	165	142	250	96
	2B	143	123	118	116	167	133	201	100
Group 3 (304Gy)	1A	163	115	15	115	125	145	287	222
	1B	134	136	19	110	118	158	249	237
	2A	127	120	118	73	88	165	235	212
	2B	144	132	119	88	81	175	275	254
Group 4 (304Gy)	1A	136	123	127	141	161	171	277	196
	1B	128	124	124	120	158	133	280	200
	2A	148	136	136	123	71	149	256	208
	2B	157	151	112	133	79	132	254	200

9. Irradiation on 01/24/2005

1/27/05	(20 μ L)	Magnet			Fake magnet		Stand-alone		Hall way	
12+13RB	5 ⁻¹	#1	#2	#3	#4	#5	#6	#7	#8	#9
Group 1 (304Gy)	1A	75	71	87	63	60	68	81	233	206
	1B	86	68	88	62	64	70	61	265	209
	2A	56	50	81	70	29	78	51	163	199
	2B	58	35	78	82	40	100	55	181	216
Group 2 (304Gy)	1A	72	62	56	77	52	63	82	184	191
	1B	50	63	46	69	51	59	90	178	194
	2A	94	62	43	63	51	48	90	209	183
	2B	88	74	40	78	44	33	76	181	169
Group 3 (304Gy)	1A	69	66	58	73	66	69	81	146	160
	1B	71	70	74	75	70	71	83	121	187
	2A	53	58	72	43	57	76	86	174	211
	2B	58	72	66	76	60	61	97	142	218
Group 4 (304Gy)	1A	73	57	94	78	92	66	70	148	126
	1B	68	50	73	88	79	73	66	171	139
	2A	51	62	59	86	52	50	38	121	194
	2B	59	56	60	86	64	46	58	134	186

1/29/05	(20 μ L)	Magnet			Fake magnet		Stand-alone		Hall way	
12+13RB	5 ⁻¹	#1	#2	#3	#4	#5	#6	#7	#8	#9
Group 1 (304Gy)	1A	89	92	99	80	72	83	97	233	208
	1B	98	86	100	79	76	89	78	265	211
	2A	71	54	89	84	37	94	61	164	199
	2B	80	49	100	96	48	110	66	181	216
Group 2 (304Gy)	1A	82	78	70	89	70	83	96	185	192
	1B	63	86	60	81	62	77	102	178	194
	2A	105	73	53	76	71	53	101	209	183
	2B	106	87	48	92	56	36	93	182	169
Group 3 (304Gy)	1A	86	83	77	86	84	77	98	146	161
	1B	80	85	92	92	84	94	90	122	188
	2A	68	73	82	52	66	95	105	175	212
	2B	65	88	79	84	74	67	111	142	218
Group 4 (304Gy)	1A	85	71	112	98	105	76	80	149	126
	1B	84	66	88	105	92	84	81	172	140
	2A	64	76	74	113	68	70	50	121	195
	2B	68	69	75	104	72	54	65	134	186

10. Irradiation on 03/01/3005

3/3/05	(20 μ L)	Magnet			Fake magnet		
14RB	3 ⁻¹	#1	#2	#3	#4	#5	#6
Group 1 (299Gy)	1A	119	67	113	87	45	64
	1B	95	67	105	91	50	70
	2A	93	116	71	101	102	128
	2B	93	107	64	97	90	127
Group 2 (299Gy)	1A	110	96	62	57	122	78
	1B	107	106	74	54	99	95
	2A	124	102	74	89	110	118
	2B	82	118	80	70	96	102
Group 3 (299Gy)	1A	65	86	83	93	104	90
	1B	97	88	97	81	108	78
	2A	96	101	82	116	99	95
	2B	104	102	92	98	96	119
Group 4 (299Gy)	1A	119	105	33	111	89	95
	1B	110	77	34	116	101	92
	2A	113	77	101	105	76	86
	2B	101	93	84	110	81	111

3/8/05	(20 μ L)	Magnet			Fake magnet		
14RB	3 ⁻¹	#1	#2	#3	#4	#5	#6
Group 1 (299Gy)	1A	140	85	128	119	56	83
	1B	109	90	130	112	61	89
	2A	111	142	97	134	134	158
	2B	114	138	82	122	128	168
Group 2 (299Gy)	1A	146	115	92	71	149	101
	1B	134	132	93	73	131	123
	2A	154	128	98	110	143	158
	2B	107	161	109	106	141	138
Group 3 (299Gy)	1A	91	110	103	123	138	117
	1B	114	117	121	113	134	103
	2A	128	135	113	147	123	134
	2B	135	127	128	129	120	149
Group 4 (299Gy)	1A	130	126	41	124	113	113
	1B	125	95	45	133	127	114
	2A	127	94	126	135	96	111
	2B	126	108	95	132	103	141

Appendix D

Experimental setups

1. Irradiation on 09/21/2004

The order of the plates during irradiation was #1, #5, #3, #4, #6 #2 counter-clockwise.

There were 3 groups of irradiation. The doses were fixed to 303Gy. The plates were plated in 6^{-1} concentration of the washing broth (1.5mL). 15 μ L was spread in each dish.

We plated 2 dishes for each membrane. Thus we had 12 dishes for one configuration.

2. Irradiation on 10/04/2004

The order of the plates during irradiation was #3, #5, #1, #2, #6 #4 counter-clockwise.

The doses were fixed to 301Gy for the 3 groups. The plates were plated in 7^{-1} concentration of the washing broth (1.5mL). 20 μ L was spread in each dish.

3. Irradiation on 10/11/2004

The order of the dishes irradiated today was #1, #5, #2, #3, #6, #4, counter-clockwise.

The magnets were changed to bigger ones with 7/8 inch diameter and 1 inch long. The geometry was changed slightly compared with the fake magnets (steel disks). The steel cylinders are made according to the old magnets (3/4 inch diameter and 3/4 inch long).

4. Irradiation on 11/23/2004

The magnets used were 7/8 inch diameter and 1 inch long. The order of the dishes is #4, #6, #3, #2, #5 and #1 CCW. The membranes are 0.5 cm by 0.5 cm. The membranes were put into 1.6 mL of water and 12 μ L of the broth was put in a Petri dish.

5. Irradiation on 11/30/2004

The magnets used were 7/8 inch diameter and 1 inch long. The order of the dishes is #1, #5, #2, #3, #6 and #4 CCW. The membranes are 0.5 cm by 0.5 cm. The membranes were put into 1.6 mL of water and 16 μ L of the broth was put in a Petri dish.

6. Irradiation on 12/07/2004

The magnets used were 2 inch diameter and 1 inch long. We used the new board for the first time. The order of the irradiated dishes is #1, #5, #3, #2, #6, #4, CCW. The dose used was 450 Gy. The membranes are 1 cm by 1 cm.

Each membrane was put into 1.5 mL of water. 0.4 mL of the broth was mixed with 0.4 mL of water to make 2^{-1} broth for x.1-x.6. 0.2 mL of the broth was mixed with 0.8 mL of water to make 5^{-1} broth for x.7 and x.8.

Then 20 μ L of the broth was plated on the YPD agar dish.

7. Irradiation on 12/20/2004

The magnets used were 2 inch diameter and 1 inch long. The order of the samples was #3, #5, #1, #4, #6, #2 counterclockwise. The membranes are 1 cm by 1 cm. The membranes of 3.8 and 3.6 were broken into 2 pieces when they were plated on the non-nutrient agar plates. Some of the 20 μ L of 1-7C was thrown away so that I was expecting the colony number of it would be smaller than others of 1-7, which turned out to be true.

1/6 dilution was applied this time.

8. Irradiation on 01/10/2005

The samples are irradiated this morning start at 8am. The order of samples was #1, #5, #3, #4, #6, #2 CCW. Now we have 16 membrane samples for one configuration. The membranes are 1 cm by 1 cm.

The membranes were put into 1.5 mL of water. 150 μ L of the broth were then put into 750 mL of water in order to get 6^{-1} dilution. Then 20 μ L of it was plated. The top membrane was labeled as 1 and the bottom membrane was labeled as 2.

Membrane 2.82 was broken in two and its inner surface touched the agar with about 1/5-1/4 of its total area.

Membrane 2.11 was thrown into the trash bin by mistake but its surface only touched agars. It was picked up and put in the water but it could be contaminated.

The non-nutrient agar 1.5 was the one that was pressed with a crack.

9. Irradiation on 01/24/2005

The order of the samples is #3,#5,#1,#4,#6,#2 CCW. There are 16 membrane samples for one configuration. The membranes are 1 cm by 1 cm. The membranes were put into 1.5 mL of water. 150 μ L of the broth were then put into 600 mL of water in order to get 5^{-1} dilution. Then 20 μ L of it was plated. The top membrane was labeled as 1 and the bottom membrane was labeled as 2.

10. Irradiation on 03/01/2005

The order of the samples is #4,#1,#5,#2,#6,#3 CCW. #1-#3 are magnets. #4-#6 are fake magnets. The magnets are the 2 inch diameter ones.

I prepared the 14RB to have 178 colonies of 5^{-1} concentration, 20 μL in the Petri dishes, 10 μL of 14RB into 1.5 mL of water.

10 μL of 14RB was put on each membrane. Membranes were put into 1.5 mL of water.

Then 150 μL of the broth was put into 300 μL of water to form 1/3 dilution. Then 20 μL of it was plated.

Appendix E

Order Information

1. *Saccharomyces cerevisiae*

Connecticut Valley Biological Supply Company, <http://www.ctvalleybio.com/>, 1-800-628-7748, Stock# L 9040T, \$8.25/tube

2. *Schizosaccharomyces octosporus*

Connecticut Valley Biological Supply Company, <http://www.ctvalleybio.com/>, 1-800-628-7748, Stock# L 9042T, \$8.25/tube

3. YPD agar medium

BD Biosciences, <http://www.clontech.com/clontech/>, Cat. No. 630410, \$110 per 700g
Fisher Scientific, <https://www1.fishersci.com/Coupon?cid=261105&gid=2420172>,
Cat. No. NC9413245, \$137.50 per 700 g

4. Granulated agar (non-nutrient agar)

Fisher Scientific, <https://www1.fishersci.com/Coupon?cid=1334&gid=2885499>,
FisherBiotech molecular genetics media, agar, used as a solidifying agent, Cat. No.
BP1423-500, \$111.66 for 500 g

5. Nitrocellulose membranes

BioExpress, <http://www.bioexpress.com/cgi-bin/mas/category.cgi?category=12821>,
Protran® Unsupported Nitrocellulose Membranes, Part # F-3125-6, Grade BA83, 0.2
µm, 20 cm × 20 cm, \$106 for 5 sheets

6. Variable gap magnet

PASCO, <http://store.pasco.com/>, EM-8641, \$199 for one

7. NdFeB magnets

Engineered Concepts, http://www.engconcepts.net/List_Of_Disc_Magnets.asp,
D1206, rating N45, 2 inch diameter by 1 inch thick, \$37 each

8. Petri dish

DAIGGER, <http://www.daigger.com/>, Cat. No. EF7159A, 100 mm × 15 mm, \$41.29
for case of 500; Cat. No. EF7159B, \$45.69 for case of 500

Fisher Scientific, <https://www1.fishersci.com/index.jsp>, S67961

9. Microtube

Fisher Scientific

Appendix F

Agar Recipe

1. Non-nutrient Agar

Put 23 g of granulated agar powder into 1000 ml of distilled water. Then put the mixture on a oven and heat it until boiling. Stir the mixture while it is being heated. When the mixture becomes transparent and yellowish, stop heating and wait for the bubbles to disappear. Then pour it into Petri dishes and wait until it turns into agar. Now flip the Petri dishes and let them dry for 2 days before they are used.

2. YPD Agar

Put 14 g of YPD powder into 200 ml of distilled water. Stir the mixture on a vortex machine until the powder mixed with water. Autoclave the mixture at 120° C for 15 min. Then pour the transparent medium into Petri dishes and wait until it turns into agar. Now flip the Petri dishes and let them dry for 2 days before they are used.